Dissertations, Master's Theses and Master's Reports

2016

EFFECTS OF SCATTERING AND ABSORPTION ON LASER SPECKLE CONTRAST IMAGING

Kosar Khaksari
Michigan Technological University, kkhaksar@mtu.edu

Recommended Citation

Khaksari, Kosar, "EFFECTS OF SCATTERING AND ABSORPTION ON LASER SPECKLE CONTRAST IMAGING", Open Access Dissertation, Michigan Technological University, 2016.
http://digitalcommons.mtu.edu/etdr/181

EFFECTS OF SCATTERING AND ABSORPTION ON LASER SPECKLE CONTRAST IMAGING

By
Kosar Khaksari

A DISSERTATION
Submitted in partial fulfillment of the requirements for the degree of
DOCTOR OF PHILOSOPHY
In Biomedical Engineering

MICHIGAN TECHNOLOGICAL UNIVERSITY
2016

This dissertation has been approved in partial fulfillment of the requirements for the Degree of DOCTOR OF PHILOSOPHY in Biomedical Engineering.

Department of Biomedical Engineering

Dissertation Advisor: *Sean J. Kirkpatrick, PhD*

Committee Member: *Keat G. Ong, PhD*

Committee Member: *Michael C. Roggemann, PhD*

Committee Member: *Warren F. Perger, PhD*

Department Chair: *Sean J. Kirkpatrick, PhD*

Table of Contents

List of figures:

Figure 1: a sample speckle pattern

Figure2: Speckle contrast vs. correlation time and camera integration time's ratio (Fercher and Briers results and the correction curve according to Duncan and Kirkpatrick's work)

Figure 3: Contrast for the Lorentsian distribution function

Figure 4: Contrast for the Gaussian distribution function

Figure 5: Comparison of the contrast for the Lorentzian and Gaussian distribution function (the red curve is Lorentzian and the blue one is Gaussian)

Figure 6: hand-made cuvettes

Figure 7: Optical setup for scattering coefficient measurements

Figure 8: LSCI optical setup

Figure 9: Cross section of the sample when there are two populations of moving scatterers in the images area

Figure 10: geometrical and effective cross section of a scattering phenomenon

Figure 11: the scattering three-dimensional plane

Figure 12: Final LSCI setup

Figure 13: Scattering Coefficient $\left(\mu_s\right)$ for different freeze-thaw cycle samples

Figure 14: Reduced Scattering coefficient for different lipid solutions

Figure 15: Raw data and the fitted curve (left figures) and the final curve (right figures) for 3 different freeze-thaw cycles samples.

Figure 16: The speckle pattern (left) and the resultant contrast image (right).

Figure 17: The contrast image for different lipid solutions with different milk concentration (The top left image is for water, the top right image is for 0.1%, the bottom left is for 1% and the bottom right is for 2% lipid solutions)

Figure 18: Contrast vs. reduced scattering coefficient

Figure 19: Sample's cross-section

Paper 1:

Figure 20. Diagram of the LSCI and flow systems.

Figure 21. Sample cross-section.

Figure 22a. A laser speckle pattern.

Figure 22b. Power spectral density of the speckle pattern shown in Fig. (22a). The diameter of the bright central region is inversely proportional to the minimum speckle size in the speckle pattern.

Figure 23. Mie calculations predicting the reduced scattering coefficient for glass spherical particles of 9.0 μm, 10.5 μm, 11.7 μm, and 13.0 μm diameters (dashed lines, red dashed lines on-line). Reduced scattering coefficient as determined by ballistic transmission data points is shown for the fluid phantoms (dots) along with the best-fit line in a least squares sense. The polydisperse microsphere phantoms behaved approximately as a monodisperse system made of of 10.5 μm glass microspheres. $\left(\mu_s^{'} = 48.66[c] - 0.196; \quad r^2 = 0.98 \right)$.

Figure 24. Plot of the absorption coefficient of the fluid phantoms as a function of india ink concentration. $\left(\mu_a = 367.3 \left[\text{ink} \right] + .0016; \quad r^2 = 0.996 \right)$.

Figure 25. A representative LSCI image. The fluid motion was in the low contrast region flowing from upper left to lower right of the image. The surrounding higher contrast triangular areas are the static plastic block.

Figure 26. Plot of K_{ratio} vs. μ_s' at 10 different values of μ_a. All slopes were statistically significant (t-test, p <0.05) and there was no statistically significant difference between the slopes (t-test, p <0.05). The mean slope was $-5.53e-2\dfrac{\Delta K_{ratio}}{\Delta \mu_s'}$.

Figure 27. Plot of the y-intercepts $\left(\mu_s' = 0 \right)$ of Fig. (7) as a function of respective absorption coefficients. An increase in absorption resulted in a linear decrease in K_{ratio} in these experiments due to reducing the influence of the underlying static scatterers. $\left(K_{ratio|\mu_s'=0} = -5.68\mu_a + 0.94 ; \quad r^2 = -0.982 \right)$.

Figure 28. Plot of K_{ratio} vs. μ_a at 10 different values of μ_s'. All slopes were statistically significant (t-test, p <0.05) and there was no statistically significant difference between the slopes (t-test, p <0.05). The mean slope $-4.01\dfrac{\Delta K_{ratio}}{\Delta \mu_a}$.

Figure 29. Plot of the y-intercepts $\left(\mu_a = 0 \right)$ of Fig. (7) as a function of respective reduced scattering coefficients. An increase in scattering resulted in a linear decrease in K_{ratio}. $\left(K_{ratio|\mu_a=0} = (-7.02e-2)\mu_s' + 0.92 ; \quad r^2 = -0.976 \right)$.

Figure 30. Plot of K_{ratio} vs. μ_t for the phantom samples that were along the major axis of the scattering and absorption phantom matrix. An increase in μ_t resulted in a significant decrease in K_{ratio}. $\left(K_{ratio} = -0.14\mu_t + 0.93; \; r^2 = -0.94 \right)$.

Paper 2:

Figure 31. Diagram of the LSCI and flow systems.

Figure 32. Sample cross-section.

Figure 33a. K_{ratio} vs. reduced scattering coefficient. A strong negative correlation (r^2=0.95) was found between the two variables. The slope of the best fit line was -0.072.

Figure 33b. K_{ratio} vs. scatterer concentration. A strong negative correlation (r^2=0.97) was found between the two variables. The slope of the best fit line was -3.3e-3.

Figure 34. Relationship between speckle contrast and the velocity of the moving fluid. The fluid phantom had a reduced scattering coefficient of 2.2 mms^{-1}. The correlation coefficient, $r^2 = 0.96$.

Figure 35. Relationship between K_{ratio} and advective flux. A strong negative linear relationship was found ($r^2 = 0.97$).

Paper 3:

Figure. 36 Example of a band-limited numerically generated speckle pattern (a), its pseudo-phase representation (b) and the pseudo-phase representation with the positively charged (green stars) and negatively charged (red circles) optical vortices identified (c).

Figure. 37 Autocorrelation functions of the rapidly decorrelating speckle sequence versus the more slowly decorrelating speckle sequence used in this study.

Figure. 38   Three-dimensional representation of the vortex trails for the rapidly decorrelating speckle sequence (a) and the more slowly decorrelating speckle sequence(b). The green stars represent the positively charged vortices and the red circles represent the negatively charged vortices.

Paper 4:

Figure. 39. Optical layout of the LSCI simulating system. The laser was a 2.5mW stabilized HeNe (633nm) and the image magnification equaled ~ 0.61.

Figure 40. (a) Phase screen loaded to the SLM. (b) The resulting imaged speckle pattern. (c) Simulated LSC image. The center rows in (2c) represent the 'flow' region. The contrast ratio between the static and dynamic regions was 4.108.

Figure 41. Intensity PDF's of SLM generated speckle patterns plotted along with numerically simulated (theoretically ideal) speckle patterns. (a) Fully developed, polarized intensity PDF showing both experimental (SLM) and theoretical speckle patterns in agreement. (b) Non-polarized intensity PDF showing both experimental and theoretical results in agreement.

Figure 42. (a) SLM generated speckle pattern (b) SLM generated speckle PSD.   The minimum speckle size in this case was 4 pixels. (c) Variation in speckle size is plotted as a function of the aperture diameter, with a fitting function overlaid for future calibration.

Figure 43a-c. Decorrelation curves for SLM speckle patterns with different correlation behaviors (top 3 figures). From the left, the decorrelation times were 70, 37 and 17 frames, respectively. **Figure 43d**. Demonstration of both Lorentzian and Gaussian decorrelation behaviors (bottom).

Figure 44. SLM simulated contrast vs $\frac{\tau_c}{T}$ for both a Gaussian and Lorentzian velocity distribution. The SLM set-up was able to faithfully reproduce the expected results for both flow models.

Paper 5:

Figure 45. Relationship between contrast (K_{Ratio}) and μ_s . Each best fit line represents a single μ_a , with the largest μ_a values at the bottom. There are no significant differences between slopes. $K_{Ratio} \propto -0.0374 \mu_s$.

Figure 46. . Relationship between contrast (K_{Ratio}) and μ_a . Each best fit line represents a single μ_s , with the largest μ_s values at the bottom. There are no significant differences between slopes. $K_{Ratio} \propto 1.28e-3\mu_a$.

Figure 47. Effects of μ_t on K_{Ratio} . A significant negative relationship between the variables was found. $K_{Ratio} \propto -0.0543\mu_t$.

Paper 6:

Figure. 48. (a) Optical layout of the LSCI simulating system. The laser was a 2.5mW stabilized HeNe (633nm). The focal length of L_1, L_2, and L_3 are 75mm, 125mm, and 75mm, respectively. The image magnification equaled ~ 0.5. (b) Horizontal view of the imaging arm of the set-up. The distance from L_2 to L_3 was ~300mm. The CMOS array was located ~132mm from the back focal plane (BFL) of L_3. The principal plane, v, was estimated to be ~37.5mm from the CMOS array.

Figure. 49. Decorrelation curve for SLM speckle patterns with different correlation behavior exhibiting a Gaussian decorrelation profile. For this example, 50 screens were

11

created to image 50 consecutive speckle patterns. (a) Decorrelation time of 37 frames, (b) Decorrelation time of 17 frames, (c) Demonstration of both Lorentzian and Gaussian decorrelation behaviors showing a Lorentzian autocorrelation function (stars) plotted along with a Gaussian autocorrelation function (dots).

Figure. 50. (a) Phase screen loaded to the SLM. The pixel-phases were evenly distributed and randomly generated between $[0,2\pi]$. The pixel values are displayed as a psudo- color image with 64 discrete values. (b) The resulting speckle pattern imaged with an 8-bit CMOS camera. The random interference can be seen mapped to gray values between $[0,255]$, with a value of 255 indicating purely constructive interference, and 0 resulting from destructive interference.

Figure. 51. Intensity PDF's of SLM generated speckle patterns plotted with numerically simulated (theoretically ideal) speckle patterns. (a) Fully developed, polarized intensity PDF showing both experimental (SLM) and theoretical speckle patterns in agreement. (b) Non-polarized intensity PDF showing both experimental and theoretical results in agreement. It is worth noting that the Rayleigh PDF is often dependent on the scale factor used. For this experiment, the logarithmic scale shows similar linearity to assume an accurate intensity distribution.

Figure. 52. (a) SLM generated speckle pattern (b) SLM generated speckle PSD. The minimum speckle size in this case was 4 pixels. (c) Variation in speckle size plotted as a function of the aperture diameter, with the theoretical curve of Eq. 1 plotted as the solid line. The experimentally sampled speckle size is plotted as blue dots.

Figure. 53. Simulated LSC image. The center region represents the 'flow' region $\left(\tau_{c2}\right)$. The contrast ratio between the static $\left(\tau_{c1}\right)$ and dynamic region was 4.108dB. In this figure,

the contrast range was set between [0,1.5]. The nearly concentric rings arose from reflections in the optical system.

Figure. 54. SLM simulated contrast vs $\dfrac{\tau_c}{T}$ for both a Gaussian and Lorentzian velocity distribution. The SLM set-up was able to faithfully reproduce the expected results for both flow models.

Figure. 55. Relation between ND filter and average intensity at CMOS array. The intensity was reduced logarithmically from the full intensity of .0605mW/cm^2.

Figure. 56. "Frozen" speckle patterns at (a) 100%, (b) 30%, (c) 8.75%, and (d) 3.4%, of full intensity (.0605mW/cm^2).

Figure. 57. (a) Contrast in a single speckle frame. In the case where a large number of speckles are used to calculate *K* the theoretical limit of *K=1* can be assumed as the "ideal."[11] (b) The global mean intensity (black dots) and standard deviation (red stars) used to calculate contrast of a single speckle pattern.

Figure. 58. PDF of speckle patterns at (a) 100%, (b) 30%, (c) 8.75%, (d) 1.1%, (e) .35%, and (f) .12% of full intensity, plotted on a log scale. Camera histogram of speckle patterns at (g) 100%, (h) 30%, (i) 8.75%, (j) 1.1%, (k) .35%, and (l) .12% of full intensity.

Figure. 59. Spatial analysis of speckle patterns at intensities of (a) 100%, (b) 30%, (c) 8.75%, (d) 3.4%, (e) 1.1%, and (f) .35%. The ring in the upper right corner of the images comes from statistically negligible noise in the optical system.

Figure. 60. (a) Contrast of speckle regions in spatial averaged LSCI. Red stars indicate the 'flow' region of faster decorrelating speckle, with the black dots indicative of the 'tissue'

region with slower decorrelating speckle. (b) Contrast ratio of the 'flow' region and the 'static' region. Optimum sensitivity to temporal changes follow the trends in Fig. 10.

Figure. 61. (a) PSD of frozen speckle pattern imaged at 8.75 % of full intensity (b) Intensity profile through the center of (a). (c) Frequency information was used to calculate 'apparent' speckle size at each incident intensity. The 'apparent' increase in speckle size was actually a loss of high frequency content in the image due to saturation.

Figure. 62. Raw speckle data imaged at 0.35% intensity: (a) histogram scaled (b) Contrast values shown with all images scaled to fill the full dynamic range of the 8-bit camera. The optimum imaging window of incident intensity showed little to no difference in the spatial analysis between the original (red stars) and scaled (blue triangles) images (c) Contrast ratio of the 'flow' region and the 'static' region for both scaled (blue triangle) and unscaled (red star) speckle.

Paper 7:

Figure 63a. B-scan of the unrestricted flow phantom. The tube containing the flow is the slightly darker region approximately 2/3 of the way down from the top. No information about motion is revealed.

Figure 63b. Probability distribution function of the B-scan shown in Fig. (63a). The distribution is Rician, starting to converge on a Gaussian distribution indicating a significant specular component to the echo.

Figure 63c. Power spectral density of the B-scan shown in Fig. (63a) used to compute the minimum speckle size in both the axial and the range direction. The non-circular shape of the bright central energy band indicates that the speckles have different dimensions in the two directions.

Figure 64. (a) B-scan of the unrestricted flow phantom. (b) Temporal contrast image using 10 frames to calculate the contrast statistic. (c) Temporal contrast image using 100 frames to calculate the contrast statistic. (d) Temporal contrast image using 200 frames to calculate the contrast statistic.

Figure 65. (a) B-scan of the diffusive flow phantom with a slower flow rate. (b) Temporal contrast image using 10 frames to calculate the contrast statistic. (c) Temporal contrast image using 100 frames to calculate the contrast statistic. (d) Temporal contrast image using 200 frames to calculate the contrast statistic. Of particular note is the progression of the area of the image that displays increasing from left to right contrast as time (number of frames) increases. This indicates a diffusion front moving through the sponge.

Figure 66. (a) B-scan of the diffusive flow phantom with a faster flow rate. (b) Temporal contrast image using 10 frames to calculate the contrast statistic. (c) Temporal contrast image using 100 frames to calculate the contrast statistic. (d) Temporal contrast image using 200 frames to calculate the contrast statistic. . Of particular note is the progression of the area of the image that displays increasing from left to right contrast as time (number of frames) increases. This indicates a diffusion front moving through the sponge.

Figure 67. Plot of the ratio of the temporal contrast in the flow region to that in the static gel region, K_{ratio}. From top to bottom, K_{ratio} for the slow diffusive phantom (green stars on-line), K_{ratio} for the unrestricted flow phantom (red dashes on-line), and K_{ratio} for the fast diffusive phantom (blue dots on-line).

List of tables:

Preface

Chapter 4 Contribution of Authors:

Sean J. Kirkpatrick: Principal Investigator, data evaluation, writing and edition
Kosar Khaksari: Ran the experiments; Developed theory, Wrote computer code, Analyzed data, Wrote manuscript

Kosar Khaksari and Sean J. Kirkpatrick*
*Corresponding Author: E-mail: sjkirkpa@mtu.edu

Chapter 5 Contribution of Authors:

Sean J. Kirkpatrick: Principal Investigator, data evaluation, writing and edition
Kosar Khaksari: Ran the experiments; Developed theory, Wrote computer code, Analyzed data, Wrote manuscript

Kosar Khaksari and Sean J. Kirkpatrick*
*Corresponding Author: E-mail: sjkirkpa@mtu.edu

Chapter 6 Contribution of Authors:

Sean J. Kirkpatrick: Principal Investigator, data evaluation, writing and edition
Kosar Khaksari: Ran the experiments; Developed theory, Wrote computer code, Analyzed data, Wrote manuscript
Donald D. Duncan: helped to develop some of the mathematics and computer codes

Sean J. Kirkpatrick[1], Kosar Khaksari, Dennis Thomas
Department of Biomedical Engineering
Michigan Technological University
1400 Townsend Dr.
Houghton, MI 49931
906-487-2167 (phone)
sjkirkpa@mtu.edu

Donald D. Duncan
Department of Electrical and Computer Engineering
Portland State University
Fourth Avenue Building
1900 SW 4th Avenue, Suite 160
Portland OR, 97201

[1]Corresponding Author

Chapter 7 Contribution of Authors:

Mitchell A. Kirby: Ran experiments, Developed optical layout
Sean J. Kirkpatrick: Principal Investigator, data evaluation, writing and edition
Kosar Khaksari: Ran the experiments; Developed theory, Wrote computer code, Analyzed data, Wrote manuscript

Mitchell A. Kirby, Kosar Khaksari, Sean J. Kirkpatrick*

*Corresponding Author: E-mail: sjkirkpa@mtu.edu

Chapter 8 Contribution of Authors:

Sean J. Kirkpatrick: Principal Investigator, data evaluation, writing and edition
Kosar Khaksari: Ran the experiments; Developed theory, Wrote computer code, Analyzed data, Wrote manuscript

Kosar Khaksari and Sean J. Kirkpatrick*

Chapter 9 Contribution of Authors:

Mitchell A. Kirby: Ran some experiments, Developed optical layout
Sean J. Kirkpatrick: Principal Investigator, data evaluation, writing and edition
Kosar Khaksari: Ran the experiments; Developed theory, Wrote computer code, Analyzed data, Wrote manuscript

Mitchell A. Kirby, Kosar Khaksari, Sean J. Kirkpatrick*

*Corresponding Author: E-mail: sjkirkpa@mtu.edu

Chapter 10 Contribution of Authors:

Sean J. Kirkpatrick: Principal Investigator, data evaluation, writing and edition
Kosar Khaksari: Developed theory, Wrote computer code, Analyzed data, Wrote manuscript
David Rosen: Ran ultrasound experiments
Jingfang Jiang: Oversaw ultrasound experiments

Kosar Khaksari, David Rosen, Jing fang Jiang and Sean J. Kirkpatrick*
*Corresponding Author: E-mail: sjkirkpa@mtu.edu

Abstract

Laser Speckle Contrast Imaging (LSCI) is a real-time, non-invasive method in used to investigate blood flow and perfusion in biological tissues with high temporal and spatial resolution. A reduction in speckle contrast due to particle motion is the primary contrast mechanism in LSCI. Motion results in speckle fluctuations in time and reduces the contrast over a given camera integration period. There are a variety of parameters that effect contrast besides motion. The optical properties of the scattering medium are one of the parameters effecting LSCI values. Changes in blood hematocrit levels manifest as changes in optical properties. In this work, we explore the effects of different hematocrit levels on LSCI contrast values using fluid phantoms with varying optical properties.

Herein, the combined effects of scattering and absorption coefficients on LSCI values are investigated using fluid phantoms. These fluid phantoms were designed to mimic the scattering and absorbing properties of blood with varying levels of hematocrit. The flow phantoms in our experiments contained different concentrations of glass microspheres (brand name Luxsil) and India ink mixed with DI water. The different number of scatterers and absorbers in the phantoms mimic the scattering and absorption behaviors of blood with different number of red blood cells. An LSCI setup combined with a simple flow system was used in our experiments in order to investigate the effects of combined scattering and absorption coefficient of 121 samples with different concentrations of Luxsil and India ink microspheres. The fluid phantoms were run in 2mm glass tubing on top of a plastic block using a mini peristaltic pump. An LSCI setup imaged the flow using a CCD camera. A MATLAB GUI controlled the pump and camera to provide near real-time contrast images of the flow. An 11x11 matrix of phantoms was created. Scattering coefficient was varied

on the columns and absorption coefficient was varied on the rows such that the first element of the matrix is water and the last element contains the phantom with the maximum number of scatterers and absorbers. A hundred raw speckle images were recorded for each phantom experiment using the described optical setup. The experiments were conducted 3 times for each element of the matrix. The 11x11 results matrix displayed the average speckle image of all 300 raw speckle images. Additionally, the matrix was filled by the contrast images where contrast was defined as standard deviation of intensity over mean intensity. In order to compare the results numerically, we calculated the ratio of the contrast from the same size window of moving portion over the static portion of the phantoms. According to the results from LSCI experiments, an increase in scattering and absorption coefficients led to a reduction in contrast values of LSCI images. By increasing the number of scatterers and absorbers (equivalent to changing hematocrit level), the optical properties (scattering and absorption coefficient) increased, which led to a reduction in contrast value in the moving area. A negative slope linear curve describes the relationship between K_{ratio} and scattering coefficient (μ_s) and between K_{ratio} and absorption coefficient (μ_a).

Chapter 1

Literature review

1.1 An introduction to Laser Speckle Contrast Imaging (LSCI)

Laser Speckle Contrast Imaging (LSCI) is a non-invasive method for monitoring blood flow and perfusion. None-invasive techniques for monitoring blood flow have been in existence for approximately 30 years [1]. Laser speckle phenomenon is the basis of many of these methods. In the 1960s the laser speckle phenomenon was observed and researchers began exploiting it for a variety of metrology applications. In the 1970s, researchers began investigating time-varying speckle that resulted from coherent light being scattered from dynamic systems. Ferchers' group at University of Essen in Germany first proposed LSCI in 1980 [2]. The main goal of their research was to develop a non-invasive method to monitor blood perfusion in retina. Early methods involved injecting a fluorescent dye to patient's blood vessels until it was visible in the retina. [2,3]. It is obvious that this method was invasive and a non-invasive method was preferred. LSCI is a method that exploits the relationship between speckle fluctuations and moving particles in the living tissues, noninvasively. Motion in the object space causes speckle fluctuations in time in the image space. When speckles fluctuate on a time scale shorter than the observing camera integration time, the result is a blurring of the speckle pattern in the image. This blurring results in a reduction in spatial contrast.

The early manifestation of LSCI to monitor blood flow in the retina employed single exposure speckle photography with a film camera [2]. A particular challenge in using the single exposure method with film was the post processing steps necessary after taking the speckle images in order to extract the information we need. With the advent of CCD cameras in the 1990's, near real-time methods were developed to monitor blood flow with minimal further processing.

1.2 Laser Speckle

When we illuminate a diffuse surface or a scattering volume with laser light, the scattered light produces a random interference pattern called laser speckle. In the past, speckles were considered primarily as a nuisance, or source of noise, which lowered the quality of images. . More recently, however, it has been recognized by the biomedical optics community that dynamic speckle patterns carry with them information about dynamic biological tissues. Figure 1 shows a sample speckle pattern:
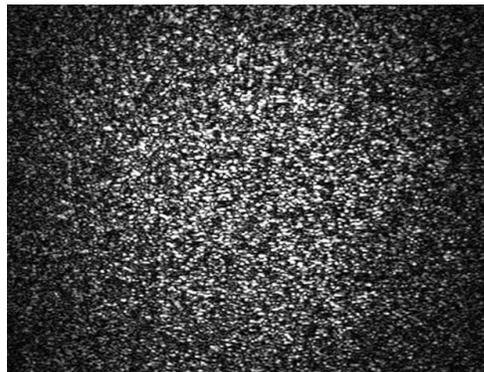
Figure 1: a sample speckle pattern

When a rough surface is illuminated by laser light, where the surface variation is on the order of or longer than the wavelength of the light, the back-scattered beams follow different optical path lengths to reach the image plane. The coherent addition of the beams reaching a single point on the image plane yields the final intensity at that point. If the summation of all the amplitudes cancels each other out, the resultant intensity is zero. In the other hand, when all of wavelets are in phase, the maximum intensity will be achieved. Since laser speckle is a random process, it is appropriate to describe it statistically. Thus, when we want to talk about speckles and mathematic behind them, the probability distribution function is one the most important thing to mention.

The contrast of a speckle pattern is defined as the ratio between standard deviation and mean intensity:

Equation 1.1

$$K(\overline{r}) = \frac{\sigma_I(\overline{r})}{\mu_I(\overline{r})}$$

Which σ_I is standard deviation of the intensity and μ_I is mean of the intensity. When we illuminate a perfectly diffusing surface with a polarized, single frequency, highly coherent laser light, the standard deviation is equal to the mean intensity in the resultant speckle pattern. The contrast is equal to unity in this case, which indicates that there is no motion in the object plane during the time period of the camera integration. Typically, in biological tissues, there is always some motion in the scattering particles and standard deviation is smaller than mean intensity, reducing the contrast. Thus, by this definition, contrast is bound between zero and one. It should be noted, however, that the local contrast in a

speckle image has its own probability distribution (Duncan, Kirkpatrick, Wang "Statistics of local speckle contrast", JBO…).

1.2.1 Time-varying speckles

When there is motion in the scattering particles, the back-scattered beams coming from the moving particles will result in a variation or fluctuation in the speckle intensity with time. This fluctuation blurs the normally sharp speckles and reduces the contrast of the speckle image. This actually is the main concept in LSCI. The speckles whose intensity fluctuates in time are called 'time varying speckles'. When monitoring a living organ, this reduction in contrast due to motion can be used to investigate the flow or motion. This method is called *laser speckle imaging*, which is the main subject of this work.

In this method, the temporal statistics of speckle fluctuations gives us information about the motion. It is common to use temporal statistics; but in some cases the spatial contrast of the time integrated speckle patterns is worth using instead.

1.3 Comparison with Laser Doppler

Another method for analyzing intensity fluctuations is Lase Doppler Flowmetry. Both LSCI and LDF analyze the fluctuations coming from the moving particles. In the Doppler method, when the particles are moving, the detected intensity is frequency shifted and this frequency-shift will be recorded. The frequency of resultant signal is the frequency difference between each point and a reference beam. The reference beam can actually be a non-shifted light, which comes from the stationary part of the object. But in the case of

time-varying speckles, there is no frequency shift. The frequency is the same for the moving particles and the speckles. But the optical path lengths are different. The intensity difference in the speckles pattern for LSCI is because the scattered beam passes different optical path length to reach the detector. When there is motion in the imaging area, the moving particles cause the beam passes different optical path length and this difference causes fluctuations in intensity in speckle pattern.

In the end, the mathematics behind these two methods is similar and both aim to find the relationship between velocity in the object space and the frequency of the fluctuations in the observation space. In some ways, the two approaches are actually two different ways of looking at the same phenomenon.

In Doppler method, in order to work with the temporal statistics of speckles, we have to do the measurements on a point-by-point basis. Thus, to have a map of fluctuations, we need to do the measurements for all the points. A method of scanning is required in this process. There are some devices on the market for that emply scanning Doppler velocimetry to provide a map of velocity. Howver, the scanning process takes time, usually several minutes and makes the imaging method slow. LSCI solvesthis problem by being a full-field imaging technique. It provides a map of relative velocity in a single shot, which makes this method a near-real time imaging method.

1.4 Literature review on LSCI and math behind it

LSCI was used for diagnosing various problems of the eye initially [18]. Existing methods at the time were invasive [19] and a non-invasive method to monitor the blood vessels in the retina [20, 21, 22] was desired. Double exposure speckle photography was the first

method proposed [23]. An effect was observed many years earlier that the contrast of speckles is reduced if speckles fluctuate, and this could be utilized to find velocity. At that time, single exposure speckle photography was proposed by Fercher and Briers [23, 24]. In laser speckle photography the basic idea is that if there is flow in the imaging area the speckle pattern in the image will be blurred. This blurring depends on the relative velocity and exposure time [23]. Furthermore, the speckle pattern has high contrast in the area where there is no flow. Mathematically, the contrast can be written as a function of the ratio of characteristic correlation time and camera integration time [25]. There are some assumptions in this regard. Assuming the exponential distribution for the velocity will give us the following equation for contrast:

Equation 1.2

$$K = \frac{\sigma}{\langle I \rangle} = \left\{ \frac{\tau_c}{2T} \left[1 - \exp\left(-\frac{2T}{\tau_c} \right) \right] \right\}^{\frac{1}{2}}$$

Assuming a Lorentzian velocity distribution of blood flow in vessels, Fercher and Briers plotted the intensity versus the ratio of correlation time and exposure time (Figure.1):
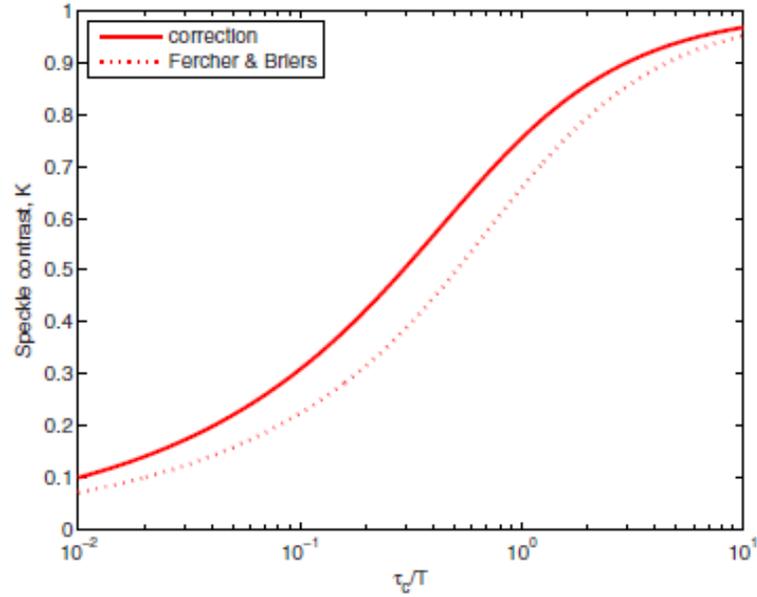
Figure 2: Speckle contrast vs. correlation time and camera integration time's ratio

(Fercher and Briers results and the correction curve according to Duncan and Kirkpatrick's work).

In the case of single exposure, the camera integration time is constant. It can be seen from this curve that the contrast is near zero when the correlation time is low and it trends towards unity when the correlation time is high. For a different assumed velocity distribution (*e.g.* a Gaussian) the general shape of the curve is the same, however, there is a small horizontal shift in the values [25].

As can be seen from this curve, the contrast is near zero when there is significant relative motion, and in the case of no motion the contrast reaches a maximum. In practice, it is not easy, or even possible in some situations, for the human eye to identify the contrast variations. Thus, for making these variations visible to the eye, a high pass filter was necessary.. This filter converted contrast variations to intensity variations. Using this filter, a large amount of light is diffracted when the speckle contrast is high and the light passes

throughout the lens when the contrast is low. In comparison to the raw images, blood vessels are more obvious in the processed version of the images after using this filter.

The single exposure speckle photography was abandoned in the 1980s partially because of this long process. At that time, a method without the photographic stage was being investigated [26, 27]. Thus, laser speckle contrast imaging was born. A simple optical setup was considered in this method. The object was illuminated by laser light and a CCD camera imaged the illuminated area. There are several parameters in the system that was under operator control. In the initial LSCI, camera integration time, size of speckles and the number of pixels were the parameters, which could be fixed by the operator [28]. If there was movement in the area under investigation, the intensity of those speckles fluctuated in time. A time-integrated image during a short exposure time was obtained using this method. The short exposure time makes the LSCI a near-real time technique. Speckle size in comparison to the pixel size is an important factor to be determined. The best cooperation in this case is when the speckle size is at least 2 times of the pixel size [23].

Although LSCI is a simple, fast and cheap method, it has some challenges [29]. For example, it is not obvious if LSCI is sensitive to flow or velocity. And also, the results are not robust and without some means of calibration, absolute values for flow or velocity are impossible to quantify. In or der to make LSCI a more quantitative too, especially in comparison to the laser Doppler flowmetry (LDF), these isues, along with otheres need to be resolved [30]. LDF uses temporal statistics instead of spatial statistics and the power spectrum is analyzed in this method [23,20].

The underlying concept of LSCI is the association of the camera integration time and the speckle contrast [25]. In order to calculate the local contrast, the intensity is calculated by an integration of the instantaneous intensity over a rectangular window.

Equation 1.3

$$I(t) = \frac{1}{T} \int i(t) rect(\frac{t-t'}{T}) dt$$

$$rect(x) = \begin{cases} 1 & |x| = \frac{1}{2} \\ 0 & else \end{cases}$$

In these equations T is camera integration time. Recall that contrast is defined as Equation 1.1. To create a contrast image, the contrast should be calculated for each pixel using Equation 1.1. Thus, the standard deviation and the mean intensity are the parameters to be calculated. According to the statistical equations, the mean intensity is equal to the expectation of the intensity $E(i)$, and we have the equation below for $E(i)$:

Equation 1.4

$$E(i) = \frac{1}{T} \int E\{i(t)\} rect\left(\frac{t-t'}{T}\right) dt$$

And in order to calculate standard deviation, we need variance:

Equation 1.5

$$i^2 = \frac{1}{T} \int_0^T C_i(\tau) \left[2\left(\frac{1-\tau}{T}\right) \right] d\tau$$

where C_i denote the covariance of the instantaneous intensity and E is the expectation.

The complex Gaussian moment theorem can be considered under the assumption that the instantaneous intensity is due to scatter from a very large number of particles. The complex Gaussian moment theorem expresses the fourth order statistical moment in terms of products of second order moments:

Equation 1.6

$$C_i(\tau) + \mu_i^2 = R_i(\tau) = \mu_i^2 + \left| R_{E(\tau)} \right|^2$$

This relationship is known as Siegert relation. Another assumption that should be considered here is to assume Brownian motion for the scattering particles velocity. According to this assumption:

Equation 1.7

$$R_E(\tau) = \mu_i \exp\left[-|\tau| \middle/ \tau_c \right]$$

where τ_c is the characteristic correlation time, which depends on the mass of particle and frictional forces. Thus, the covariance is:

Equation 1.8

$$C_i(\tau) = \mu_i^2 \exp\left[2|\tau| \middle/ \tau_c \right]$$

And finally for the contrast we have:

Equation 1.9

$$K = \frac{\sigma}{\langle I \rangle} = \left\{ \frac{\tau_c}{2T} \left[2 - \frac{\tau_c}{2T} \left(1 - \exp\left(-\frac{2T}{\tau_c} \right) \right) \right] \right\}^{1/2}$$

This approach has a fundamental issue, which the assumption of having the exponential correlation function related to Brownian motion for the ordered flow. Fercher and Briers pointed out that the contrast is in a Lorentzian shape under the assumption of an exponential correlation function.
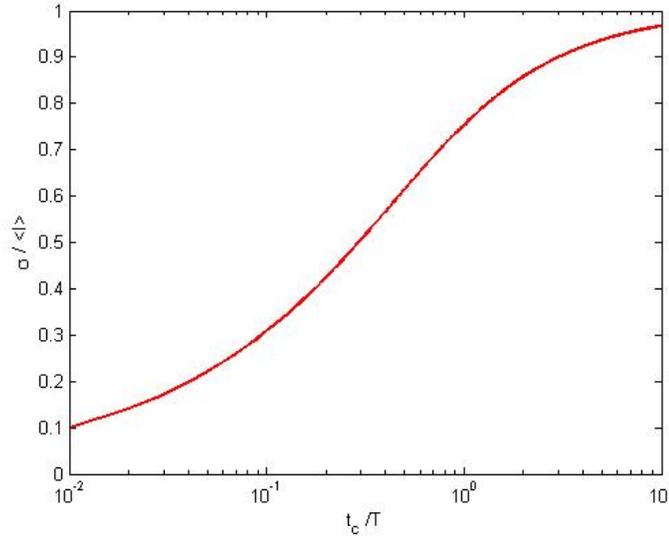
Figure 3: Contrast for the Lorentzian distribution function.

If we considered the ordered flow as an inhomogeneous broadening phenomenon, the line shape for the ensemble of scatterers is Gaussian and in this case, the correlation function is Gaussian too.

Assuming the Gaussian model for the covariance of instantaneous intensity leads to:

Equation 1.10

$$C_i(\tau) = \mu_i^2 \exp\left[2\left(\frac{|\tau|}{\tau_c}\right)^2\right]$$

The measured contrast is shown by:

Equation 1.11

$$K = \frac{\sigma}{\langle I \rangle} = \left\{ \frac{\tau_c}{2T} \left[\sqrt{2\pi} erf\left(\frac{\sqrt{2}T}{\tau_c} \right) - \frac{\tau_c}{T} \left(1 - \exp\left(-2\left(\frac{T}{\tau_c} \right)^2 \right) \right) \right] \right\}^{\frac{1}{2}}$$

And the contrast curve under the assumption of a Gaussian correlation function is shown in the figure below:
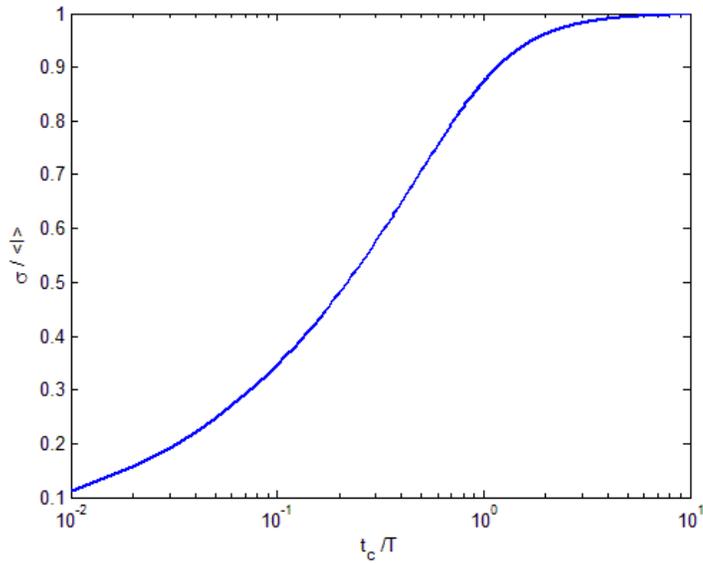
Figure 4: Contrast for the Gaussian distribution function.

The significant differences between the Lorentzian and Gaussian correlation function is shown in the image below. As we can see from the two curves, these too line shapes are slightly different but they have identical same dynamic ranges and overall similar shapes. The real correlation function for the ordered flow is likely a mixture of these too correlation functions and the true model may be the convolution of these two line shapes.
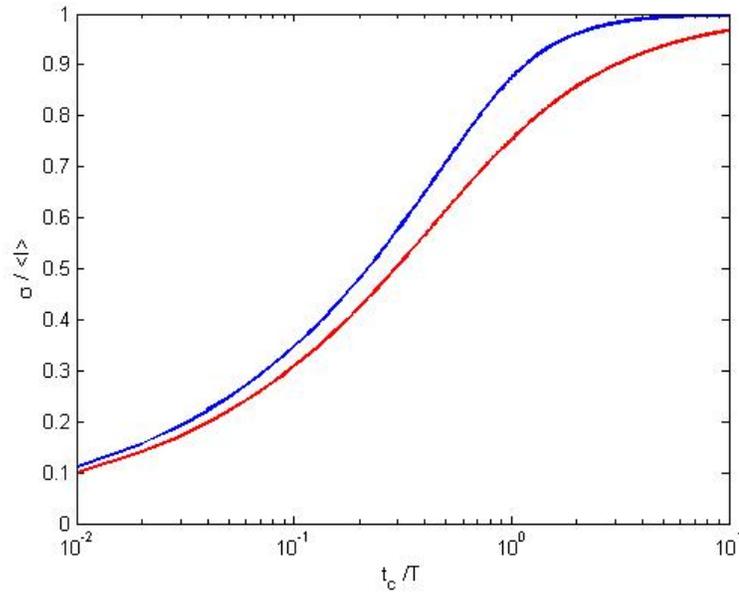
32

Figure 5: Comparison of the contrast for the Lorentzian and Gaussian distribution

function (the red curve is Lorentzian and the blue one is Gaussian).

The final goal in LSCI is to measure velocity. But there are some common errors in this method that prevent it from being a quantitative tool [25]. The first one is a persistent mathematical error, which is missing a triangular window in the variance equation. The actual variance according to what we discussed earlier should be defined as:

Equation 1.12

$$\sigma_i^2 = \frac{1}{T} \int_0^T C_i(\tau) \left[2\left(1 - \frac{\tau}{T}\right) \right]$$

But the triangular window in the Fercher and Briers work was missing and the resultant contrast was:

Equation 1.13

$$K = \frac{\sigma}{\langle I \rangle} = \left\{ \frac{\tau_c}{2T} \left[1 - \exp\left(-\frac{2T}{\tau_c} \right) \right] \right\}^{1/2}$$

Which is different from what we had earlier:

Equation 1.14

$$K = \frac{\sigma}{\langle I \rangle} = \left\{ \frac{\tau_c}{2T} \left[2 - \frac{\tau_c}{2T} \left(1 - \exp\left(-\frac{2T}{\tau_c} \right) \right) \right] \right\}^{1/2}$$

Another problem is that there is not a proper statistical model for the unordered flow [31]. Some workers consider it to be similar to the ordered flow and assume Lorentzian function for the unordered flow, too. In some works, this statistical behavior considered as Gaussian distribution. But in reality, the actual statistical behavior of the flow lies somewhere between Gaussian and Lorentzian.

The third problem on the way of LSCI to becoming a truly quantitative tool is the relationship between correlation time and flow velocity. LSCI is based on the relationship between contrast and speckle movements. The concept is to infer a correlation time from the contrast image. This correlation time and velocity are inversely proportional; but there is no substantial equation to show this relationship. A suggested relationship is:

Equation 1.15

$$\tau_c = \frac{\lambda/2\pi}{V}$$

where λ is the wavelength of the laser light used in the experiment. It means the correlation time is the quotient of wavelength as a physical length scale and the velocity. Since the desired output of LSCI is the velocity values, the mathematical errors should be solved, a

proper distribution function should be considered for the flow and the relationship between the time constant and velocity should be defined.

1.5 Effects of optical properties on LSCI

If there is no flow in the imaged area in laser speckle contrast imaging, there will be maximum contrast in the speckle pattern, because effect of static scatterers is maximum. But if there is flow (or other motion) in imaging area, the intensity of each moving speckle fluctuates from its original intensity. Thus, the number of moving particles will have an effect on LSCI. Changing the number of scattering particles alters the optical properties of the imaged sample. This aim will consider the effects of optical properties on the observed contrast in laser speckle contrast imaging. The effects of optical properties such as the scattering coefficient, absorption coefficient and anisotropy of scattering will be investigated through numerical simulations and experimentation.

1.5.1 Literature review on optical properties

Propagation of light in biological tissues is an important consideration in medical optical imaging [3]. When light interacts with biological tissue, it can be scattered, absorbed or both [4, 5].

Light propagation in biological tissues can be describes by Boltzmann equation that consist of three optical properties, scattering coefficient, absorption coefficient and anisotropy of scattering [6]. Various experimental methods for measuring these optical properties have been proposed [7, 8, 9, 10]. In this work, we use a modified Lambert-Beer law to estimate the scattering coefficient through the experiments [11]. This law technically only applies

to absorption; but in this work we use a modification of Lambert-Beers law to discuss about both absorption and scattering.

The scattering coefficient reveals the inverse of the mean distance a photon travels in a scattering medium before being scattered and can be approximated with the Lambert-Beer's law. In an absorbing medium, the Lambert-Beer's law relates the radiant power to the path length of the beam and to the concentration of the absorbers (chromophores), respectively. This law can be shown by this equation:

Equation 1.16

$$T = \frac{I}{I_0} = 10^{-\mu_a l}$$

where μ_a is the absorption coefficient and l is the geometrical distance light travels through the media. If we use the modified Lambert-Beer's law for absorption and scattering, the equation above can be shown as:

Equation 1.17

$$I(z) = I_0 \left[\exp\left(-(\mu_a + \mu_s)z\right) \right]$$

Where μ_a is the absorption coefficient, μ_s is the scattering coefficient, z is the sample thickness, I_0 is the intensity without any sample in the experiment and I_0 is the intensity when a sample with z thickness is using for the experiment.

At the wavelengths of interest in this work, the scattering coefficient usually is much greater than the absorption coefficient. Thus, in the experiments, in order to measure the scattering coefficients, the absorption coefficient can be ignored when we only have

samples with scattering particles. Assuming that μ_a is zero, lead to an expression for scattering coefficient:

Equation 1.18

$$\mu_s = \left[\ln\left(\frac{I(z)}{I_0}\right) \right] \Big/ z$$

This equation alongside the optical setup, which will be shown in the next part, will help us to approximate μ_s in purely scattering media.

The optical properties associated with tissue types in human body are related to both location and direction of the scattered beam from the tissue [12]. Anisotropy of scattering g is the factor that can illustrate the direction of scattering. If θ is the angle of scattering, anisotropy of scattering can be defined as the average cosine of θ:

Equation 1.19

$$g = \langle \cos\theta \rangle$$

 Note that we ignore azimuthal scattering in this simple relationship. For a more complete description of g, a phase function should be defined which gives the probability density function of scattered light in different angles [13] over 4 steradians. This phase function is a measure of anisotropy of scattering and can give intensity for each direction. If g =1.0, the scattering angle is zero and the beam of light will pass through the medium without changing direction and we will have exact forward scattering. If $g = 0$, the mean scattering angle is 90° and the scattering is isotropic.

It is common to employ a phase function when discussing scattering anisotropy. The Henyey-Greenstein function [14, 15] is commonly employed in biological applications.

37

This function introduces a phase function with parameter g, which can be varied from -1 to 1. The scattering in this range varies from backscattering to forward scattering. The Henyey-Greenstein function is defined as:

Equation 1.20

$$p(\theta) = \frac{1}{4\pi} \frac{1-g^2}{\left(1+g^2-2g\cos\theta\right)^{3/2}}$$

Which $p(\theta)$ is the probability density function and θ is the angle between the direction photon travels before the scattering event and after that. So, the anisotropy of scattering is defined as:

Equation 1.21

$$g = \langle\cos\theta\rangle = \int_0^\pi \cos(\theta) P(\theta) 2\pi \sin(\theta) d\theta$$

Different methods were developed to calculate the scattering anisotropy. The most common technique, which we are using in our work, is the goniometry. In the experimental design section we will discuss about this method.

The absorption coefficient is another optical property, which we are going to address its effects on laser speckle contrast imaging [4]. Analogous to the scattering coefficient, the absorption coefficient is a measure of the inverse mean distance a photon travels in a medium before it is absorbed. A low absorption coefficient means that there is a small amount of absorption of light for that specific tissue. This parameter depends on the material that is illuminated and the wavelength of light. The absorption coefficient is not constant for different wavelength.

The absorption coefficient can be calculated using this equation:

Equation 1.22

$$\mu_a = \varepsilon C \ln(10)$$

In this equation ε is the extinction coefficient and C is the concentration of the chromophore(s). Also, Lambert-Beer's law can help us to measure absorption coefficient by removing all the effects related to scattering. Assuming no scattering leads to the absorption coefficient using the equation below:

Equation 1.23

$$\mu_a = \left[\ln\left(\frac{I(z)}{I_0} \right) \right] \Big/ z$$

As we mentioned earlier, optical properties could have effects on laser speckle contrast imaging [12]. We know that if there are some moving particles in the imaging area, the contrast decreases. Thus, there is a relationship between the number of moving particles or concentration and the resultant contrast. In this part of our work we will change the number of moving scatterers and see the result. Changes in scatterer concentration will change the optical (scattering) properties. Herein, we will consider the effects of optical properties on the laser speckle contrast imaging. Scattering coefficient, absorption coefficient and anisotropy of scattering are the optical properties we are going to address their effects on LSCI.

Chapter 2

Samples and Experimental setup

2.1 Introduction

Laser speckle contrast imaging (LSCI) is a non-invasive method to monitor blood flow. A two dimensional map of blood flow is produced by using this method in a relatively short time [1]. The theory is based on inferring a temporal correlation time from the speckle contrast and then finding a relationship between this time constant and the flow velocity. There are several outstanding issued regarding this method that will be investigated in this work. In order to examine the effects of optical properties on LSCI we need appropriate samples and experimental setup. In this chapter we will introduce the samples we used in our experiments and the different optical setup for each set of experiment.

2.2 PVA and lipid samples to measure scattering coefficient

A key component of this research was developing suitable phantom materials that would mimic the absorption and scattering properties of blood and biological tissue. Poly Vinyl Alcohol (PVA) and lipid solutions with varying lipid concentrations were two materials we initially investigated as phantom materials.

Optimizing the number of freezing and thawing cycle of PVA solutions is a technique to vary the scattering properties of PVA. Our initial goal was to create PVA samples with optical properties similar to the properties of the tissue in human female breast.

The simple process of freezing and thawing of the PVA samples results in a gel sample whose mechanical strength gradually rises with the number of freezing and thawing cycles. By increasing the number of cycles, the sample changes from a clear gel to an opaque one. A firming phenomenon happens during these processes and makes the sample rigid and turbid.

An appropriate amount of PVA and water was heated to gain a solution with concentration of 20% by weight [37]. A temperature of 95 degrees of Celsius is needed and the solutions were heated for two hours with constant stirring. The solutions were left standing for 2 -3 hours in order to let all the bubbles move to the surface of the solution. Finally, the solutions were placed in a freezer at -20 degrees Celsius for approximately 12 hours. Repeated freezing and thawing cycles increased both the optical scattering and the mechanical strength and stiffness of the samples.

We made samples with 0 to 4 freeze-thaw cycles and did the experiments using these samples using red diode laser with a 660nm center wavelength for these experiments, we needed thin samples. Thus, we made hand-made cuvettes and used them during the experiments.
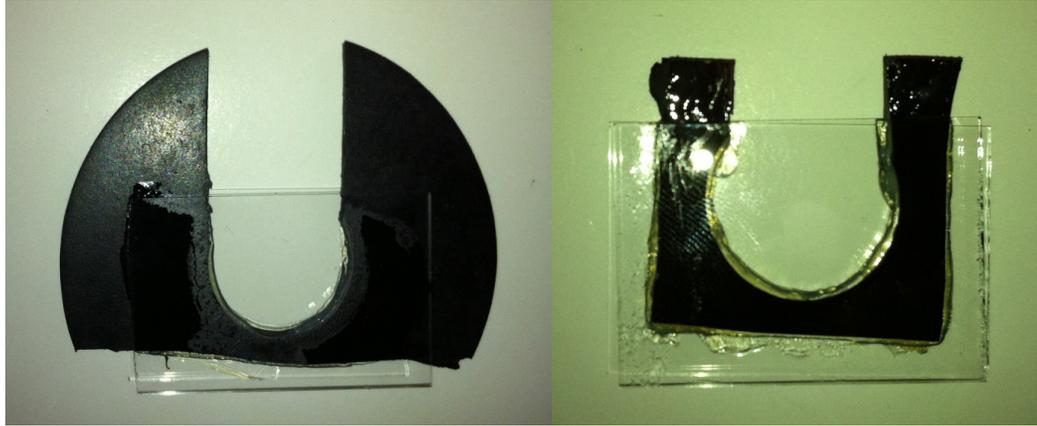
Figure 6: hand-made cuvettes

We made lipid phantoms by adding different milk concentration to DI water. The initial lipid concentration of milk was 2% and we made 10 different phantoms of 0.1% lipid to 2% lipid phantoms.

These samples were actually replaced later on with new samples called Luxil microspheres and a plastic bar instead of PVA samples. The reason we changed the lipid samples was because we wanted to be able to make 121 different samples and keep them for a long time to be able to redo the experiments several times. The lipid solutions did not let us keep them for more than a few days. Thus, we switched to a new type of microspheres, which are glass microspheres with brand name Luxsil. These microspheres have diameter of 9-13 microns with the average diameter of 11.7 micron, which is close to the diameter of red blood cells. We made our solutions with these new particles. The results will be shared in the following chapters. Also, we used a plastic bar instead of PVA samples, since our goal was to keep all the other experimental parameters constant, but the optical properties of PVA samples change during the time. So, a plastic bar sounded like a better idea to mimic

the tissue in the imaging section. Luxsil microspheres and the new experimental setup will be discussed in more detail later in this work.

2.3 Experimental design

2.3.1 Optical setup to measure optical properties

The optical properties were being measured by ballistic transmission. A simple optical setup for scattering coefficient measurement is shown in this image:
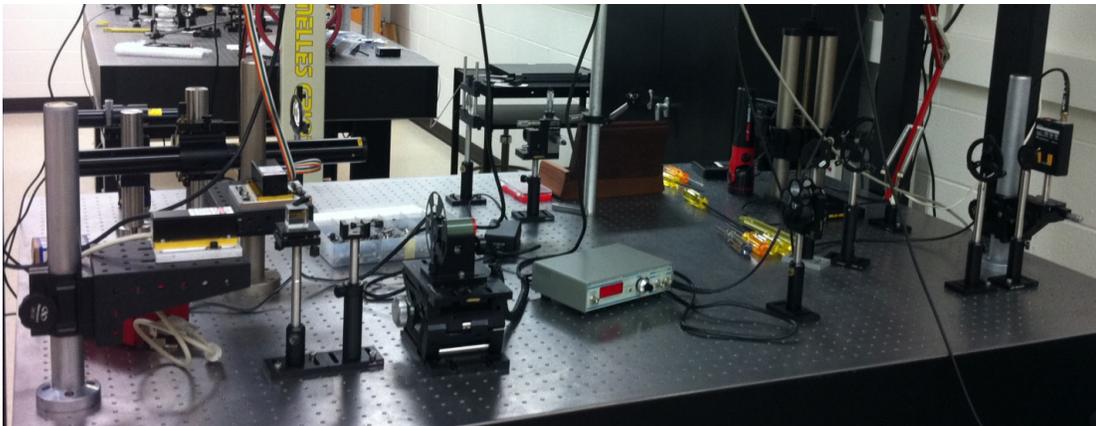
Figure 7: Optical setup for scattering coefficient measurements.

In this system, we use a red diode laser source of 660nm wavelength. A synchronous detection scheme was used employing a lock-in amplifier and an optical chopper. The purpose of this detection scheme was to improve the signal-to-noise ratio. An added benefit of this detection scheme was that the room lights were able to be left on. Neutral density filters were used in this optical setup to decrease the intensity of light impinging

on the detector, not only to prevent saturation, but also because the high intensity can damage the detector. A sensitive detector is needed to detect low intensity beams in the case of higher FTC samples. Also, an aperture was placed immediately in front of the detector so that only unscattered light reached the detector.

The goal of these experiments was to calculate scattering coefficient. Scattering coefficient μ_s can be obtained from a modified Lambert-Beer's law:

Equation 2.1

$$I(z) = I_0 \left[\exp\left(-(\mu_a + \mu_s)z\right) \right]; \qquad \mu_a = 0$$

Equation 2.2

$$\mu_s = \left[\ln\left(\frac{I(z)}{I_0}\right) \right] \Big/ z$$

The equation above shows the relationship between the output voltage and μ_s. It is necessary to mention that z is thickness of the sample and I_0 is the intensity with just a cuvette filled with water in the experiment.

2.3.2 LSCI Experimental Setup

According to what was stated in the previous sections, our objective in this part is to consider the effects of scattering coefficient on the contrast or generally on laser speckle contrast imaging. In order to investigate this effect, we use the LSCI optical setup using a plastic bar sample with a capillary on top which a liquid phantom ran through. In this part, other parameters during the experiment held constant and the only parameter, which is

going to be changed, is the scatterer concentration. Changing the scatterer concentration will change the scattering coefficient and as a result, contrast variation will be examined. The following image (Figure 8) illustrates the laser speckle contrast imaging optical setup used in our lab. As this image shows, a solid plastic phantom with glass tubing on top is used as the sample, which is illuminated by a laser diode of 660nm wavelength. The sample is imaged using am 8-bit Point Grey Dragonfly CCD camera. The magnification and f/# of the camera held constant during the experiments. The magnification was 2 and camera's f/# was fixed on f/32. The fluid phantom solutions run through the tubing by means of a mini peristaltic pump and this pump controls the fluid flow, which was held constant for the experiments. Neutral density filters are used in this optical setup to control the intensity of the incident light to prevent camera saturation.
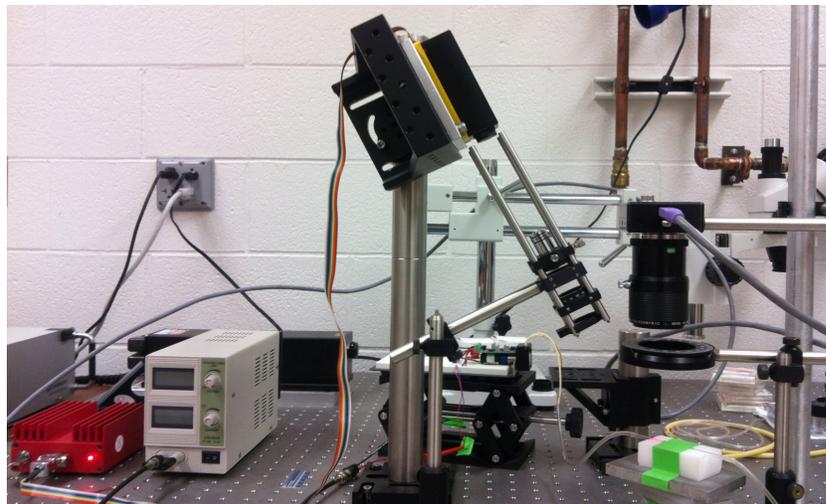

Figure 8: LSCI optical setup.

2.3.3 Imaging setup in detail

A camera with a macro zoom lens was mounted to a vertical stage, observing the sample normally. The camera was focused at the center of the glass tube. A laser diode with a collimation kit is then set up so that divergent laser light illuminates the object. In this work, red laser light was used because it was easier to demonstrate how to build the system, but infrared laser light could just as easily be used and would have the additional benefit of penetrating deeper in tissue. Also, with appropriate filters in front of the camera to block visible light, infrared light could be used with the room lights on.

In laser speckle contrast analysis, a laser illuminates the sample under test. The scattered light from the sample returns to a camera sensor and produces a dynamic speckle pattern. LSCI is a predominantly single scatter technique. The camera records the intensity at the detection point and the aperture of the lens controls the speckle pattern.

2.4 Luxil microspheres samples

In order to conduct these experiments repeatedly and efficiently, we wanted to make solution to be able to keep them for a longer time than lipid or PVA samples. We started our experiments using those samples, but since they are not convenient to be used for different experiments during days, we needed to come up with a new scattering liquid phantom. We choose glass microspheres with the brand name of Luxsil. Luxsil is cosmetic hollow glass microspheres from Potters Company. The spherical shape of these microspheres, their diameter and the color made them appropriate to use as scatterers. In our experiments the scatterers should mimic red blood cells in terms of physical dimensions as well as optical properties. Luxsil, with the diameter of 11.7 microns is approximately

the same physical dimension as red blood cells. The table below shows the technical information about Luxsil:

Table 1: Luxsil microspheres technical information

Shape	Sphere
Density	1.1 g/cc nominal
Size	9-13 micron
Color	White
Crush strength	>10,000 psi
INCI Name	Calcium aluminium borosilicate
Chemical Resistance	Low alkali leach, insoluble in water

2.4.1 Mie scattering calculator to predict concentration

 In this section, we use Mie Theory to estimate the optical scattering properties of the Luxsil microspheres. We used the well-established Mie calculator by Scott Prahl from the Oregon Medical Laser Center (omlc) website to calculate the scattering coefficient of the microspheres. The diameter of these microspheres and their density are known from the spec sheet provided by the manufacturer. Using this information and the calculator we wanted to solve the inverse problem and determine the necessary concentrations of the Luxsil solutions to approximate the scattering coefficient whole blood at different hematocrit levels. After these calculations, the solutions with different concentrations were

be made in the lab and the corresponding scattering coefficient was measured. At the end, comparing the results from the calculator and the lab will be our point of interest.

2.4.2 Mie Theory a model for optical properties in tissue

Mie theory can be introduced as a model to describe the optical properties. It actually describe slight scattering by particles. "Particles" in this case means a combination of a region with refractive index of n_p surrounding by another region with the refractive index of n_m. Electron oscillation in the molecules causes a dipole re-radiation pattern that leads to a strong net source of the scattered beam. These scattering radiations do not cancel each other in all but results in both constructive and destructive radiation patterns. Thus, particles scatter the incident light beam in various directions and with varying efficiency. The ratio of the refractive indices between the particles and the surrounding material is called "magnitude of refractive index mismatch":

Equation 2.3

$$n_r = \frac{n_p}{n_m}$$

The other important parameter we can define is the "size of the surface of refractive index mismatch" which is the ratio of the circumference of the sphere to the wavelength of the light in the medium:

Equation 2.4

$$x = 2\pi a \left(\frac{\lambda}{n_m} \right)$$

To calculate the scattering coefficient using Mie theory calculation, first, the efficiency of scattering is defined as:

Equation 2.5

$$\sigma_s = Q_s A$$

Which Q_s in this equation is efficiency of scattering, σ_s is the cross-sectional area of scattering and A is the true geometrical cross-sectional area of the particles.


Geometrical cross-section
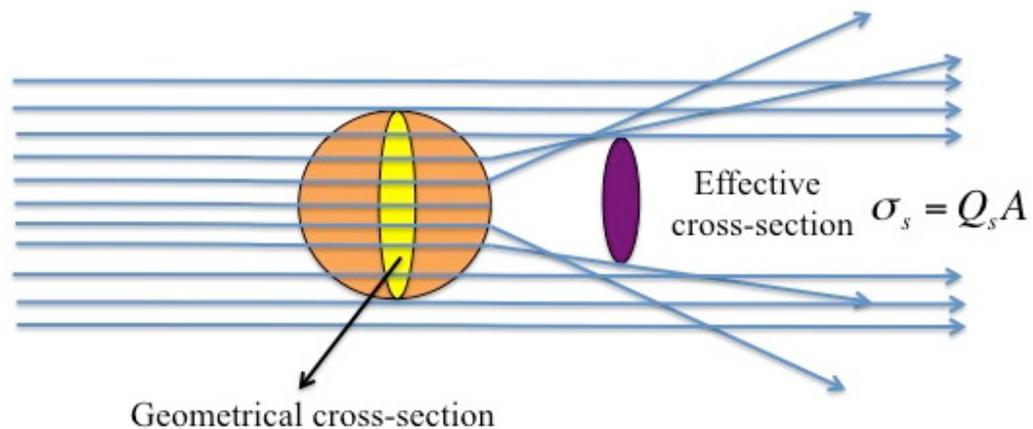
Figure 9: geometrical and effective cross section of a scattering phenomenon

Finally, the scattering coefficient which introduced the average distance photon travels in tissue before being scattered, is shown as:

Equation 2.6

$$\mu_s = \rho_s \sigma_s$$

which ρ_s is the scatterer number density and σ_s is the geometrical cross-sectional area of particles.

2.4.3 Math behind Mie scattering

Consider the "scattering plane" as a three dimensional plane which is defined by an observer. Then, consider a source and a spherical particle. When the incident light reaches the particle it will scatter and shrink to its components. These components can be parallel or perpendicular to the scattering plane. As shown in this figure:
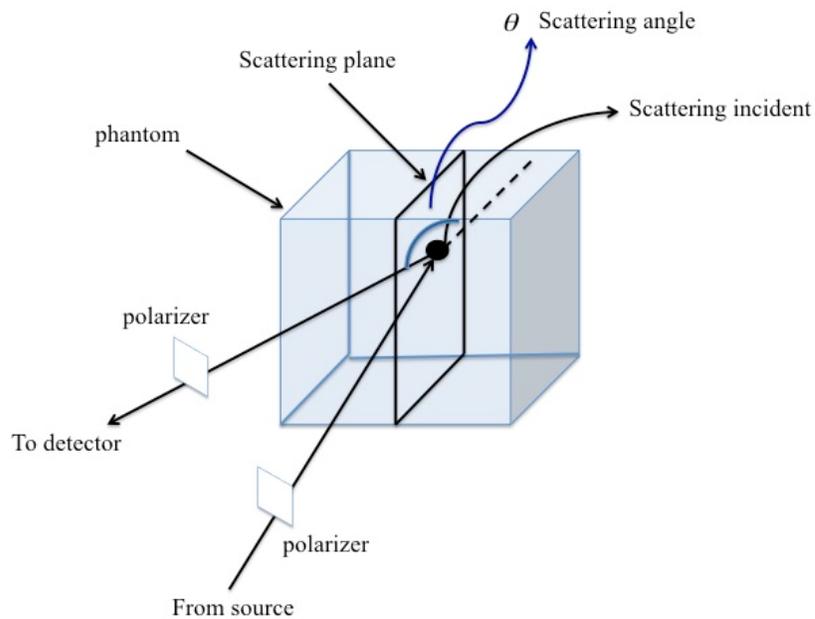

Figure 10: The scattering three-dimensional plane

The scattering matrix depicts the association between incident and scattered components, which are perpendicular or parallel to the scattering plane in the "far field":

Equation 2.6

$$\begin{bmatrix} E_{\parallel s} \\ E_{\perp s} \end{bmatrix} = \frac{\exp\left(-ik\left(r-z\right)\right)}{-ikr} \begin{bmatrix} s_2 & s_3 \\ s_4 & s_1 \end{bmatrix} \begin{bmatrix} E_{\parallel i} \\ E_{\perp i} \end{bmatrix}$$

In the above expression, the exponential term, is a transport factor which is related to the distance between observer and scatterer. The transport factor is constant if the scattered light is measured from a constant distance from the scatterers. In this case:

Equation 2.7

$$\frac{\exp\left(-ik\left(r-z\right)\right)}{-ikr} = cons\tan t$$

For the observation in the far field at a distance r from the particle of diameter d, when $kr \rangle\rangle n_c^2$, $k = \frac{2\pi}{\lambda}$ and $n_c = \frac{d}{\lambda}$ the scattering elements of s_1 and s_2 are equal to zero.

In practical experiments we actually measure the intensity. In order to measure the intensity, we use this equation:

Equation 2.8

$$I = \langle EE^* \rangle = \left(\frac{1}{2}\right) a^2$$

where $E = a\exp\left(-i\phi\right)$. ϕ is phase and a is amplitude. So, the final equation will be:

Equation 2.9

$$\begin{bmatrix} I_{\parallel s} \\ I_{\perp s} \end{bmatrix} = cons\tan t \begin{bmatrix} s_2 & 0 \\ 0 & s_1 \end{bmatrix} \begin{bmatrix} I_{\parallel i} \\ I_{\perp i} \end{bmatrix}$$

According to the mathematics we introduced above, we can write a code to do the calculation of scattering coefficient using Mie theory. Also, there are some already written codes, which are on-line such as Wiscombe's code [http://omlc.org/software/mie/] that can be used to do the calculations. But, Scott Prahl wanted to be able to do the calculations without needing to compile Mie code each time, he created an interactive web page that allows everyone to do their own Mie scattering calculations.

This interactive webpage called Mie theory calculator is available on Oregon Medical Laser Center's website (http://omlc.org/calc/mie_calc.html). In this work we used this calculator to measure the scattering coefficient of Luxsil microspheres solutions with different concentrations.

2.4.4 Calculations using Mie calculator

The parameters used in the Mie calculator for the Luxsil microspheres are listed below. The third column in the first table shows the units of each parameter.

The second table illustrates the result of Mie calculator for the specific concentrations. The anisotropy of scattering was given by the Mie calculator according the particles technical properties.

Table 2: Mie Scattering Calculator input parameters.

Sphere diameter	11.7	Micron
Wavelength in vacuum	0.660	Micron
Index of refraction in medium	1.5	
Real index of sphere	1.51	

Imaginary index of refraction	0	
Number of angles	100	
Concentration	?	Spheres/cubic micron

Table 3: results from Mie scattering calculator.

Concentration is the number of spheres per cubic micron in this table.

Concentration	μ_s(1/mm)	g	μ_s'(1/mm)
0.00001	0.62615	0.99923	0.8223
0.00002	1.2523	0.99923	0.8381
0.00003	1.8785	0.99923	0.8458
0.00004	2.5046	0.99923	0.8534
0.00005	3.1308	0.99923	0.8610
0.00006	3.7569	0.99923	0.8686
0.00007	4.3831	0.99923	0.8763
0.00008	5.0092	0.99923	0.8839
0.00009	5.6354	0.99923	0.8915
0.00010	6.2615	0.99923	0.8989

which, g (anisotropy of scattering) is given by Mie calculator.

3.4.5 Formulation of samples

According to the information we have for the Luxsil, we are able to estimate the mass of one particle using the simple math below:

Equation 2.10

$$d_{microsphere} = 11.7\mu$$

$$V_{microsphere} = \frac{4}{3}\pi\left(\frac{11.7\mu}{2}\right)^3 = 838.177\mu^3$$

$$Density = 1.1 \times 10^{-12}\, g\big/\mu^3$$

$$Density = \frac{m}{V} \Rightarrow 1.1 \times 10^{-12}\, g\big/\mu^3 = \frac{m}{838.177\mu^3}$$

$$\Rightarrow m = 921.99 \times 10^{-12} g$$

The concentration using in Mie calculator is considered as spheres per cubic micron. Having the mass of one particle will help us to calculate the amount of Luxsil we need for each solution with a specific concentration.

The fluid phantoms were mixed in 90mL containers. In order to have the amount of Luxsil powder for solutions we need to multiply the mass of spheres needed by the volume in cubic microns. Table below shows the concentrations we formulated in g/mL:

Table 4: Calculated concentration of Luxsil solutions.

Concentration (Spheres/cubic micron)	Amount of Luxsil (mg/mL)	Concentration
0.00001	0.00922	0.92%
0.00002	0.01844	1.84%
0.00003	0.02766	2.76%
0.00004	0.03688	3.68%
0.00005	0.0461	4.61%
0.00006	0.05532	5.53%
0.00007	0.06454	6.45%
0.00008	0.07376	7.37%
0.00009	0.08298	8.29%
0.00010	0.0922	9.22%

In order to make the samples, we multiplied the amount of Luxsil in this table with the volume and add that amount of Luxsil to the DI water. The resultant concentrations in the above table is the ratio of the mass of Luxsil microspheres to the mass of water. Figure (12) shows some sample phantoms we made in the lab:

Figure 11: phantom solutions of Luxsil microspheres

2.4.6 New experimental setup

In the process of improving our experimental design, we developed a new LSCI setup. We placed the laser, microscope objective and a polarizer on a small optical breadboard and the plate mounted on an articulated arm, which made the system easier to move in order to fix the alignment. The image below (Figure 13) shows the new optical system.
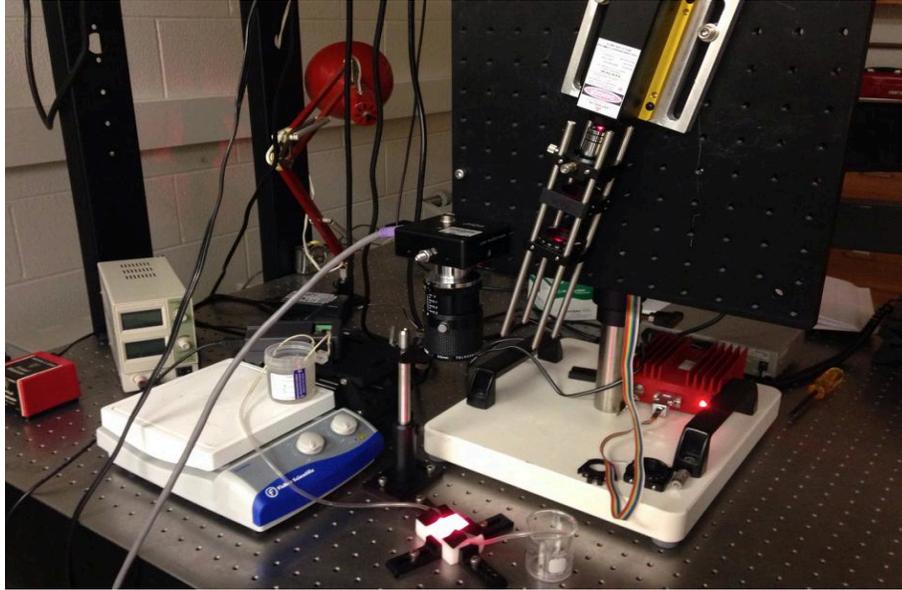
Figure 12: Final LSCI setup

2.5 Absorption coefficient

In order to measure absorption coefficient we used India ink as absorber. We added 10 different amounts of India ink to a Luxsil solution with known scattering coefficient. The goal here was to mimic the absorption coefficient of blood with various hematocrit levels. Using ballistic transmission we measured the attenuation coefficients of the new samples. Then, we calculated the absorption coefficients of the samples by subtracting the scattering coefficient of the Luxsil solution from the attenuation coefficient. According to Lambert-Beer's law:

Equation 2.11

$$I(z) = I_0 \exp(-\mu_t)$$

And we also have:

Equation 2.12

$$\mu_t = \mu_a + \mu_s$$

We have scattering coefficient and total attenuation coefficients from the experiments.

So, the absorption coefficient would be:

Equation 2.13

$$\mu_a = \mu_t - \mu_s$$

Chapter 3
Results

3.1 Introduction

As we mentioned in previous chapters, the goal in this work was to measure optical properties of some samples and find the effects of these optical properties on LSCI contrast values. Samples and experimental design was introduced in the previous chapters and now it is time to depict some results. The results of the optical properties measurements come first and then we will see how these properties effect contrast in LSCI images.

3.2 Scattering Coefficient Measurements

3.2.1 PVA samples

In order to investigate the effects of optical properties on LSCI, as a first step, the measurement of these optical properties is necessary. Scattering coefficient can be calculated in the lab for PVA and lipid solution samples using ballistic transmission. PVA samples are the samples considering them as tissue and lipid solutions are indicating blood with different hemoglobin concentration [44]. We made PVA samples in the lab and did the process of freezing and thawing them for several times for different samples.

The experiments were done for 5 freeze-thaw cycles (0 to 4) for four different samples. The scattering coefficient was measured using Lambert-Beer's law. The plot below shows

scattering coefficient versus number of freeze-thaw cycles for four different samples. Each set of dots with the same color introduces a sample. As can be seen from this plot, by increasing the number of freeze-thaw cycles the scattering coefficient increases.
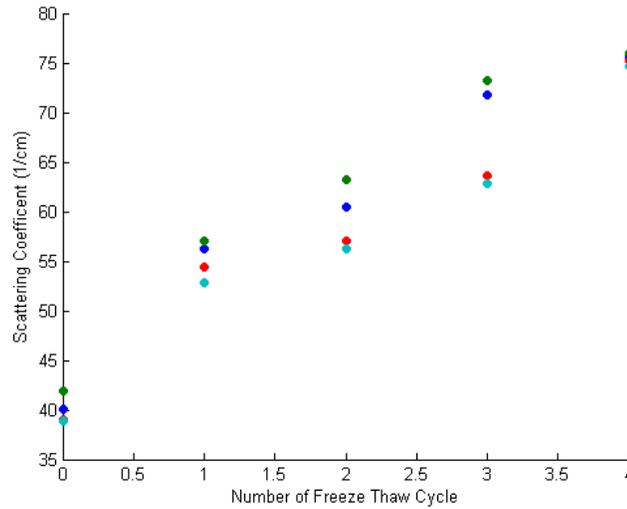

Figure 13: Scattering Coefficient $\left(\mu_s\right)$ for different freeze-thaw cycle's samples.

3.2.2 Lipid solutions

In order to consider optical properties of blood, we decided to use different lipid solutions. This approach helps us to guess the optical properties of blood using these solutions.

For this purpose, at first, we made a solution with 0.04% lipid concentration and continued making these solutions by increasing the percentage of lipid. At the end, we did the experiment for 2% lipid concentration and calculated the scattering coefficient for these solutions. Results are shown in this curve:
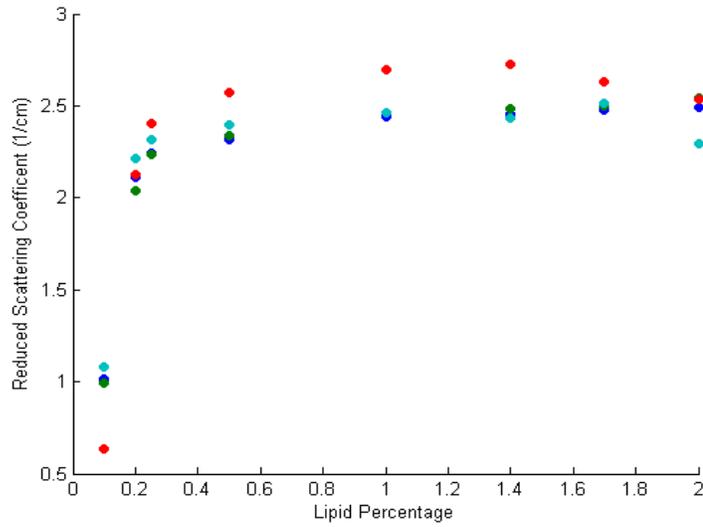
Figure 14: Reduced Scattering coefficient $\left(\mu'_s\right)$ for different lipid solutions.

The following table demonstrates the numerical values of scattering coefficient and reduced scattering coefficient measured through the experiments. Furthermore, *g* was measured for lipid particles using the goniometry method and is equal to 0.76. Also, reduced scattering coefficient was calculated using this Equation 3.1[33]:

Equation 3.1

$$\mu'_s = \mu_s (1-g)$$

Table 5: Scattering coefficient and reduced scattering coefficient for the solutions with different lipid concentrations (g=0.721).

Percentage	μ_s (1/mm)	μ'_s (1/mm)
0.04%	0.2	0.0558

0.1%	1.2	0.3348
0.2%	2.56	0.7142
0.4%	2.65	0.7393
0.6%	2.77	0.7728
0.8%	2.9	0.78
1%	3.04	0.8091
1.4%	3.21	0.8955
1.6%	3.22	0.8983
1.7%	3.38	0.9430
1.8%	3.42	0.9541
2%	3.60	1.0044

During this research, we examined techniques to take off the behavior of skin and blood by making PVA phantoms produced with various numbers of freeze-thaw cycles and lipid solutions with various concentrations [34]. As proof of concept of such a PVA phantom, we had created a layered phantom composed of a 2mm layer of PVA that had undergone four freeze-thaw cycles. By increasing the number of cycles, optical scattering and mechanical stiffness are increased. As we can see from the curves, by increasing the number of cycles μ_s increases. The mechanism behind the changing properties is the gradual change in the gel from an amorphous to crystalline polymer. The crystalline nature remains in place even following thawing. After the thawing process, the porosity also increases due to the melting of water phase, leading to increase turbidity.

3.3 Scattering anisotropy, *g*, measurement using goniometry

For anisotropy of scattering measurements we used a set of samples with different number of freeze-thaw cycles. A goniometry method was utilized in the experiments. We made three different samples; the freezing and thawing process was done three times for each sample and the goniometry measurement repeated three times for each freeze-thaw cycle of each sample. It means at the end we had nine sets of data for each freeze-thaw cycle sample. A curve fitting method using the Henyey-Greenstein phase function was applied to each set of data to have the final phase function. Curves below show the actual data collected in the lab and the corresponding fitted curve to that set of data. Left curves are for a single set of data for each sample and right curves show the nine sets of data for that sample with the final curve averaging over the other nine curves.
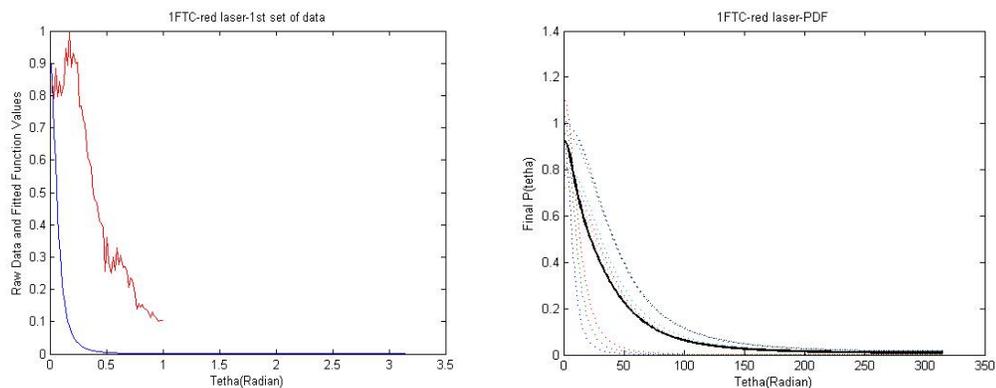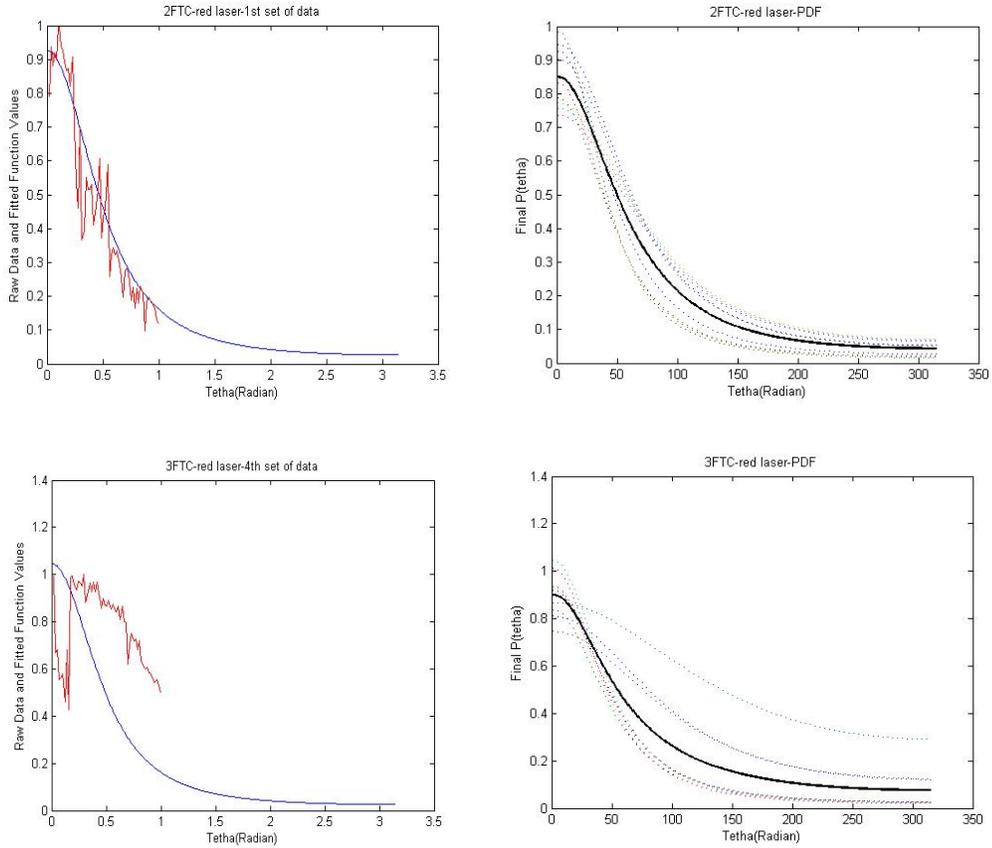
Figure 15: Raw data and the fitted curve (left figures) and the final curve (right figures)

for 3 different freeze-thaw cycles samples.

This table shows the results of anisotropy of scattering experiment for three different

freeze-thaw cycle samples:

Table 6: Anisotropy of scattering for 3 different freeze-thaw cycle's samples.

No.	1 FTC	2 FTC	3 FTC
1	0.9159	0.7303	0.5269
2	0.8861	0.741	0.5336

3	0.8593	0.7557	0.5343
4	0.8163	0.7813	0.5485
5	0.7285	0.7833	0.5671
6	0.722	0.6793	0.5478
7	0.6945	0.6417	0.3082
8	0.6901	0.5463	0.3051
9	0.6845	0.5645	0.3795
	g=0.77	**g=0.69**	**g=0.47**

3.4 Effects of scattering coefficient on contrast

As we can see from the results of the last section, increasing the lipid concentration increased the scattering coefficient. Increasing the lipid concentration means that we have more lipid molecules in the imaging area. So, we will have more scattering and also a larger scattering coefficient. Having a large scattering coefficient shows that the probability of scattering is high in that regime and the contrast will be lower in this case.

For this purpose, the LSCI optical setup was used in the lab [35]. The speckle pattern and the resultant contrast image are:
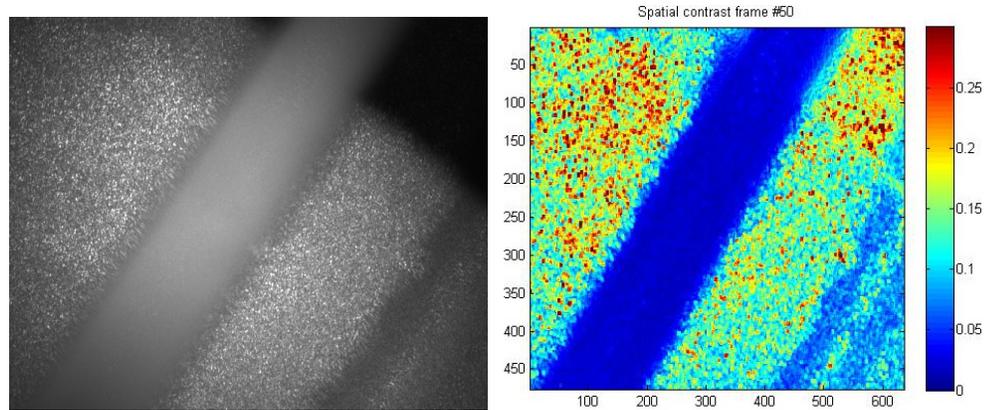
Figure 16: The speckle pattern (left) and the resultant contrast image (right).

3.4.1 Representative Results

In the figure below, the first image shows an example of a typical raw speckle image and a converted speckle contrast image that should be generated when using the software to examine in the brain [36]. For visualizing changes in blood flow, it is easier to have the software generate relative maps of blood flow. The second figure shows a typical series of relative blood flow images during a transient increase in blood flow that travels across the field of view. The blue color represents a decrease in contrast when we have motion in the imaging area. The yellow color indicates that there is no movement in the imaging area. All the parameters held constant during the experiment and just the lipid concentration was supposed to change. This phenomenon checked for eight lipid solutions with different lipid concentrations. Images below are the four examples of the results and show the change in contrast due to changes in scattering coefficient:
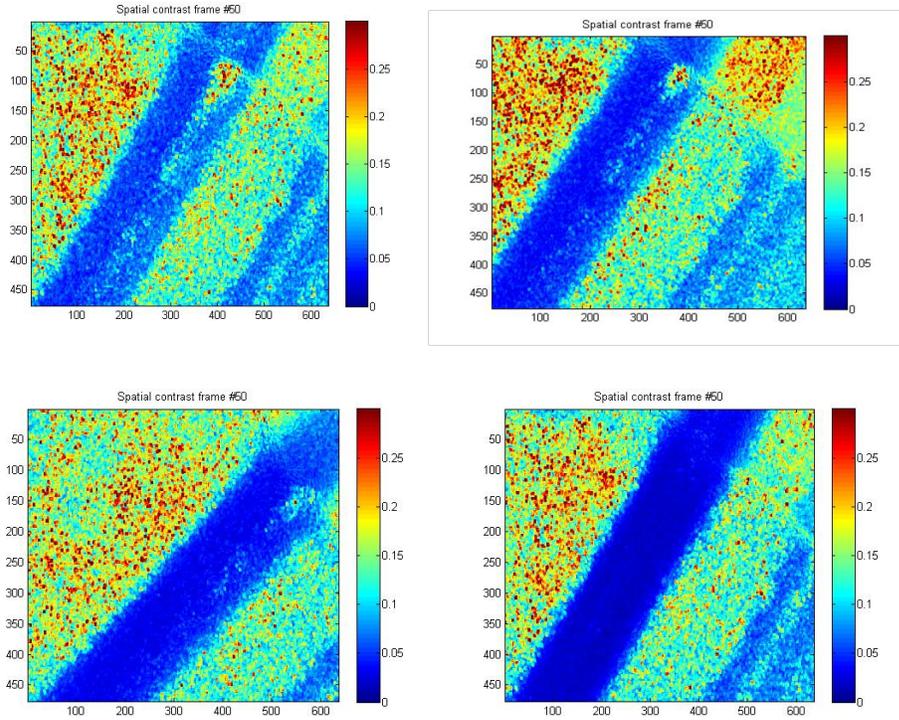
Figure 17: The contrast image for different lipid solutions with different milk

concentration (The top left image is for water, the top right image is for 0.1%, the bottom

left is for 1% and the bottom right is for 2% lipid solutions).

The top left image is the contrast when we had water running in the tubing. Also, we

calculated the local contrast with a MATLAB program for all the images and the resultant

curve depicted below:
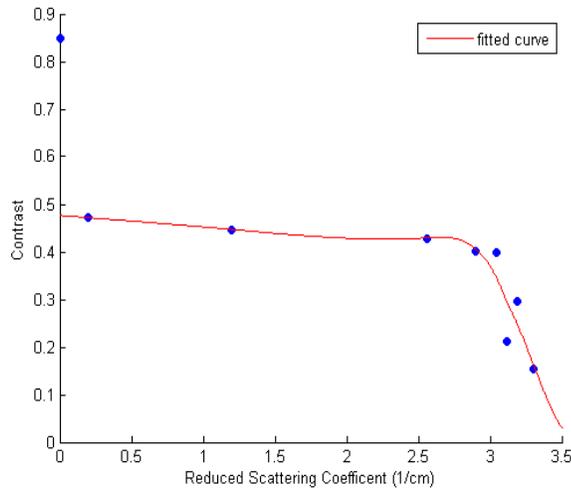
Figure 18: Contrast vs. reduced scattering coefficient.

According to this curve, by increasing the scattering coefficient contrast decreases. Thus, the scattering coefficient of the moving fluid influences the contrast values in LSCI and an increase in scattering coefficient leads to a decrease in contrast. One of the parameters which held constant was the flow and as can be seen from the images and the curve, identical flow speeds will result in different contrast values when the scattering coefficient changes. Each of those images have static and moving scatterers which they are in the same depth of field.
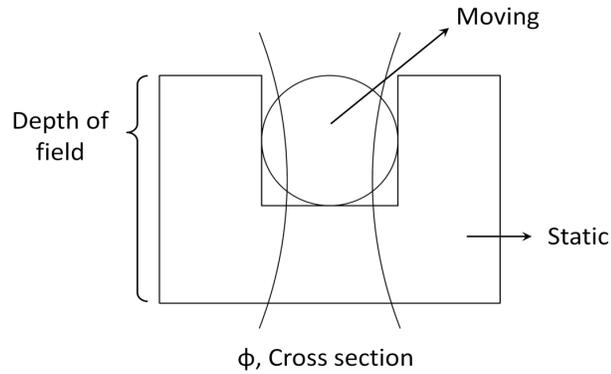
Figure 19: Sample's cross-section.

The image above shows the cross section of our sample. The moving and static part of the sample are in the same depth of field. By increasing the percentage of moving scatterers or increasing scattering coefficient, the influence of static scatterers on the contrast is reduced. Therefore, the contrast in the moving part is lower when the scattering coefficient is higher. Another idea to address the effects of scattering coefficient on contrast is to change the static scatterers. In the previous part we tried to change the number of moving particles and address the effects of that on LSCI. According to this new idea, we can change the number of static scatterers using differnet numbers of tapes on top of the sample and test the effects of different numbers of scatterers.

3.5 Absorption coefficient results and error propagation

3.5.1 Error propagation

When we suppose to measure the addition or subtraction of some quantities with different uncertainties, the final error propagation should be calculated in a certain way. We cannot simply add or subtract the uncertainties since it will be actually an overestimate of the

uncertainty in addition or subtraction. If the measured quantities are a and b with uncertainties δa and δb, the error for final quantity of Q which is defined as:

Equation 3.2:

$$Q = a \pm b$$

Will be calculated using equation below:

Equation 3.3:

$$\delta Q = \sqrt{(\delta a)^2 + (\delta b)^2}$$

In our case, we were measuring optical properties, μ_t, μ_s and μ_a. We measured μ_t and μ_s with known uncertainties $\delta\mu_t$ and $\delta\mu_s$. In order to measure the error for μ_a, $\delta\mu_a$, we can follow equation 3.4 since we have:

Equation 3.4:

$$\mu_a = \mu_t - \mu_s$$

Then $\delta\mu_a$ would be:

Equation 3.5:

$$\delta\mu_a = \sqrt{\delta\mu_t^2 + \delta\mu_s^2}$$

Table 7 shows the error propagation for 10 different μ_t and 10 corresponding μ_as. In this table μ_s and $\delta\mu_s$ are $\mu_s = 0.79 mm^{-1}$ and $\delta\mu_s = 0.04 mm^{-1}$.

Table 7: Error propagation calculations (mm^{-1})

$\times 10^{-4} \rightarrow$	0.1	0.2	0.4	0.6	0.8	1	1.2	1.4	1.6	1.8
μ_t	4.8051	4.8087	4.80258	4.832	4.8391	4.844	4.8448	4.8519	4.888	4.8954
$\delta\mu_t$	0.042	0.027	0.061	0.04	0.032	0.023	0.037	0.055	0.036	0.071
μ_a	0.0051	0.0087	0.0258	0.032	0.0391	0.044	0.0448	0.0519	0.088	0.0954
$\delta\mu_a$	0.058	0.048	0.072	0.056	0.051	0.046	0.054	0.068	0.053	0.043

References

1. Y. Tamaki, M. Araie, E. Kawamoto, S. Eguchi and H. Fujii, Non-contact, two-dimensional measurement of retinal microcirculation using laser speckle phenomenon, Inv.
2. Adel Belouchrani, Moeness G. Amin, Blind Source Separation Based on Time-Frequency Signal Representations. 1053-587X/98. 1998 IEEE.
3. Michael S. Patterson, B. Chance, and B. C. Wilson, Time resolved reflectance and transmittance for the non-invasive measurement of tissue optical properties. Applied Optics, Vol. 28, No. 12, 15 June 1989.
4. Goodman J. W., Statistical Optics. , Wiley, New York ((1985)).
5. R. A. J. Groenhuis, H. A. Ferwerda, and J. J. Ten Bosch, Scattering and Absorption of turbid materials determined from reflection measurements. Applied Optics, Vol. 22, No. 16, 15 August 1983.
6. Christian J. M. Moes, Martin J. C. van Gemert, Willem M. Star, Johannaes P. A. Marijnissen, Scott A. Prahl. Measurements calculations of the energy fluence rate in a scattering and absorbing phantom at 633nm. Applied Optics, Vol. 28, No. 12, 15 June 1989.
7. Alwin Lienle, Michael S. Patterson. Determination of the optical properties of turbid media from a single Monte Carlo simulation. 1996 IOP Publishing Ltd. 0031-9155/96/102221.
8. Chin-I Lin, Marcia Baker, Robert J. Charlson. Absorption Coefficient of Atmospheric Aerosol: a Method for Measurement. Applied Optics, Vol. 12, issue 6, pp.1356-1363 (1973).
9. Michael Vorlander, Eckard Mommertz. Definition and measurement of random-incidence scattering coefficient. Elsevier Science. 200. S0003-682X (99) 00056-0.
10. Michael S. Patterson, B. Chance, and B. C. Wilson. Time resolved reflectance and transmittance for the noninvasive measurement of tissue optical properties. Applied Optics, Vol. 28, No. 12, 15 June 1989.
11. http://teaching.shu.ac.uk/hwb/chemistry/tutorials/molspec/beers1.htm
12. Thompson O., and Andrews M. Spectral density and tissue perfusion from speckle contrast measurements. In Coherence Domain Optical Methods and Optical Coherence Tomography in Biomedicine XII, Izatt J. A., Fujimoto J. G., and Tuchin V. V., Eds., Proc. SPIE. 0277-786X 6847, 68472D ((2008)).
13. Martin Hammer, Anna N. Yaroslavsky, Dietrich Schweitzer. A scattering phase function for blood with physiological haematocrit. 2001 IOP Publishing Ltd. 0031-9155/01/030065.
14. Dominique Toublanc. Henyey–Greenstein and Mie phase functions in Monte Carlo radiative transfer computations. Applied Optics, Vol. 35, No. 18, 20 June 1996.
15. Vladimir I. Haltrin. One- Parameter Two-Term henyey-Greenstein Phase Function for Light Scattering in Seawater. Applied Optics, Vol. 41, No. 6, 20 Feb 2002.

16. Oliver B. Thompson, Michael K. Andrews. Tissue perfusion measurements: multiple-exposure laser speckle analysis generates laser Doppler-like spectra, J. Biomed Opt. 15(2), 027015 (April 16, 2010). Doi: 1117/1.3400721.

17. http://www.biologie.uniregensburg.de/Biophysik/Theis/research/tutorialOnBSS.pdf

18. Boas DA, Dunn AK. Laser speckle contrast imaging in biomedical optics. J. Biomed. Opt.2010, 15:011109–011109.

19. M. D. Stern, In vivo evaluation of microcirculation by coherent light scattering, Nature 254, 50-58, 1975.

20. Briers JD, Fercher AF. Retinal blood-flow visualization by means of laser speckle photography. Invest. Ophthalmol. Vis. Sci. 1982, 22:255–259.

21. H. Fujii, Visualization of retinal blood flows by laser speckle flowgraphy, Med. Biol. Eng. Comput. 32, 302-304, 1994.

22. A. I. Srienc, Z. L. Kurth-Nelson and E. A. Newman, Imaging retinal blood flow with laser speckle flowmetry, Front Neuroenergetics 2, 128, 2010.

23. J. David Briers. Laser speckle contrast imaging for measuring blood flow. Optica Applicata, Vol. XXXVII, No 1-2, 2007.

24. A. F. Fercher and J. D. Briers, Flow visualization by means of single-exposure speckle photography, opt. Commun. 37, 326-330, 1981.

25. Donald D. Duncan, Sean J. Kirkpatrick, Can laser speckle flowmetry be made a quantitative tool? . Optical Society of America. 1084-7529/08/082088.

26. Fercher A., Briers J. Flow visualization by means of single-exposure speckle photography. Opt. Commun. 0030-4018 37, (5), 326–330 ((1981)).

27. Briers J., Webster S., Quasi real-time digital version of single-exposure speckle photography for full-field monitoring of velocity or flow fields. Opt. Commun. 0030-4018 116, (1–3), 36–42 ((1995)).

28. Sean J. Kirkpatrick, Donald D. Duncan, Wells-Gray E., Detrimental effects of speckle-pixel size matching in laser speckle contrast imaging. Opt. Lett. 0146-9592 33, (24), 2886–2888 ((2008)).

29. J. D. Briers, Laser Doppler and time-varying speckle: reconciliation, J. Opt. Soc. Am. A 13, 345-350, 1996.

30. R. Bonner and R. Nossal, Model for laser Doppler measurements of blood-flow in tissue, Appl. Opt. 20, 2097-2107, 1981.

31. Donald D. Duncan, Sean J. Kirkpatrick, J. Gladish. What is the proper statistical model for laser speckle flowmetry? In Complex Dynamics and Fluctuations in Biomedical Photonics.

32. Dunn AK. Simultaneous imaging of total cerebral hemoglobin concentration, oxygenation, and blood flow during functional activation. Opt Lett. 2003, 28:28–30.

33. Maureen Johns, Cole Giller, Dwight German, Hanli Liu, Determination of reduced scattering coefficient of biological tissue from a needle-like probe. Optics Express, Vol. 13, issue 13, pp. 4828-4842(2005).

34. I. Fredriksson, M. Larsson and T. Strömberg, Model-based quantitative laser Doppler flowmetry in skin, J Biomedical Optics 15(5), 2010, doi: 10.1117/1.3484746.

35. J. D. McKinney, M. A. Webster, K. J. Webb, A. M. Weiner. Characterization and imaging in optically scattering media by use of laser speckle and a variable-coherence source. Optical Society of America. 0146-9592/00/010004-03.

36. H. Fujii, K. Nohira, Y. Yamamoto, H. Ikawa and T. Ohura, Evaluation of blood flow by laser speckle image sensing: Part 1, Appl. Opt. 26, 5321-5325, 1987.

37. Method of producing annealed polyvinyl alcohol contact lens

38. Jones P. Simultaneous multispectral reflectance imaging and laser speckle flowmetry of cerebral blood flow and oxygen metabolism in focal cerebral ischemia. J. Biomed. Opt. 2008, 13.

39. Dunn AK, Bolay H, Moskowitz MA, Boas DA. Dynamic imaging of cerebral blood flow using laser speckle. J Cereb Blood Flow Metab. 2001, 21:195–201.

40. Fabio Scardigli, Generalized uncertainty principle in quantum gravity from micro-black hole gedanken experiment. Published by Elsevier Science, 1999, S0370- 2693 99 00167-7.

41. Donald D. Duncan, Sean J. Kirkpatrick. The copula: a tool for simulating speckle dynamics. J. Opt. Soc. Am.. 0030-3941 25, (1), 231–237 ((2008)).

42. Donald D. Duncan, Sean J. Kirkpatrick, Algorithms for simulation of speckle (laser and otherwise). In Complex Dynamics and Fluctuations in Biomedical Photonics V, Tuchin V. V. and Wang L. V., Eds. Proc. SPIE. 0277-786X 6855. 685505 ((2008)).

43. http://optics.sgu.ru/SFM_Files/2010/report/1154/index.html

44. Ayata C. Pronounced hypoperfusion during spreading depression in mouse cortex. J Cereb Blood Flow Metab. 2004, 24:1172–1182.

Chapter 4
(Paper 1)

Combined Effects of Scattering and Absorption on Laser Speckle Contrast Imaging[1]

Contribution of Authors:

Sean J. Kirkpatrick: Principal Investigator, data evaluation, writing and edition

Kosar Khaksari: Ran the experiments; Developed theory, Wrote computer code, Analyzed data, Wrote manuscript

Kosar Khaksari and *Sean J. Kirkpatrick*[*]

*Corresponding Author: E-mail: sjkirkpa@mtu.edu

Michigan Technological University, Department of Biomedical Engineering, 1400 Townsend Dr., Houghton, MI, 49931 USA

---

[1] The material contained in this chapter has been accepted for publication in the *Journal of Biomedical Optics*.

Abstract Several variables may affect the local contrast values in laser speckle contrast imaging (LSCI), irrespective of relative motion. It has been suggested that the optical properties of the moving fluid and surrounding tissues can affect LSCI values. However, a detailed study of this has yet to be presented. In this work, we examined the combined effects of the reduced scattering and absorption coefficients on LSCI. This study employed fluid phantoms with different optical properties that were developed to mimic whole blood with varying hematocrit levels. These flow phantoms were imaged with an LSCI system developed for this study. The only variable parameter was the optical properties of the flowing fluid. A negative linear relationship was seen between the changes in contrast and changes in reduced scattering coefficient, absorption coefficient and total attenuation coefficient. The change in contrast observed due to an increase in the scattering coefficient was greater than what was observed with an increase in the absorption coefficient. The results indicate that optical properties affect contrast values and that they should be considered in the interpretation of LSCI data.

Introduction

Laser speckle contrast imaging (LSCI) is a low cost and non-invasive method used to monitor blood perfusion and blood flow.[1-3] This method has a wide field of view and it is efficient and simple for full-field monitoring. The simplicity of LSCI along with its high spatial and temporal resolution allows it to be used as a powerful tool to measure, monitor and investigate living processes in near real-time. The concept behind this method lies in the mathematical relationship between moving particles (e.g., red blood cells) in the object space (i.e, the blood vessel) and the translating or 'boiling' speckles in the image plane.

When there is motion in the object space, the intensity of speckles in the image space fluctuates over time. It is these time-varying speckles in the image space that encode the motion in the object space. In time varying, or dynamic, speckle patterns, the speckle is blurred during the finite camera integration time and the spatial variation, or contrast, in intensity is thereby decreased. Contrast in LSCI is typically defined as:

$$K_r = \frac{\sigma_I}{\mu_I} \tag{1}$$

where μ_I is the mean intensity of a small window (7 x 7 in this work)[4] of pixels centered at location r and σ_I is the standard deviation of the intensity over the same window.[1] In practice, this window is slid on a pixel-by-pixel basis over the entire speckle image yielding a final spatial contrast image. In LSCI, the contrast of the speckle images is lower in regions displaying motion relative to static regions. For a polarized speckle pattern, $\sigma_I = \mu_I = 1.0$, yielding an expected value of $K_r = 1.0$.[1-3] It should be noted that this expectation, however, has its own statistical distribution.[4] When there is motion in the scattering particles, the shifting back-scattered waves coming from the moving particles will cause a temporal variation in the speckle intensity. This fluctuation results in a blur of the speckle pattern, and thereby, a reduction in K_r.

In a previous publication,[5] using arguments from mass transport theory, it was demonstrated that the contrast values calculated in LSCI are sensitive to the sum of diffusive flux and advective flux in the circulation. In that paper,[5] we argued that the diffusion with drift equation[6] adequately describes the physical phenomena to which LSCI is ultimately sensitive to. The steady state diffusion with drift equation can be written without any loss of generality in 1-dimension as

$$J_{KK} = -D\frac{\partial [c]}{\partial x} + \vec{v}_x[c], \tag{2}$$

where J_{KK} is the total flux, the first term on the right hand side (RHS) of Eq. (2), $-D\frac{\partial [c]}{\partial x}$, describes the diffusional flux, J_L, component of J_{KK} and the second term on the RHS of Eq. (2), $\vec{v}[c]$, describes the advective flux, J_G, and is the product of the velocity, $\vec{v}$, of the fluid and the concentration, $[c]$, of the scatterers suspended in it. This term, $\vec{v}[c]$, describes ordered motion of the particles and the dynamic behavior of the individual particles is unique to the individual scatterers, whereas the J_L term describes random motion of the particles and the behavior of an individual scatterer is representative of the scatterer population as a whole.[7] These two behaviors independently describe the two extreme, limiting behaviors of particle motion in a fluid and their associated correlation functions have been used to relate the observed speckle contrast to the motion of the scattering particles.[1-3]

Khaksari and Kirkpatrick[5] demonstrated a clear negative, linear relationship between both the $\vec{v}$ and $[c]$ components of advective flux and that LSCI was approximately equally sensitive to both terms. Changes in particle concentration, $[c]$, manifest as changes in the scattering coefficient, μ_s, of the fluid. A key conclusion from this study was that changes in red blood cell concentration, that is, changes in hematocrit, which result in a change in the scattering coefficient of the blood, may appear as changes in velocity and vice versa. However, a change in hematocrit also results in a change in the absorption coefficient, μ_a, due to changes in the amount of hemoglobin present in the observation

volume. The confounding effect of changes in absorption was not considered in Khaksari and Kirkpatrick.[5] Changes in observed speckle contrast in LSCI due to changes in hematocrit[8] or directly due to changes in μ_s and μ_a in phantom materials have been described by others in the literature,[9] however a systematic study of the combined effects of absorption and scattering on the observed contrast values in LSCI has yet to be reported.

Hematocrit, that is, the percentage of red blood cells in whole blood typically ranges between 38.8% and 50% in men and 39.4% - 44.5% for women in the systemic circulation.[10] However, even beyond these wide normal ranges, the hematocrit level of blood varies both naturally and under various pathological conditions. There is regional difference in hematocrit levels. For example, there is approximately a 3-fold variation in hematocrit between the capillary circulation and the systemic circulation.[11] Age and certain diseases such as anemia, leukemia, diarrhea and colon cancer can also change hematocrit level. A different level of hematocrit reflects a difference in the number of red blood cells, which function as both absorbers and scatters in a LSCI. Our motivation to examine the effects of optical properties on contrast imaging arises from the fact that different levels of hematocrit may influence contrast via a change in optical properties. The practical question, then, reduces to how do differences in optical properties, due to changes in hematocrit, effect the calculated contrast in LSCI? Furthermore, if LSCI is to be used to evaluate blood flow over a time course, or between individuals, does relative hematocrit that manifests as different μ_s and μ_a need to be considered in the interpretation of the results?

In the present work, we investigate how the optical properties of the scattering and absorption media influence speckle contrast imaging results. In order to examine this issue,

LSCI was performed on a series of flowing solutions with different reduced scattering and absorption coefficients. The hypothesis is that changing the volume fraction of scatterers and absorbers changes the reduced scattering coefficient and absorption coefficient resulting in a change in contrast. The goal of this study is to quantitatively examine the effects of optical properties on LSCI.

2. Materials and Methods

2.1 LSCI system

An LSCI system was designed and constructed specifically to examine the effects of the optical properties of the moving fluid on contrast values (Fig. 20). The system was essentially identical to the one used in Khaksari and Kirkpatrick.[5] A polarized 660nm diode laser (B&W Tek, Newark, DE, USA) was used to illuminate a section of glass tubing with outer diameter of 2mm and inner diameter of 1.5mm resting on top of a grooved plastic base. The illuminated region was approximately 20 mm in length. The glass tube, which served as our imaging window, rested in the groove. The glass tube was attached to a segment of rubber tubing, which ran, from the fluid phantom reservoir and through a mini-peristaltic pump (Instech Laboratories, Plymouth Meeting, PA, USA, model P625) that controlled the flow velocity. The mini-peristaltic pump was controlled by an Arduino microcontroller. A MATLAB GUI controlled the imaging CCD camera (Point Grey, Dragonfly, Vancouver, BC, Canada) and the pump and also calculated and saved contrast images in near real-time.

2.2 Liquid Phantoms

We used and added-absorber method to generate our flow phantoms. We initially created purely scattering phantoms in the same fashion as was done in Khaksari and Kirkpatrick[5] by mixing calcium aluminum borosilicate glass microspheres (LUXSIL Cosmetic Microspheres, Potters Industries, Inc., Malvern, PA) with DI water. The microspheres were polydisperse in terms of diameter, ranging between 9-13μm, which is close to the diameter of red blood cells. The microspheres had mass density of 1.1g/cc, which being close to that of water, minimized settling. Using a Mie calculator,[12] the appropriate microsphere concentration was calculated using Mie theory to approximate the scattering coefficient of whole blood at various hematocrit levels.[11] For these calculations, we assumed that the microspheres were pure scatterers and that $\mu_a = 0$. Once the necessary concentrations of microspheres needed to create samples that approximate the scattering properties of whole blood were calculated, the flow phantoms were made by adding the calculated amount of microspheres to DI water. Ten solution phantoms of different scatterer concentrations were made using the results from the Mie calculations. Scattering coefficients of the fluid phantoms were confirmed via ballistic transmission measurements. A modified version of the Lambert-Beer law was used to calculate the scattering coefficient. Equations 3 and 4 summarize the approach:

$$I(z) = I_0[\exp-(\mu_s + \mu_a)z] \quad ; \quad \mu_a = 0 \tag{3}$$

$$\mu_s = \frac{\ln(\frac{I(z)}{I_0})}{z} \tag{4}$$

where μ_s is the scattering coefficient, μ_a is the absorption coefficient and z is the linear path length through the sample. The samples were in contained in cuvettes with 1cm

internal width (z=1cm). I_0 is the intensity of the ballistically transmitted beam when pure

DI water was used as the sample in place of a scattering phantom. Since $I(z)$ of the DI

water and the scattering samples was measured in the same cuvette and the ratio between

the intensities, $\dfrac{I(z)}{I_o}$, the intensity loss due to the cuvette wall was eliminated from the

calculations.

To calculate the reduced scattering coefficient, μ_s', we assumed scattering

anisotropy of, $g = 0.9$ from the Mie calculations and

$$\mu_s' = \mu_s(1-g).\qquad\qquad(5)$$

Because the microsphere powder was polydispese in terms of diameter, ranging between 9

– 13 μm, with a mean size of 11.7μm according to the manufacturer, but with an unknown

size probability distribution, Mie calculations were performed assuming mono-dispersions

of 9.0 μm, 11.7 μm, and 13.0 μm. The scattering coefficients calculated via Mie theory

were compared to the values generated via the ballistic transmission experiments in order

to better characterize the scattering behavior of the fluid phantoms.

The effect of varying μ_a on LSCI was also of interest in this study. Thus, a series

of absorbing liquid phantoms was constructed. An 'added-absorber' approach was

followed in making these phantoms. Empirically determined volumes of India ink were

added to the purely scattering phantoms and pure DI water. Using ballistic transmission

again, and with a priori knowledge of the scattering coefficient of the sample the absorption

coefficient was estimated as:

$$I(z) = I_0[\exp-(\mu_s + \mu_a)z]$$

$$\mu_t = \mu_s + \mu_a \tag{6}$$

Equation (6) calculates the total attenuation coefficient (μ_t). By rearrangement, then,

$$\mu_a = \mu_t - \mu_s \tag{7}$$

Ultimately, an 11x11 matrix of phantom solutions with each element of the matrix having a unique combination of μ_s, μ_a, and therefore μ_t was developed. The initial sample in this matrix was pure DI water ($\mu_s = \mu_a = \mu_t = 0$) and the last sample has the largest concentration of microspheres and India ink $\left(\mu_s = \mu_a = \mu_t = \max \right)$.

2.3 LSCI Measurements

Each fluid phantom was imaged with the LSCI system described above at a uniform velocity. Figure 21 displays the cross section of the sample preparation we used in the LSCI setup. As can be seen in the picture, the moving and static parts are in the same depth of field (flow is coming out of the page, towards the reader).

The camera lens (100mm macro zoom) was fixed at f/32, which resulted in relatively large speckles (see below) and an extended depth of field. During the experiments, all experimental parameters were held constant with the exception of the optical properties of the moving fluid, which varied by sample. The flow velocity was held constant at 5mm/s. The camera integration time was 6ms and held constant for all experiments. Images were acquired at a frame rate of 125 frames/s. Thus, the only varying parameter was the optical properties of the fluid phantom used.

An important parameter in a LSCI experiment is the relative size of the speckles vs. camera pixel size.[13] The minimum speckle size (in pixels), σ_{min}, was determined by

calculating the power spectral density of the raw speckle images (Figs. 22a, 22b) and applying Eq. 8:

$$\sigma_{min} = 2 \left(\frac{\text{Width of Array}}{\text{Diameter of PSD Energy Band}} \right) \qquad (8)$$

In LSCI, unlike other speckle techniques such as diffusing wave spectroscopy, the minimum speckle size should not match the camera pixel size, but must be greater than 2 times of camera pixel pitch in order to meet the spatial Nyquist criteria.[13] In these experiments, the minimum speckle size was set to 2.72 times the pixel size (10.7 μm). The minimum speckle size in the image plane was, therefore $\approx 29.1 \, \mu m$.

For image collection, the laser was set slightly off-axis to avoid specular reflection. A video of 100 frames was recorded with the CCD camera for each sample. The experiment was repeated 3 times for each sample. In the end, 300 frames of raw speckle and 300 contrast images were recorded for each sample. The 300 frames were then averaged to create an 'average' contrast image. The ratio between the dynamic (fluid) region and the static region (K_{ratio}) of the contrast images was calculated for all of the images. Similar to above, an 11x11 matrix was created of K_{ratio} values. This matrix demonstrated the change in contrast that resulted from the change in the optical properties of the fluid phantoms. The numerical values of K_{ratio} lay between 0 and 1.0, since the contrast is always lower in the fluid (dynamic) region of the contrast image:

$$K_{ratio} = {K_{fluid}} \Big/ {K_{static}} \qquad . \qquad (9)$$

3. RESULTS

3.1 Phantom Characterization

The scattering coefficient for 10 different sample concentrations of microspheres (plus pure DI water) was measured and by assuming $g = 0.9$, the reduced scattering coefficient of the samples was estimated. By increasing the number of scatterers, the reduced scattering coefficient increased in a linear fashion. Figure (23) shows the phantom's reduced scattering coefficients and the relationship between the concentration of scatterers and the reduced scattering coefficient. Because the microspheres were polydisperse with an unknown size distribution, Fig. 23 also displays the results of Mie scattering simulations for the minimum, maximum, and means size of the spheres as reported by the manufacturer. It is seen that the polydisperse mixtures displayed overall scattering behavior similar to that of a monodisperse system of ~10.5µm spheres. Microsphere concentration $[c]$ ranged from 9.2e-3mg/ml (1e-5 spheres/µm^3) to 9.2e-2 mg/ml (1e-4 spheres/µm^3) and the reduced scattering coefficient of the samples ranged from 0.48 mm^{-1} to 4.84 mm^{-1}. A linear regression through the experimental data yielded the following relationship:

$$\mu_s^{'} = 48.66[c] - 0.196 \quad (r^2 = 0.977). \tag{10}$$

By adding measured amounts of India ink to the sample with the highest concentration of microspheres ($\mu_s^{'} = 4.8\text{mm}^{-1}$), we determined the absorption coefficient at 10 different India ink concentrations via ballistic transmission measurements of μ_t and using Eq. 7. Absorption coefficient values of the phantoms used in our study ranged from

$5.1e-3 \leq \mu_a \leq 6.73e-2$ mm^{-1}. Figure (24) shows the linear relationship between India ink concentration and the measured absorption coefficient $\left(\mu_a = 367.3[\text{ink}] + 0.0016; \quad r^2 = 0.996\right)$.

3.2 Contrast Imaging

The main goal of this investigation was to examine the combined effects of scattering and absorption on the contrast in LSCI images. As discussed above, the experiments were run for the 121 phantoms with unique combinations of reduced scattering and absorption coefficients. Accordingly, within the matrix, the absorption coefficient changed when moving along the rows and the reduced scattering coefficient changed moving along the columns. Values of K_{ratio} were obtained from this matrix, and the contrast ratios for the different combinations of optical properties were plotted.

Figure (25) shows an example LSCI images from the 11x11 K_{ratio} matrix. The tubing that contained fluid phantom flowed runs from the upper left to lower right and the resulting, low-contrast area is readily observed in the images. The triangular regions in the upper right and lower left were the 'static' plastic block.

The relationship between K_{ratio} and μ_s' was found to be linear. An increase the concentration of scatterers $[c]$ which manifested as an increase in μ_s' resulted in a decrease in K_{ratio}.[5] The results are plotted in Fig. (26) where K_{ratio} is plotted as a function of μ_s' for 11 different values of μ_a. All the linear fits were statistically significant (*t*-test, $p<0.05$) and the slopes, m_s, of the best fit lines ranged between $-0.072\dfrac{\Delta K_{ratio}}{\Delta \mu_s'} \leq m_s \leq -0.05\dfrac{\Delta K_{ratio}}{\Delta \mu_s'}$

and there was no significant difference between the slopes (*t*-test, $p < 0.05$). The mean slope was $-5.53e - 2 \frac{\Delta K_{ratio}}{\Delta \mu_s'}$. Figure (27) plots the y-intercepts $\left(\mu_s' = 0 \right)$ of the regression lines shown in Fig. (26) as a function of absorption coefficient, μ_a. This plot reveals a linear reduction in K_{ratio} with an increase in μ_a in our experiments $\left(K_{ratio|\mu_s'=0} = -5.68 \mu_a + 0.94 ; \; r^2 = -0.982 \right)$.

As will be discussed below, this reduction in contrast is due to the attenuation of the light reaching the static scattering block below the moving fluid and thus, reducing the influence of these static scatterers on the overall contrast. Others[8,9] have observed an increase in contrast with an increase in absorption, however, in their experiments, there was no underlying layer of static scatterers and their scattering mediums were optically semi-infinite, or close to it.

Thus, with an increase in absorption coefficient, K_{ratio} decreased. This trend is shown for the fluid phantoms with 11 different reduced scattering coefficients in Fig. (28). All the linear fits were statistically significant (*t*-test, $p < 0.05$) and the slopes, m_a, of the best fit lines ranged between $-3.52 \frac{\Delta K_{ratio}}{\Delta \mu_a} \leq m_a \leq -4.55 \frac{\Delta K_{ratio}}{\Delta \mu_a}$ and there was no significant difference between the slopes (*t*-test, $p < 0.05$). The mean slope was $-4.01 \frac{\Delta K_{ratio}}{\Delta \mu_a}$. Figure (29) plots the y-intercepts of these regression lines as a function of the corresponding reduced scattering coefficients. This plot reveals a linear reduction in

K_{ratio} with an increase in μ_s' in our experiments

$\left(K_{ratio|\mu_a=0} = (-7.02e-2)\mu_s' + 0.92 ; \ r^2 = -0.976 \right)$.

By combining the scattering and absorption data, the influence of total attenuation coefficient, $\mu_t = \mu_s' + \mu_a$ on K_{ratio} was assessed. As expected from the results presented above, there was a linear decrease in K_{ratio} with an increase in μ_t. Figure (30) displays the results of the K_{ratio} vs μ_t for the samples that were along the major axis of the scattering – absorption phantom matrix. The equation describing the least-square fit was $K_{ratio} = -0.14\mu_t + 0.93; \ r^2 = -0.94$. The slope is statistically significant (t-test, $p < 0.05$).

4. Conclusions

We have demonstrated a linear decrease in speckle contrast, K_{ratio} , with an increase in reduced scattering coefficient. This decrease in contrast with an increase in μ_s' was independent of absorption as quantified by the absorption coefficient, μ_a . It is important to note that the parameter of real interest is not the scattering coefficient, per se, but the concentration of scatterers, $[c]$, in the imaging volume. A change in $[c]$ manifests as a linear change in μ_s' .[5]

Likewise, in this study, contrast decreased linearly as absorption increased. Others[8,9] have reported an increase in contrast as absorption increases. At initial glance, it may appear that these results are contradictory. However, that is not the case and indeed, the results presented here are entirely consistent with what has been reported in the

literature previously. The effect of increasing absorption is to decrease the number of (deep) scattering events. In previous publications, the fluid phantoms were relatively deep and the entire imaging volume was populated by dynamic scatterers. Thus, by adding absorber, the number of dynamic scattering events was reduced, resulting in an increase in contrast. In the present situation, the addition of absorbers accomplished the same thing. That is a decrease in the number of deep scattering events. However, in our case, the deep scatterers were static, coming from the fixed plastic block underneath the glass tube that served as our imaging window. Thus, the absorbers decreased the number of static scattering events and thereby the influence of these static scattering events was reduced, resulting in decreased contrast values.

Recently, Kazmi et al.[8] focusing entirely on scattering concluded that LSCI is sensitive to the product of speed and a dimensional term that is proportional to vessel diameter. In the Introduction to this paper, and in our prior work,[5] it was argued that LSCI is sensitive to advective flux. These two conclusions are, again, entirely consistent with each other. Recall from above that advective flux, J_G is the second term on the RHS of the diffusion with drift equation. Rewriting Eq. (2),[5]

$$J_{KK} = -D\frac{\partial[c]}{\partial x} + \vec{v}_x[c],$$

and

$$J_G = \vec{v}_x[c]. \tag{12}$$

Thus, Khaksari and Kirkpatrick[5] concluded that LSCI is sensitive to the product of velocity (assuming direction is known) and scatterer concentration. Note that advective flux as

defined by Eq. (12) is related to the total mass flux $\dot{m}$ across a plane perpendicular to the direction of flow via Eq. (13):

$$\dot{m} = J_{KK}S ,$$ (13)

where S is the internal cross-sectional area of the tube or vessel containing the flow, J_{KK} is the total flux, and the dot over the variable explicitly indicates the time derivative. It assumed that diffusional flux = 0 and $J_G = J_{KK}$. To be consistent with the conclusions of Kazmi et al.,[8] Eq. 13 can be re-written in terms of diameter:

$$\dot{m} = J_{KK}\left(\frac{\pi}{4}\right)d^2 ,$$ (14)

where d is the diameter of the vessel. By substitution, then

$$\dot{m} = \vec{v}_x [c]\left(\frac{\pi}{4}\right)d^2 .$$ (15)

Thus total mass flux is given by Eq. (15), assuming that diffusional flux = 0. In the case where diffusional flux does not equal 0.0 (likely in most practical LSCI applications), then the total mass flux is given by

$$\dot{m}_T = \left(-D\frac{\delta[c]}{\delta x} + \vec{v}_x [c]\right)\left(\frac{\pi}{4}\right)d^2 .$$ (16)

Equations (15) and (16), then, shows the consistency between the present results, the results of Khaksari and Kirkpatrick[5] and the results of Kazmi et al.[8] That is, in terms of mass flux, LSCI is sensitive to the product of velocity (or speed if direction is not known explicitly), particle concentration, and a factor that is proportional to diameter squared.

The present paper is certainly not the first paper to demonstrate that speckle contrast changes as a function of the amount of scattering or absorption present,[5,8,9] however, this

is the first systematic study that systematically evaluated the combined effects of scattering and absorption on contrast values. Furthermore, the present paper demonstrates that by viewing LSCI in terms of mass transport, consistency between earlier studies and the present one can be achieved. Specifically, we demonstrate that both scattering and absorption have linear effects on contrast values. Contrast values decrease linearly with an increase in scattering, regardless of absorption. An increase in absorption serves to reduce the number of deep scattering events observed. Thus, depending if the 'deep' scatterers are dynamic or static, contrast values can either increase or decrease with increased absorption.

5. References

1. A. F. Fercher and J.D. Briers, "Flow visualization by means of single-exposure speckle photography," *Opt. Commun.* **37**(5), 326-330 (1981).

2. D. A. Boas and A. K. Dunn, "Laser speckle contrast imaging in biomedicine," *J. Biomed. Opt.* **15**(1), 011109 (2010).

3. D. Briers et al., "Laser speckle contrast imaging: Theoretical and practical limitations," *J. Biomed. Opt.* **18**(6) 066018 (2013).

4. D. D. Duncan, S. J. Kirkpatrick, and R.K. Wang, "Statistics of local speckle contrast," *J Opt. Soc. Am. A* **25**(1), 9-15 (2008).

5. K. Khaksari and S. J. Kirkpatrick, "Laser speckle contrast imaging is sensitive to advective flux," *J. Biomed. Opt.* in review (2016).

6. Berg, H.C., *Random Walks in Biology*, Princeton University Press, Princeton, NJ, USA, 1983.

7. D. D. Duncan and S. J. Kirkpatrick, "Can laser speckle flowmetry be made a quantitative tool?," *J. Opt. Soc. Am* **25**(8), 2088-2094 (2008).

8. S. M. Kazmi, et al., "Flux or speed? Examining speckle contrast imaging of vascular flows," *Biomed Opt. Express* **6**(7), 2588-2608 (2015).

9. A, Mazhar, et al., "Laser speckle imaging in the frequency domain," *Biomed Opt. Express* **2**(6), 1553-1563 (2011).

10. J. F. Murray, "Systemic circulation," *Annual Rev. Physiol*, **26**, 389-420 (1964).

11. D. J. Pine et al., "Diffusing-wave spectroscopy: dynamic light scattering in the multiple scattering limit," *J. Phys.* **51**(27), 2101-2127 (1990).

12. http://omlc.org/calc/mie_calc.html

13. S. J. Kirkpatrick, D. D. Duncan, and E. M. Wells-Gray. "Detrimental effects of speckle-pixel size matching in laser speckle contrast imaging." *Optics letters* **33**(24), 2886-2888 (2008).

Figures:
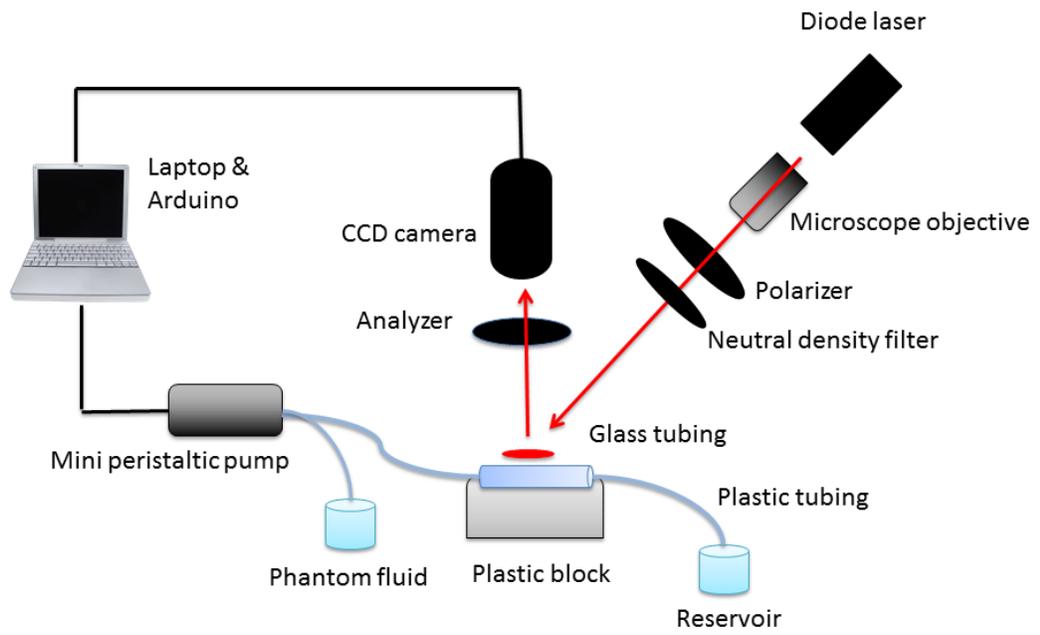
Figure 20. Diagram of the LSCI and flow systems.
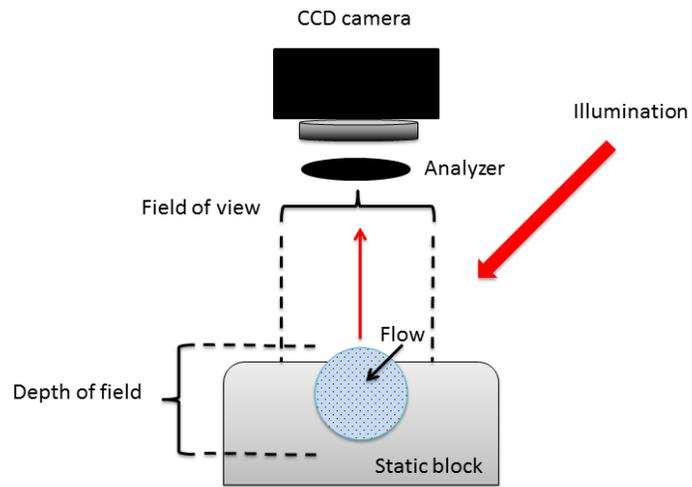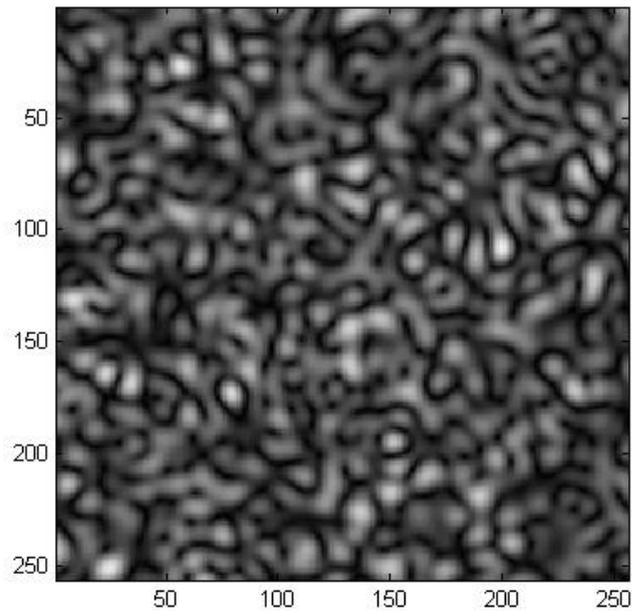
Figure 21. Sample cross-section.

Figure 22a. A laser speckle pattern.
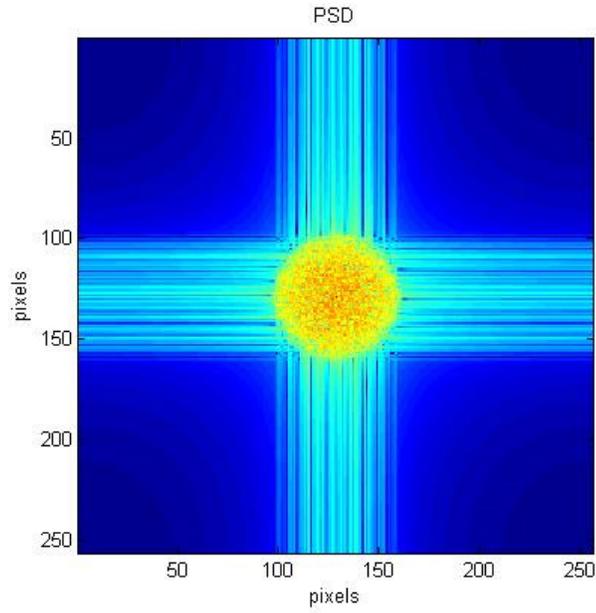
Figure 22b. Power spectral density of the speckle pattern shown in Fig. (21a). The diameter of the bright central region is inversely proportional to the minimum speckle size in the speckle pattern.

Figure 23. Mie calculations predicting the reduced scattering coefficient for glass

spherical particles of 9.0 μm, 10.5 μm, 11.7 μm, and 13.0 μm diameters (dashed lines,

red dashed lines on-line). Reduced scattering coefficient as determined by ballistic

transmission data points is shown for the fluid phantoms (dots) along with the best-fit line

in a least squares sense. The polydisperse microsphere phantoms behaved approximately

as a monodisperse system made of 10.5 μm glass microspheres.

$$\left(\mu_s^{'} = 48.66[c] - 0.196; \quad r^2 = 0.98 \right).$$

Figure 24. Plot of the absorption coefficient of the fluid phantoms as a function of India

ink concentration. $\left(\mu_a = 367.3[\text{ink}] + .0016; \quad r^2 = 0.996 \right).$

Figure 25. A representative LSCI image. The fluid motion was in the low contrast region flowing from upper left to lower right of the image. The surrounding higher contrast triangular areas are the static plastic block.

Figure 26. Plot of K_{ratio} vs. μ_s' at 10 different values of μ_a . All slopes were statistically significant (t-test, p <0.05) and there was no statistically significant difference between the slopes (t-test, p <0.05). The mean slope was $-5.53e-2\dfrac{\Delta K_{ratio}}{\Delta\mu_s'}$.


Figure 27. Plot of the y-intercepts $\left(\mu_s'=0\right)$ of Fig. (7) as a function of respective absorption coefficients. An increase in absorption resulted in a linear decrease in K_{ratio} in these experiments due to reducing the influence of the underlying static scatterers.

$$\left(K_{ratio|\mu_s'=0}=-5.68\mu_a+0.94\,;\ r^2=-0.982\right).$$

Figure 28. Plot of K_{ratio} vs. μ_a at 10 different values of μ_s'. All slopes were statistically significant (t-test, p <0.05) and there was no statistically significant difference between the slopes (t-test, p <0.05). The mean slope $-4.01 \dfrac{\Delta K_{ratio}}{\Delta \mu_a}$.


Figure 29. Plot of the *y*-intercepts $\left(\mu_a = 0\right)$ of Fig. (7) as a function of respective reduced scattering coefficients. An increase in scattering resulted in a linear decrease in K_{ratio}. $\left(K_{ratio|\mu_a=0} = (-7.02e-2)\mu_s' + 0.92 \, ; \; r^2 = -0.976\right)$.

Figure 30. Plot of K_{ratio} vs. μ_t for the phantom samples that were along the major axis of the scattering and absorption phantom matrix. An increase in μ_t resulted in a significant decrease in K_{ratio}. $\left(K_{ratio} = -0.14\mu_t + 0.93;\ r^2 = -0.94 \right)$.

Chapter 5

(Paper 2)

Laser Speckle Contrast Imaging is Sensitive to Advective Flux Density[1]

Contribution of Authors:

Sean J. Kirkpatrick: Principal Investigator, data evaluation, writing and edition

Kosar Khaksari: Ran the experiments; Developed theory, Wrote computer code, Analyzed data, Wrote manuscript

Kosar Khaksari and *Sean J. Kirkpatrick*[*]

*Corresponding Author: E-mail: sjkirkpa@mtu.edu

Michigan Technological University, Department of Biomedical Engineering, 1400 Townsend Dr., Houghton, MI, 49931 USA

Abstract. Unlike laser Doppler flowmetry, there has yet to be presented a clear description of the physical variables that laser speckle contrast imaging (LSCI) is sensitive to. Herein, we present a theoretical basis for demonstrating that LSCI is sensitive to total flux, and in particular the summation of diffusive flux and advective flux density. We view LSCI from the perspective of mass transport and briefly derive the diffusion with drift equation in terms of an LSCI experiment. This equation reveals the relative sensitivity of LSCI to both diffusive flux and advective flux, and thereby to both concentration and the ordered velocity of the scattering particles. We demonstrate this dependence through a short series of flow experiments that yield relationships between the calculated speckle contrast and the concentration of the scatterers (manifesting as changes in scattering coefficient), between speckle contrast and the velocity of the scattering fluid, and ultimately between speckle contrast and advective flux. Finally, we argue that the diffusion with drift equation can be used to support both Lorentzian and Gaussian correlation models that relate observed contrast to the movement of the scattering particles and that a weighted linear combination of these two models is likely the most appropriate model for relating speckle contrast to particle motion.

1. Introduction

Laser speckle contrast imaging (LSCI) is a non-invasive (or minimally invasive) imaging modality used primarily for the relative and qualitative imaging of blood flow and perfusion.[1-3] This method has a wide field of view and it is efficient and simple for full-field monitoring. The simplicity of LSCI along with its high spatial and temporal resolution allows it to be used as a powerful tool to measure, monitor and investigate living processes in near real-time. The fundamental concept behind this method is the quantification of the relationship between moving particles (scatterers) in the object space (i.e, the living organ or blood vessel) and the moving speckles in the image plane. When there is motion in the object space, the intensity of speckles in the image space fluctuates in time. It is these time-varying speckles in the image space that encode the motion in the scattering object. In time varying, or dynamic, speckle patterns the speckle is blurred during the finite camera integration time and the spatial variation, or contrast, in intensity is thereby decreased.

A clear relationship between LSCI and laser Doppler flowmetry has been established in the literature.[4] Furthermore, a clear relationship between laser Doppler flowmetry and both the concentration of scattering particles and the velocity of the particle-containing fluid has been established.[4] As noted by Boas and Dunn,[2] the theoretical basis of LSCI seems to imply that LSCI is sensitive to variations in speed, yet several authors have observed that LSCI is sensitive to particle concentration as well.[2,5] This implies that LSCI is truly a measure of flux. However, a clear demonstration of this has yet to be presented. That is the purpose of this manuscript.

Blood perfusion, flow, speed, velocity and flux

In order to more clearly understand exactly what LSCI is sensitive to, it is important to have clear definitions of the various terms used in the literature to describe the movement of blood. Many of these terms have been used interchangeably in the LSCI literature, even though these terms possess different units and physical dimensions.[2,3]

Clinical units for blood perfusion are typically milliliters (of blood) per milliliters (of tissue) per second (ml/ml/s) and is a measure of blood volume flow through a given volume or mass of tissue. Blood perfusion clearly indicates a rate, $\phi_b = \dfrac{(V_b / V_t)}{s}$, where V_b is the volume of whole blood, V_t is the volume of tissue, and *s* is seconds. Alternatively, blood perfusion may be reported in units of ml/100mg/min. Either way, clinical blood perfusion is a measure of capillary and interstitial blood flow and is meant as a means of quantifying the delivery of oxygen and nutrients to the tissue as well as the removal rate of metabolic waste from the tissue by the blood. Regardless of units, blood perfusion has physical dimensions of [quantity] T^{-1} (because $M \propto L^3$). It should be noted that V_b refers to the volume of whole blood, not just the components of blood that scatter light. The units of blood perfusion imply a concentration rate.

The term flow is usually expressed in terms of volume per time, for example, ml/s, and has physical dimensions of L^3 / T. The frequency shift observed in laser Doppler flowmetry of blood has been convincingly demonstrated to be sensitive to bulk blood flow and to particle density.[4] Flow, when discussing the movement of a fluid with suspended particles, such as blood, is often thought of as the number of particles per volume per time,[2] or a concentration rate, $[\dot{c}]$, where the dot explicitly indicates the time derivative and $[c]$ is

103

the number concentration, $[c] = \dfrac{n_p}{V_b}$, where n_p is the number of particles. In this case, flow

is more properly referred to as flux density (below).

Speed and velocity are often used interchangeably, although they are two very different quantities.[3] Speed is a scalar quantity with units of distance per time (*e.g.,* ms^{-1}), while velocity is a vector quantity with the same units. The magnitude of the velocity vector is speed. Both speed and velocity have physical dimensions of LT^{-1}.

Flux is a term used to describe transport phenomena. That is the flow of some physical property (mass, energy, momentum, etc.) in space. It is typically thought of as a rate of flow of a physical property per unit area. Flux has the physical dimensions of [quantity] $T^{-1}L^{-2}$. Of particular relevance to LSCI is the diffusive flux (the rate of movement of particles across a unit area (e.g., mol m^{-2}·s^{-1}) which describes Fick's first law of diffusion and advective flux ([particles] m^{-2} s^{-1}) where the square brackets indicate the number concentration.[6]

Relationship to laser Doppler flowmetry

In addressing the issue of what LSCI is sensitive to, the usual approach is to observe that LSCI and laser Doppler flowmetry (LDF) essentially measure the same quantity, although through very different means.[3] Goodman[7] established a relationship between the speckle contrast, $K = \dfrac{\sigma_s}{\langle I \rangle}$, and the autocovariance of the intensity fluctuations, $C_t(\tau)$, of an individual speckle:[3]

$$K^2 \propto \sigma_s^2(T) = \frac{1}{T}\int_0^T C_t(\tau)\,d\tau, \tag{1}$$

where T is the detector integration time, τ is the characteristic correlation time, and σ^2 is the speckle intensity variance over time T.   The autocovariance of the intensity fluctuations, $C_t(\tau)$ was assumed to follow a Lorentzian distribution, although this assumption is not a necessity for Eq. (1) to hold. By assuming a Lorentzian line shape for $C_t(\tau)$, it is implicit that the underlying particle motions giving rise to the intensity fluctuations is random (Brownian for larger particles). If ordered motion is assumed, then $C_t(\tau)$ follows a Gaussian line shape.[8] Laser Doppler flowmetry directly evaluates the integrand on the right hand side of Eq. (1), while LSCI indirectly assesses the left hand side of the equation.[3]

Bonner and Nossal[4] clearly demonstrated a quantitative relationship between the mean Doppler shift, $\langle \omega \rangle$, particle density and velocity of the fluid in a moving fluid. That is, a dependence of $\langle \omega \rangle$ on particle flux. Yet, such a clear demonstration has not yet been provided for LSCI. The remainder of this manuscript considers LSCI from the perspective of mass transport and aims to demonstrate a theoretical and experimental dependence of LSCI on particle flux.

2. Theory

Diffusion with Drift Equations

We begin by viewing the problem in terms of a 3-dimensional mass-transport problem governed by the convection-diffusion equations.[6] In the most general 3-D form, the convection-diffusion equation is frequently given as

$$\frac{\partial [c]}{\partial t} = R + \nabla \cdot (D\nabla[c]) - \nabla \cdot (\vec{v}[c]) \tag{2}$$

where $[c]$ is the concentration of scatterers (*e.g.,* red blood cells), D is the mass diffusivity for the scattering particle motion and is simply diffusion coefficient of the scatterers, R is a factor that accounts for a change in the number of scatterers due to creation or destruction (also referred to as a "source" or "sink" of $[c]$), and $\vec{v}$ is the average velocity of the moving scatterers which in our case we will assume is the average blood flow velocity (ms^{-1}). As usual, $\nabla \cdot$ represents the divergence and ∇ is the gradient in the dimensions [x,y,z].

Several simplifying assumptions can be made for our situation.[6] We assume a steady-state situation such that $\frac{\partial [c]}{\partial t} = 0$. That is, the concentration of scatterers remains constant over the imaging time. Secondly, we assume that the overall number of scatterers remains constant in our imaging volume over the imaging time. That is $R = 0$. Given these assumptions, then, Eq. (2) becomes the stationary convection-diffusion equation

$$0 = \nabla \cdot (D\nabla[c]) - \nabla \cdot (\vec{v}[c]) \tag{3}$$

The first term on the right hand side (RHS) of the equation, $\nabla \cdot (D\nabla[c])$ describes the flux J_L due to random motion of the scatterers and in mass-transport theory is usually attributed to diffusion. The local motion of the scatterers is random and in spectroscopic or laser physics terminology is described by a Lorentzian spectral line shape.[8] Employing an analogy from laser physics, all of the scatterers in the imaging volume will have identical behaviors. In laser physics, this results in the phenomenon of homogeneous line broadening and is one of the two possible limiting behaviors of moving particles. The second term on the RHS of the equation $\nabla \cdot (\vec{v}[c])$ describes the flux J_G due to both the concentration of

the scatterers and the velocity of the fluid (blood serum). This term is referred to as *advective flux density*. Advection is defined here as the transport mechanism by which the scatterers (*e.g.*, red blood cells) are transported due to the bulk motion of the fluid, the blood serum. The advection operator in Cartesian coordinates can be given by[6]

$$\nabla \cdot \mathbf{v} = \vec{v}_x \frac{\partial}{\partial x} + \vec{v}_y \frac{\partial}{\partial y} + \vec{v}_z \frac{\partial}{\partial z} \quad , \tag{4}$$

where **v** is a velocity field. If the flow is assumed to be incompressible then **v** is solenoidal (*i.e.*, $\nabla \cdot \mathbf{v} = 0$) and the advection equation may be written as

$$\frac{\partial \varphi}{\partial t} + \mathbf{v} \cdot \nabla \varphi = 0 \tag{5}$$

where φ is a scalar field that describes the location of the scattering particles. If the flow of the blood serum is steady then $\mathbf{v} \cdot \nabla \varphi = 0$, φ is steady along a streamline and the flow is organized. As above, in the terminology of laser physics, this can be viewed as an inhomogeneous line broadening phenomenon and the dynamic behavior is particular to individual scatterers. The line shape for the population of scatterers in this case is Gaussian[8] and represents the other possible limiting behavior (as opposed to the Lorentzian description, above).

Thus, Eq. (3) describes ordered and unordered flow, along with both the diffusion dependent and velocity dependent components of the total flux $J_{KK} = J_L + J_G$. In the case where the motion is entirely due to random motion (Brownian), then $J_G = 0$. In the other limiting case where the motion is purely organized flow, $J_L = 0$. Of course, these two limiting situation are rare, and in most cases of practical interests, there will be components of both types of motion.

For the sake of thoroughness, it is worth noting that the average velocity $\vec{v}$ is in some fashion proportional to the applied pressure (*i.e.,* the blood pressure). In this case, we can write the stationary drift-diffusion equation:[6]

$$0 = \nabla \cdot (D\nabla[c]) - \nabla \cdot \left(\frac{\vec{F}c}{\xi}\right) \quad , \tag{6}$$

where $\vec{F}$ is the applied force and ξ describes the viscous drag on the particles (e.g., the red blood cells).

In the case of perfusion imaging using LSCI, the dimensionality of the problem can be reduced to 2 dimensions, x and y (assuming the optical imaging axis is in the z direction). The situation becomes planar when one realizes that LSCI is a coherent imaging technique and that the light scattered from all scatterers within the depth of field (DOF) of the imaging lens will coherently sum in the imaging plane to create a single speckle pattern. The underlying assumption is that the temporal coherence length of the laser, $\ell_c \geq \text{DOF}$. In the planar assumption, the convection-diffusion equation (Eq. (3)), then, is recognized as Fick's first equation with drift:[9]

$$
\begin{aligned}
J_x &= -D\frac{\partial[c]}{\partial x} + \vec{v}_x[c] \\
J_y &= -D\frac{\partial[c]}{\partial y} + \vec{v}_y[c].
\end{aligned}
\tag{7}
$$

Equation (7) describes the situation in which all of the scatterers translate in the $+x$ (or $+y$) direction at a velocity $\vec{v}$. Thus the flux at any point x increases by amount $\vec{v}_x[c](x)$ (and similarly for any point y).

Equation (7) may also be written in a form that incorporates the applied force $\vec{F}$, such as blood pressure, that is responsible for the 'drift' (*i.e.,* the second term on the RHS of Eq. (7)). In this case, Eq. (7) becomes

$$J_x = -D\frac{\partial[c]}{\partial x} + \frac{\vec{F}_x}{\xi}[c]$$

$$J_y = -D\frac{\partial[c]}{\partial y} + \frac{\vec{F}_y}{\xi}[c].$$

(8)

In many LSCI applications where the motion along a vessel is of interest, Eq. (7) can be further reduced in dimensionality to a 1-D problem. As with the discussion of Eq. (3), Eq. (7) describes ordered and unordered flow, along with both the diffusion dependent (first term on the RHS) and velocity dependent (2nd term on the RHS) components of the total flux.

We now focus on a situation in which the movement of scattering particles is entirely random (Brownian motion). Such a situation may be envisioned when using LSCI to image a semi-infinite medium with scattering particles (*e.g.,* microspheres) in random motion. Thus,

$$J_{KK} \propto \frac{\partial[c]}{\partial x}.$$

(9)

Therefore, in this implementation, LSCI is sensitive to diffusional flux resulting from a concentration gradient or from the Brownian motion of particles.

In the case of primarily ordered flow (*i.e.,* steady flow in a vessel or tube) it is seen that

$$J_{KK} \cong \vec{v}[c] \quad .$$

(10)

Equation (10) describes the condition in which the total flux is due entirely to advective flux density. Advective flux density is flux that is dependent upon both velocity $\vec{v}$ and concentration of scattering particles $[c]$.[6] Thus in this implementation, LSCI is sensitive to flux resulting from both velocity and concentration of scatterers. An increase in either velocity or concentration will result in an increase in the number of dynamic scattering events during a given time interval (camera integration time, T), resulting in a decrease in contrast, K.

To relate this discussion to our assertion at the top of this section that our problem is one of mass transport, we note that advective flux density as defined by Eq. (10) is related to the total mass flux $\dot{m}$ across a plane perpendicular to the direction of flow via Eq. (11):

$$\dot{m} = J_{KK} S \,, \tag{11}$$

where S is the internal cross-sectional area of the tube or vessel containing the flow and the dot over the variable explicitly indicates the time derivative.

Relationship of the Diffusion with Drift Equation to Contrast: Random motion and the Lorentzian cumulative distribution function

Consider the one-dimensional case:[9]

$$J_{KK} = -D \frac{\partial [c]}{\partial x} + \vec{v}_x [c] \,. \tag{12}$$

From Eq. (12), it is seen that the total flux, J_{KK}, is dependent upon the concentration (gradient) of scatterers, $[c]$, and the velocity, $\vec{v}$, of the surrounding fluid that is causing a

lateral translation of the scatterers. Note that changes in $[c]$ manifest as changes in the

scattering coefficient, μ_s, of the fluid solution under observation.

The first term on the RHS of Eq. (12) is recognized as Fick's first law of diffusion.[9]
Particle motion described by this term is random (Brownian). Fercher and Briers[1] invoked
this assumption about the particle motion in their initial description LSCI. Under this
assumption, then, a relationship between speckle contrast, K, (in the imaging plane) and
the exponential (de)correlation function associated with Brownian motion has been
developed by several authors[2,3] and serves as one possible limiting behavior:[8]

$$K(\overline{r}) = \left\{ \frac{\tau_c}{2T} \left[2 - \frac{\tau_c}{T} \left(1 - e^{-2T/\tau_c} \right) \right] \right\}^{\frac{1}{2}}, \tag{13}$$

where τ_c is the characteristic decorrelation time of the observed speckle pattern in the
imaging plane and T is the camera integration time. It is important to note that Eq. (13) is
actually the cumulative distribution function of a Lorentzian probability distribution
function.[8]

Ordered flow and the Gaussian cumulative distribution function

Equation (13) is technically only correct for purely random particle motion
described by the first term on the RHS of Eq. (13). This term, $-D\frac{\partial[c]}{\partial x}$, describes the
diffusional flux, J_L, component of J_{KK}. In this motion, the individual behaviors of the
particles are representative of the population as a whole.

The second term on the RHS of Eq. (13) describes the advective flux density, J_G, component of J_{KK}. This term, $\vec{v}[c]$, describes ordered motion of the particles and the dynamic behavior of the individual particles is unique to the individual scatterers. That is, the behavior of individual particles is not representative of the behavior of the population. This behavior forms the other possible limiting behavior of dynamic particles. As above, several authors have presented a relationship between the observed speckle contrast and the Gaussian correlation function associated with ordered motion:[2,3]

$$K\left(\overline{r}\right) = \left\{ \frac{\tau_c}{2T}\left[\sqrt{2\pi}\operatorname{erf}\left(\frac{\sqrt{2}T}{\tau_c}\right) - \frac{\tau_c}{T}\left(1 - e^{-2(T/\tau_c)^2}\right)\right]\right\}^{\frac{1}{2}} . \tag{14}$$

Again, it is worth noting that Eq. (14) is in actuality a cumulative distribution function of a Gaussian probability distribution function. Also worth noting is that Eq. (14) is technically only accurate for purely ordered flow.[8]

Combination of ordered and un-ordered flow

It is becoming clear, then, that LSCI is sensitive to flux, *J*. The previous two sections have discussed the two contributions to J_{KK}, diffusional flux, J_L, and advective flux density, J_G. In most practical situations involving LSC imaging, it is most likely that both forms of motion are present in some proportion and the actual behavior is a mixture of these two statistically independent processes. In this case, the model relating *K* to the characteristic correlation behavior of the scatterers would be a convolution of the two previous models. Note that by the convolution theorem,[8] the net correlation function for the combined behavior is simply the product of the exponential correlation behavior

112

associated with random motion and the Gaussian correlation behavior associated with ordered motion. Such a model is referred to as a Voigt model.[8] This model has been discussed by Duncan and Kirkpatrick[8] and has been shown to have physical relevance with regards to relating speckle correlation times to scatterer velocity in the object plane.

Thus, depending upon the implementation of LSCI, LSCI is sensitive to diffusional flux (Eq. (9)), advective flux density (eq. (10)), or some combination of the two (Eq. (12). In most practical scenarios of interest LSCI depends upon both velocity and concentration.

3. MATERIALS AND METHODS

A small flow system, an LSCI system, and a series of fluid phantoms with known optical properties were developed so as to examine the effects of velocity, $\bar{v}$, and scatterer concentration, $[c]$. Because the direction of the flow was known *a priori*, velocity, not speed was evaluated. A polarized 660nm diode laser (B&W Tek, Newark, DE, USA) illuminated a piece of glass tubing with outer diameter of 2mm and inner diameter of 1.5 mm on top of a grooved plastic base. The illuminated region was approximately 20 mm in length. The glass tube, which served as our imaging window, rested in the groove. Thus, there was a layer of static scatterers below the flow tube and along both sides. The static scattering regions adjacent to the flow tube served as reference regions to normalize the contrast values from the flow region (see below). A section of rubber tubing was attached to the glass tubing that connected the tubing system to a mini peristaltic pump (Instech Laboratories, Plymouth Meeting, PA, USA, model P625). The fluid phantom material flowed into the tubing using this mini peristaltic pump, which was controlled by an Arduino

microcontroller. A MATLAB GUI controlled the CCD camera (Point Grey, Dragonfly, Vancouver, BC, Canada) and the pump, and also calculated and saved contrast images in near real-time (Fig. 31).
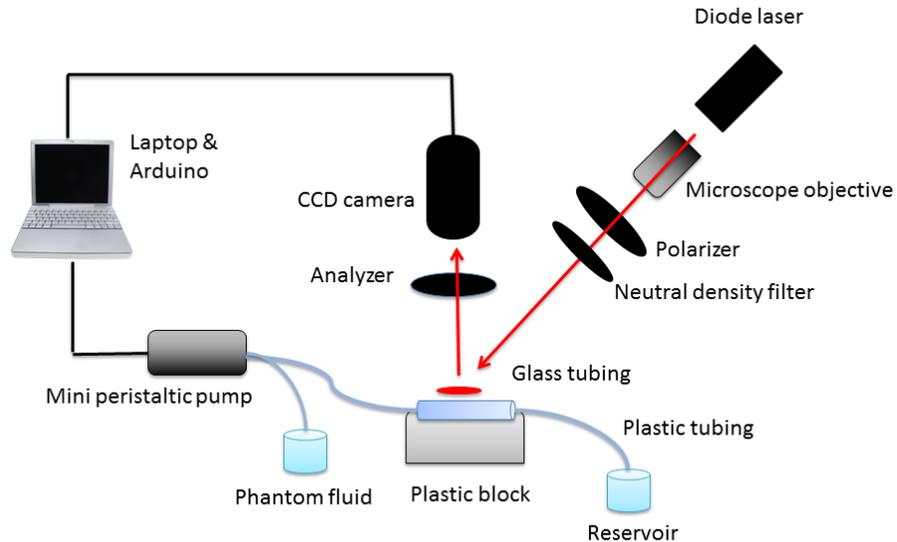

Figure 31. Diagram of the LSCI and flow systems.

Scattering flow phantoms were made by mixing aluminum borosilicate glass microspheres (Luxil Cosmetic Microspheres, Potters Industries, Inc., Malvern, PA) with DI water. The microspheres were poly-disperse in terms of size and the diameters nominally ranged between 9-13 microns with a mean diameter of 11.7 microns according to the manufacturer. The number distribution of the sizes was not known to us. The microspheres had a mass density of 1.1g/cc. Using Mie theory, we calculated the appropriate concentrations to create scattering solutions with reduced scattering

coefficients, μ_s', that approximated that of whole blood with various hematocrit levels.[10]
Once the solutions were mixed, ballistic transmission measurements were used to verify
the scattering coefficient, μ_s and ultimately, μ_s'.

A modified version of the Lambert-Beer law was used to calculate the scattering
coefficient from the ballistic transmission data. Since only scatterers were added to the DI
water, we assumed that the scattering coefficient was much greater than the absorption
coefficient, μ_a, and that $\mu_a = 0$. Thus:

$$I(z) = I_0[\exp{-(\mu_s + \mu_a)z}] \quad ; \quad \mu_a = 0 \tag{15}$$

$$\mu_s = \frac{\ln(\frac{I(z)}{I_0})}{z} \tag{16}$$

where z is the thickness of the samples (1.0 cm), I_0 was the measured intensity of the
ballistically transmitted beam when pure DI water was used as the sample. Since the
ballistic intensity of the DI water and the scattering samples was measured in the same
cuvette and the ratio between the intensities, $\dfrac{I(z)}{I_o}$, the intensity loss due to the cuvette wall
was eliminated from the calculations.

Assuming scattering anisotropy $g = 0.9$ based on the Mie calculations, μ_s' was
calculated for the phantoms as

$$\mu_s' = \mu_s(1-g). \tag{17}$$

In this fashion, 10 liquid phantom samples were made. The number concentration, $[c]$, of
microspheres ranged from $1e^{-5}$ to $1e^{-4}$ microspheres/μm^3 and the reduced scattering

coefficients of the samples ranged from 0.48 to 4.84 mm^{-1}. Pure DI water was also used as a flow sample.

Each fluid phantom was run through the LSCI system described above. The image below (Fig. 32) shows the cross section of the sample preparation we used in the LSCI setup. As can be seen in the picture, both moving and static scatterers were in the within the depth of field of the imaging lens and thus the light scattering from these different regions summed coherently into a single speckle pattern. In this figure, the flow is coming out of the page, towards the reader.
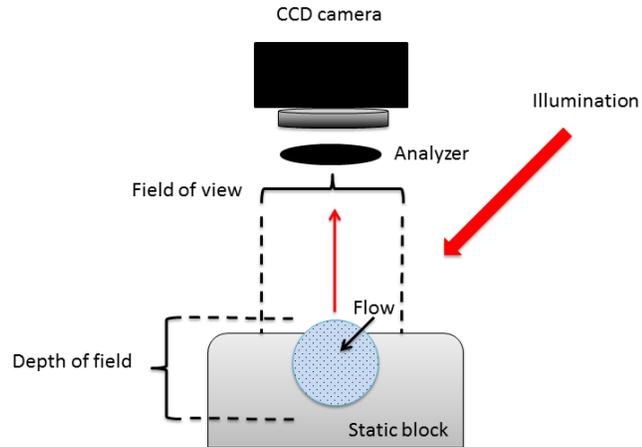
Figure 32. Sample cross-section

The laser was set slightly off-axis to avoid specular reflection. A video of 100 frames was recorded with a CCD camera for each sample at 125 frames per second. The custom MATLAB GUI saved all 100 frames of the raw speckle patterns, generated contrast images using a sliding 7x7 pixel window,[11] and finally saved the resulting contrast images.

The experiment was repeated 3 times for each sample. In order to more generalize the results, we reported a value of $K_{ratio} = \dfrac{K_{flow}}{K_{static}}$, where K_{flow} is the contrast calculated from the 7 x 7 pixel window cropped from the flow region of the speckle images and K_{static} is an identically sized window from the surrounding static region. Reporting K_{ratio} as opposed to just reporting values of K reduced the undesirable influences of ambient light and fluctuations in incident laser intensity on the sample, as well as reduces the influence of the scattering properties of the background static block on the results.

During the experiments to examine the sensitivity of LSCI to changes in $[c]$, all of the experimental variables were held constant with the exception of μ_s', which varied by sample. The velocity, $\bar{v} = 5.0$ mm/s, the outer diameter of the glasstubing was 3mm and the inner diameter was 2mm. The camera integration time, T, was 6ms. The camera lens (55 mm telecentric lens) was fixed at f/32, which resulted in relatively large speckles and an extended depth of field. The minimum speckle size on the CCD chip in the camera was ~ 3x the pixel pitch as determined by examining the power spectrum of a speckle image. K_{ratio} values were calculated as above and plotted as a function of particle concentration.

Similarly, to examine changes in $\bar{v}$, fluid phantoms with a single $[c]$ were flowed through our fluids system at varying velocities ranging from 1 mm s^{-1} to 8 mm s^{-1}. The particle concentration of these samples was constant at 6e-5 spheres/micron^3, which resulted in a reduced scattering coefficient of 2.2 mm^{-1}. All other experimental variables were held constant at the same values as above. K_{ratio} values were calculated and plotted as a function of velocity.

Thus our experiments individually assessed the sensitivity to both $[c]$ and $\vec{v}$. That is, to both components of advective flux.

4. Results

The experiments described above were designed specifically to assess the sensitivity to the $\vec{v}[c]$ term of Eq.(12) and the results clearly show a dependence of K_{ratio} on this term, that is, on advective flux, $\vec{v}[c]$. Both individual changes in $\vec{v}$ and $[c]$ result in changes in K_{ratio}. Figures 33a and 33b display the results of the experiments aimed at assessing the sensitivity of LSCI to scattering particle concentration, $[c]$. Figure (33a) presents the results in terms of changes in $\mu_s^{'}$, while Fig. (33b) presents the results directly in terms of particle concentration. The velocity of the fluid in these experiments was 5.0 mms^{-1}. The solid lines represent the best-fit line in a least-squares sense. The linear equations for these lines are, respectively,

$$K_{ratio} = -0.072\mu_s^{'} + 0.0965$$

$$(18)$$

$$K_{ratio} = -3.3e-3[c] + 0.982.$$

Correlation coefficients for the relationships were $r^2 = 0.95$ and $r^2 = 0.97$, respectively. Thus there is a strong, linear negative relationship between the concentration of scatterers and speckle contrast. Of note in both plots are the points where $[c] = 0$. That is, when contrast measurements were made using pure DI water. The K_{ratio} values in these cases were 0.9985, 0.9986, and 0.9984. These values indicate that the glass tubing used in our

experimental flow system had negligible influence on the contrast values. That is, the contrast in the glass tube was the same as the contrast in the surrounding static medium when no dynamic scatterers were present. Thus, no correction for background scatter from the tube was necessary.
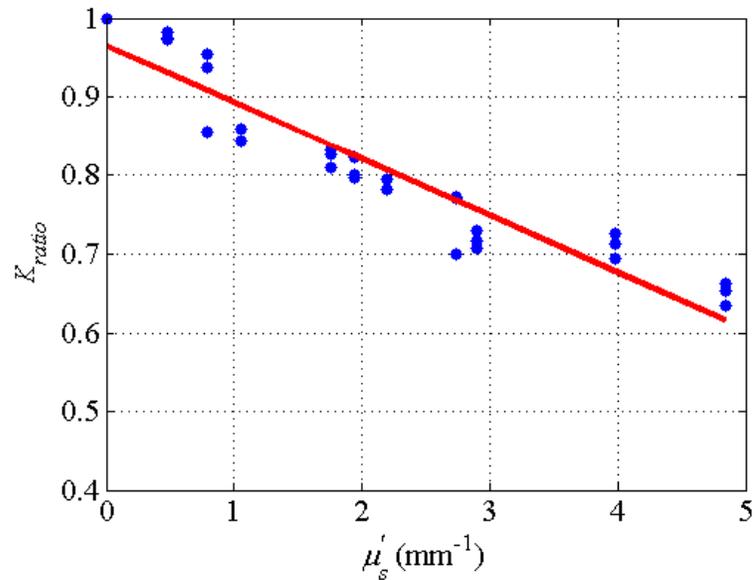
Figure 33a. K_{ratio} vs. reduced scattering coefficient. A strong negative correlation (r^2=0.95) was found between the two variables. The slope of the best fit line was -0.072.
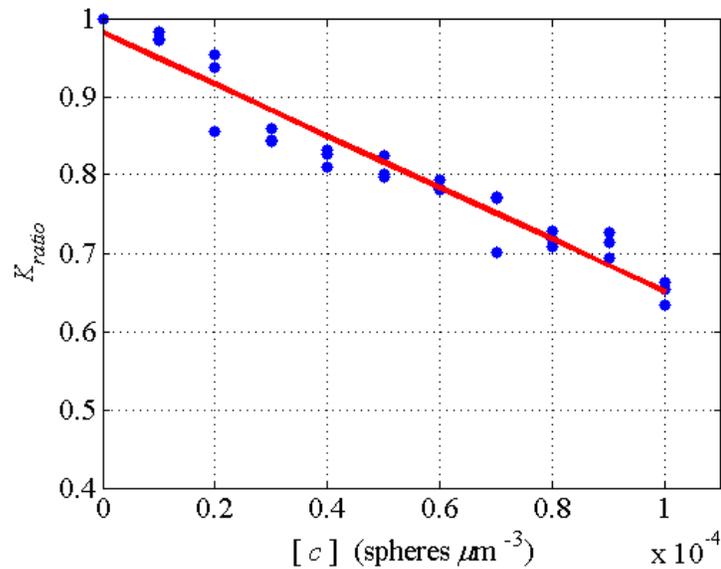
Figure 33b. K_{ratio} vs. scatterer concentration. A strong negative correlation (r^2=0.97) was found between the two variables. The slope of the best fit line was -3.3e-3.

The next set of experiments examined the relationship between the velocity of the moving fluid and speckle contrast. Recall from above, that these experiments were conducted with samples having a $\mu_s' = 2.2$ mm^{-1}. This value was somewhat arbitrarily chosen because it lies near the middle of the range of scattering coefficients we examined. As above, a strong negative linear correlation was found between K_{ratio} and $\vec{v}$. The results are displayed in Fig. (34).
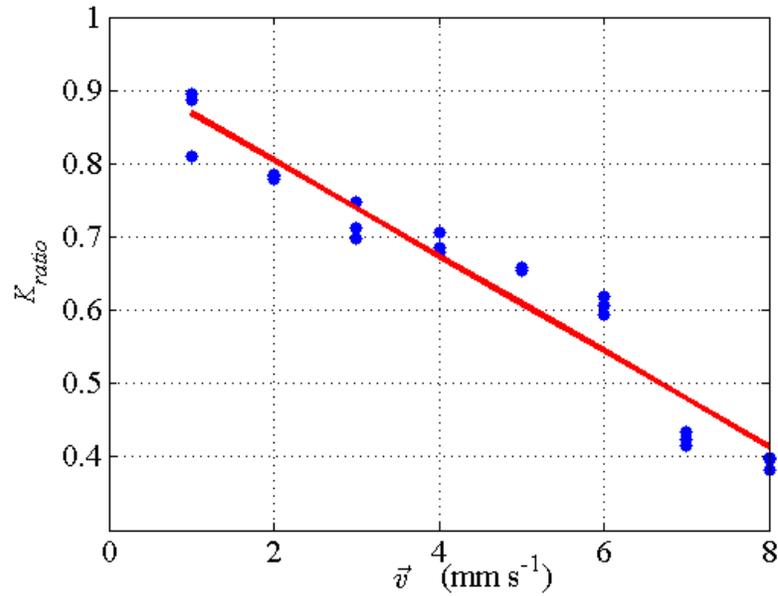
Figure 34. Relationship between speckle contrast and the velocity of the moving fluid. The fluid phantom had a reduced scattering coefficient of 2.2 mms^{-1}. The correlation coefficient, $r^2 = 0.96$.

The linear least-squares regression line was described by the equation:

$$K_{ratio} = -0.065\vec{v} + 0.934 \quad \left(r^2 = 0.96\right).$$ (19)

It is worth noting that the slope of this line is of the same order as the slope of the K_{ratio} vs μ_s' line. This observation appears to indicate that LSCI is equally sensitive to changes in velocity and scatterer concentration.

Combining the above results allows for an investigation into the sensitivity of LSCI to advective flux density, $\vec{v}[c]$. Because the results thus far indicate equal sensitivity to both velocity and scatterer concentration, $\vec{v}$ was held constant at $\vec{v} = 5$ mms^{-1} and $[c]$ was

varied from $0 \leq [c] \leq 1e-4$ spheres per cubic micron. Figure 35 shows the dependency of K_{ratio} on $\vec{v}[c]$.
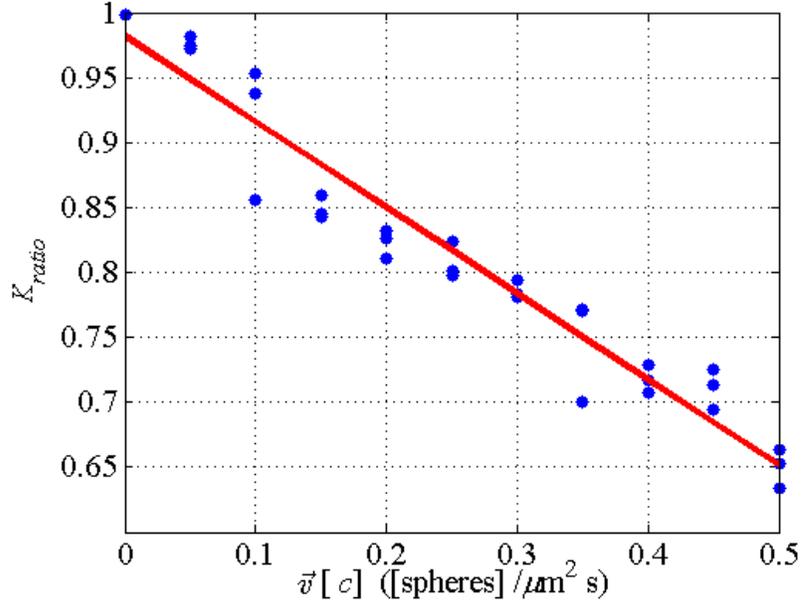
Figure 35. Relationship between K_{ratio} and advective flux. A strong

negative linear relationship was found ($r^2 = 0.97$).

Speckle contrast was found to decrease monotonically with increasing advective flux density following the linear relationship:

$$K_{ratio} = -0.66\vec{v} + 0.982 \quad \left(r^2 = 0.97 \right). \tag{20}$$

This result clearly demonstrates that LSCI is sensitive to advective flux density.

It is certainly worth noting that the *y*-intercept is approximately 1.0. It was demonstrated above that the glass tube had essentially no influence on the contrast values, so a *y*-intercept of 1.0 should be expected, assuming, as we did, that the first term on the

RHS of Eq. (12), that is the diffusive flux term, $\frac{\partial[c]}{\partial x} = 0$. That the y-intercept is ~1.0, then, confirms the assertion that these experiments explicitly examined the influence of advective flux on LSCI.

5. Discussion

The results clearly demonstrate a negative linear dependence of K on both $[c]$ and $\vec{v}$ for our experimental arrangement. It is worth noting that the experimental results presented herein indicate that LSCI is approximately equally sensitive to both changes in velocity and changes in scatterer concentration. This is significant in that a change in scatterer concentration may be mistaken for a change in velocity when using LSCI. This implies that in order to properly interpret LSCI data, which is typically used to assess a change in blood flow (or speed, or velocity) a change in scatterer concentration must be either logically or experimentally ruled out. Such a change may arise from a change in hematocrit level, for example. In most studies, a change in hematocrit can be ruled out physiologically. However, one could envision LSCI being used in time-course studies were a change in hematocrit is possible or when comparing LSCI results between individuals, who may have different hematocrit. In these cases, the results presented here indicate that $[c]$ must be considered in the interpretation of those results. A more detailed analysis of this is needed.

Our experiments were intentionally devised so as to focus on the second term on the RHS of Eq. (12). That is, our experimental arrangement focused on the sensitivity of LSCI to advective flux density, $\vec{v}[c]$. An underlying assumption is that the diffusional

flux term of Eq. (12) is small. That is, $-D\dfrac{\partial[c]}{\partial x} \square \ \vec{v}_x[c]$. Other studies have focused more

on the diffusional flux term, and although not couched in mass transport terms,

demonstrated a clear dependence of LSCI on $\dfrac{\partial[c]}{\partial x}$.[12]

It is worth asking the question of how to interpret the *y*-intercept of Fig. (35) had it

not been unity and was something less than 1.0. The theoretical development and the

experimental results appear to indicate that any reduction in K_{ratio} when $\vec{v}[c]=0$ must be

due to random diffusional flux (i.e., the first term on the RHS of Eq. (12)). Thus, the theory

and experiments in this paper suggest an approach to determining the relative contributions

of diffusional flux (unordered motion) and advective flux (ordered motion) to the reduction

in speckle contrast. This is discussed in more detail below with regards to choosing a

proper statistical model to relate speckle contrast to particle motion.

Another issue to consider is that in our experiments, a solid, static scattering block

was below and in the same DOF as the dynamic, flowing scatterers. One could argue that

our experiments merely demonstrate that as $[c]$ increases, the influence of the static

scatterers, which by themselves should result in a high contrast value of $K \rightarrow 1.0$ is

reduced. The usual argument explaining this phenomenon is that as more and more moving

scatterers are introduced to the imaged volume, the number of speckle fluctuations will

also be increased, diminishing the overall influence of the static scatterers. If we were

considering laser Doppler flowmetry, we would make the argument that the fraction of

Doppler-shifted photons increases with an increase in the number of scatterers.[3] Indeed,

these arguments are correct. However, they do not diminish our results that indicate that LSCI is sensitive to advective flux.

The one cautionary note regarding the influence of static scatterers is that the proportionality constants that we report relating K_{ratio} to $[c]$ may not be entirely generalizable and may vary depending upon the experimental arrangement due to the scattering properties of the background material. However, by reporting K_{ratio} values as opposed to purely values of K, this influence of background scatterers is reduced and the results should be fairly generalizable. Note that in living tissue, there are no scattering volumes in which the speckle arising from the volumes has a decorrelation time $\tau_c \rightarrow \infty$. That is, there are no static scatterers and speckle from living tissue will always have a finite τ_c.

The question of the proper statistical model for describing the underlying motion of the scattering particles and ultimately relating this model to the observed contrast arises frequently in the LSCI literature where it is either directly addressed,[2,3] or one statistical model or the other is implicit in the analysis.[5] The two limiting behaviors as discussed above in the Theory section are random (Brownian) motion and ordered motion. Ultimately, these two limiting behaviors give rise to Lorentzian and Gaussian correlation functions, respectively, that relate contrast K and the decorrelation time, τ_c, of the observed speckle. Frequently, the discussion surrounding the proper choice of the statistical model gives the appearance that this is a binary choice. One has to either assume a Gaussian or a Lorentzian model. Although it has been proposed that a Voigt model might

125

be a logical alternative and that this Voigt model is a convolution of the Lorentzian and Gaussian line shapes.[8]

The theoretical development, above, resulting in Eq. (7) for the 2-D case and Eq. (12) for the 1-D case, along with the experimental findings, lends credence to the choice of a Voigt model. From these equations, it becomes apparent that this model selection is not binary, but is actually points along a continuum, with the Lorentzian and Gaussian models serving only as the outer limits to the continuum. Inspection of Eq (12) reveals that LSCI is sensitive to both diffusive flux, J_L and advective flux density, J_G, where the total flux, $J_{KK} = J_L + J_G$. If the particle motion is assumed to be entirely random (Brownian), then LSCI is revealing J_L and the Lorentzian model should be adopted. Alternatively, if the particle motion is assumed to be entirely ordered, then LSCI is revealing J_G and the Gaussian model should be adopted. However, in most normal cases of interest both components of total flux will be present and the appropriate statistical model is some combination between the Lorentzian and Gaussian models. As suggested above, one solution to this is to employ a Voigt model[8] which is the convolution of the Lorentzian and Gaussian models, or some other weighted linear combination of the two, where the weights reflect the relative contributions of diffusive flux and advective flux. Readers are referred to Duncan and Kirkpatrick[8] for more details on this model. When viewed in terms of mass transport, then, it becomes apparent that the oft cited binary decision between the Lorentzian and Gaussian models is a false decision and that these two models are simply limiting behaviors governed by the diffusion with drift equation.[9]

In summary, we have viewed LSCI from a mass-transport perspective and demonstrated that by adopting the diffusion with drift equation (Eq. (12) for the 1-D case), a theoretical basis for understanding the sensitivity of LSCI to both particle concentration and speed (or velocity) can be shown. Furthermore, this same mass-transport approach, invoking the diffusion with drift equation, draws a mathematical and physical linkage between random and ordered motion of particles. This single equation (*e.g.,* Eq. (12)) adequately describes both behaviors as limiting conditions on contrast values. Finally, when discussing LSCI, we encourage the use of the term flux, and in particular diffusive flux and advective flux density (as opposed to terms such as perfusion, flow, velocity and speed) to describe the physical variable to which LSCI is sensitive.

References

1. A. F. Fercher and J.D. Briers, 'Flow visualization by means of single-exposure speckle photography," *Opt. Commun.* **37**(5), 326-330 (1981).

2. D. A. Boas and A. K. Dunn, "Laser speckle contrast imaging in biomedicine," *J. Biomed. Opt.* **15**(1), 011109 (2010).

3. D. Briers et al., "Laser speckle contrast imaging:theoretical and practical limitations," *J. Biomed. Opt.* **18**(6) 066018 (2013).

4. R. Bonner and R. Nossal, "Model for laser Doppler measurements of blood flow in tissue," *Appl. Opt.* **20**(12), 2097-2107 (1981).

5. A. Dunn et al., "Dynamic imaging of cerebral blood flow using laser speckle," *J. Cereb. Blood Flow Metab.* **21,** 195-201 (2001).

6. Kirby, B.J., *Micro – and Nanoscale Fluid Mechanics*, Cambridge University Press, Cambridge, UK, 2010.

7. J. W. Goodman, "Some effects of target-induced scintillationson optical radar performance," *Proc. IEEE* **53**(11), 1688-1700 (1965).

8. D. D. Duncan and S. J. Kirkpatrick, "Can laser speckle flowmetry be made a quantitative tool?," *J. Opt. Soc. Am* **25**(8), 2088-2094 (2008).

9. Berg, H.C., *Random Walks in Biology*, Princeton University Press, Princeton, NJ, USA, 1983.

10. M. Hammer, A. N. Yaroslavsky and D. Schweitzer, "A scattering phase function for blood with physiological haematocrit," IOP Publishing Ltd., 0031-9155/01/030065 (2001).

11. D. D. Duncan, S. J. Kirkpatrick, and R. K. Wang., "Statistics of local speckle contrast," *J. Opt. Soc. Am A* **25**, 9-15 (2008).

12. R. Bandyopadhyay, et al., "Speckle-visibility spectroscopy: A tool to study time-varying dynamics," *Rev. Sci. Instrum.* **76** 093110 (2005).

Chapter 6
(Paper 3)

Optical Vortex Behavior in Dynamic Speckle Fields[1]

Sean J. Kirkpatrick, Kosar Khaksari, Dennis Thomas, Donald D. Duncan, "Optical Vortex Behavior in Dynamic Speckle Fields", Journal of Biomedical Optics, 17(5), pp, 050504(1), − 050504(3), (2012). (See **Appendix A** for copyright transfer agreement that give permission to use this material.)

Contribution of Authors:

Sean J. Kirkpatrick: Principal Investigator, data evaluation, writing and edition

Kosar Khaksari: Ran the experiments; Developed theory, Wrote computer code, Analyzed data, Wrote manuscript

Donald D. Duncan: helped to develop some of the mathematics and computer codes

Sean J. Kirkpatrick[1], *Kosar Khaksari, Dennis Thomas*
Department of Biomedical Engineering
Michigan Technological University
1400 Townsend Dr.
Houghton, MI 49931
906-487-2167 (phone)
sjkirkpa@mtu.edu

Donald D. Duncan
Department of Electrical and Computer Engineering
Portland State University

---

[1] The material contained in this chapter was previously published in the *Journal of Biomedical Optics*.

Fourth Avenue Building
1900 SW 4th Avenue, Suite 160
Portland OR, 97201

[1]Corresponding Author

Key Words: Optical vortices, Phase singularities, Laser speckle, Biological dynamics

Abstract. The dynamic behavior of phase singularities, or optical vortices, in the pseudo-phase representation of dynamic speckle patterns was investigated. Sequences of band-limited, dynamic speckle patterns with pre-determined Gaussian decorrelation behavior were generated and the pseudo-phase realizations of the individual speckle patterns were calculated via a 2-D Hilbert transform algorithm. Singular points in the pseudo-phase representation were identified by calculating the local topological charge as determined by convolution of the pseudo-phase representations with a series of 2×2 nabla filters. The spatial locations of the phase singularities were tracked over all frames of the speckle sequences and recorded in 3-D space (x, y, f), where f is frame number in the sequence. The behavior of the phase singularities traced 'vortex trails' that were representative of the speckle dynamics. Slowly decorrelating speckle patterns resulted in long, relatively straight vortex trails, while rapidly decorrelating speckle patterns resulted in tortuous, relatively short vortex trails. Optical vortex analysis such as described herein can be used as a descriptor of biological activity, flow and motion.

131

Introduction

Speckle fields arising from scattering media such as biological tissue contain locations of zero intensity and undefined phase. The phase in the immediate vicinity of these singular points rotates through a full 2π radians along a circular path surrounding these points. This spiral behavior of the phase values has led to these singular points being referred to as optical vortices. Optical vortices may be described in terms of topological charge n_t with each vortex typically possessing a topological charge of ± 1, depending upon the direction of rotation of the phase values,[1,2] however higher order charges are possible. As a direct outcome of the principle of conservation of charge, vortices only appear in pairs, with one member of the pair possessing a topological charge of $+1$ and the other pair member possessing a topological charge of -1. This further implies that optical vortices can only be created and destroyed in pairs. As the scattering particles in the dynamic media move, the phase in the scattered field, and therefore the locations of the optical vortices, also changes in a related fashion. The behavior of optical vortices and beams that contain optical vortices has received much attention lately.[2-4] Much of this attention has focused on the density and the behavior of the optical vortices as the field propagates through a turbulent atmosphere.[2,4] Sendra et al.[5] evaluated vortex behavior in dynamic speckle images and pointed to the biological and industrial applications of analyzing vortex activity. They note that there is a strong relationship between the motion of a scattering diffuser and the resultant motion of the optical vortices in the observed dynamic speckle pattern.

132

The apparent robustness of optical vortices combined with the observation that the vortices in a dynamic, stochastic optical field move in a manner that is correlated with the motion of the scattering particles (or medium) implies that optical vortex behavior may be used as a surrogate for understanding the dynamic behavior of scattering media. Particular applications in biomedicine where vortex analysis may be of use include investigating the dynamic behavior of scattering suspensions, particle sizing, monitoring cellular activity, and microcirculation studies, for example. The purpose of this Letter is to demonstrate one approach to studying optical vortex behavior in simulated speckle intensity patterns that exhibit dynamic behavior similar to that observed when coherent light is scattered by biological tissues.

To investigate the spatio-temporal behavior of optical vortices in dynamic speckle patterns, we generated sequences of band-limited dynamic speckle patterns in the Matlab environment using the numerical method we described in an earlier publication.[6] Using this approach, we were able to generate fully developed, dynamic speckle patterns with very well controlled first and second order statistics and also with prescribed decorrelation behavior. Following the generation of the speckle sequences, the pseudo-phase $\hat{\phi}$ [7] of the speckle patterns was generated using a 2-D Hilbert transformation of the speckle patterns. It must be noted that this representation of $\hat{\phi}$ is not unique and an entirely different representation of the pseudo-phase can be generated if, for example, one were to employ a 2-D Fourier transform in place of the Hilbert transform. This is the classic phase retrieval problem. However, regardless of the numerical method used to generate the pseudo-phase, the operation simply exploits information already present in the signal without adding any new information.[5] Once a 2-D representation of $\hat{\phi}$ is generated, the singular points that

133

identify the optical vortices can be located. These points then can be tracked as the speckle pattern dynamically evolves.

We begin our formal discussion of the problem by noting that the complex representation of an optical field and its relationship to the intensity image is given by

$$U(x,y,z;t) = A(x,y,z)\exp[i\omega t]$$

(1)
$$I(x,y,z) = \lim_{T\to\infty} \int_{-T/2}^{T/2} |U(x,y,z;t)|^2 \, dt = |A(x,y,z)|^2$$

where the phasor amplitude of the field, A, is itself a complex-valued function of space.

The local true phase of the field is defined as usual as $\phi(x,y) = \tan^{-1}\dfrac{\text{Im}[U(x,y)]}{\text{Re}[U(x,y)]}$. To generate a 2-D representation of the pseudo-phase $\hat{\phi}(x,y)$ from $I(x,y)$ we use a Hilbert transform in 2 dimensions such that $\hat{U}(x,y) = I(x,y) + jH\{I(x,y)\}$

and

(2)
$$\hat{\phi}(x,y) = \tan^{-1}\frac{\text{Im}\{\hat{U}(x,y)\}}{\text{Re}\{\hat{U}(x,y)\}}$$

The phase singularities are defined in terms of n_t:

(3)
$$n_t \equiv \frac{1}{2\pi}\oint_c \nabla\hat{\phi}(x,y)\cdot d\vec{l} \quad ,$$

where $\nabla\hat{\phi}(x,y)$ is the local phase gradient and the contour integral is taken over path l on a closed loop c around the vortex. It is clear that $n_t = 0$ everywhere $\hat{\phi}$ is differentiable, except at the singularity where the phase is undefined. Since $\hat{\phi}$ is a continuous function, and has continuous first derivatives, by Stokes theorem we can see that

(4)
$$n_t \equiv \frac{1}{2\pi} \oiint_c \nabla \hat{\phi}(x,y) \cdot d\vec{l} = \frac{1}{2\pi} \iint_D \left(\frac{\partial^2 \hat{\phi}}{\partial x \partial y} - \frac{\partial^2 \hat{\phi}}{\partial y \partial x} \right) \partial x \partial y$$

where D is a disc of radius a enclosing the circular path over which n_t is evaluated.[8,9] This formulation suggests that the locations of the optical vortices can be determined efficiently through a series of convolution operations:

$$n_t = \hat{\phi}(x,y) \otimes \nabla_1 + \hat{\phi}(x,y) \otimes \nabla_2 + \hat{\phi}(x,y) \otimes \nabla_3 + \hat{\phi}(x,y) \otimes \nabla_4$$

(5)

where

$$\nabla_1 = \begin{pmatrix} 0 & 1 \\ 0 & -1 \end{pmatrix}; \quad \nabla_2 = \begin{pmatrix} 1 & -1 \\ 0 & 0 \end{pmatrix}; \quad \nabla_3 = \begin{pmatrix} -1 & 0 \\ 1 & 0 \end{pmatrix}; \quad \nabla_4 = \begin{pmatrix} 0 & 0 \\ -1 & 1 \end{pmatrix}$$

and $\otimes$ is the convolution operator. Figures 36(a), 36(b), and 36(c) display a numerically synthesized speckle pattern, its pseudo-phase representation, and the pseudo-phase representation with the optical vortices indicated by the superimposed stars and circles, respectively. Here, the vortices with positive topological charge are indicated by green stars and those with a negative topological charge by red circles.

Two sequences of 100 dynamic speckle patterns each were generated numerically. These speckle sequences displayed temporal decorrelation behavior as shown in Fig. 37. From this figure, it is seen that both sequences exhibited Gaussian decorrelation behavior, but with drastically different characteristic times. The 'fast' sequence was defined by a time constant of $\tau_f \cong 9$ frames, while the 'slow' sequence was characterized by a longer time constant $\tau_s \cong 36$ frames. For both sequences, pseudo-phase representations were generated for each frame and the locations of the vortices identified. These locations were

then plotted in (x, y, f), where f is frame number in the sequence. Following the convention of Fig. 36(c), the positive charged vortices were plotted in green stars and the negatively charge vortices were plotted in red circles.

The results of this operation are shown in Figs. 38(a) and 38(b). Several observations can be made regarding these figures. A key observation is that the vortices are robust. That is, individual vortices persist through at least several frames, even in the rapidly decorrelating speckle example. The locations of the individual vortices over several frames trace a path, or a vortex trail. In the rapidly decorrelating speckle sequence, the vortex trails are relatively short and tortuous (Fig. 38(a)). However, in the slowly varying sequence, the vortex trails are quite long and trace a much straighter path (Fig. 38(b)). It is clear that in the limit of a truly static speckle sequence, the vortices would maintain their (x, y) positions through all frames, f. Careful examination of Figs. 38(a) and 38(b) also reveals locations where positively and negatively charged optical vortices annihilate each other. Elsewhere, new vortices are formed. These events always occur in pairs (*i.e.*, both a positively and a negatively charged vortex is either destroyed or created) and arise due to the conservation of charge principle.[4]

In an actual, physical setting, the motion of the speckles arising from scatter from biological tissues arises from numerous sources, including but not limited to the random motion of cellular activity and from the more ordered motion of red blood cells, for example. We may generalize and simply say that motion in these speckle patterns is from biological activity. From this discussion, it becomes apparent that the spatio-temporal behavior of optical vortex trails is an indicator of biological activity and that specific imaging configurations and experiments could be designed to focus on one particular type

136

of motion. For example, one could coherently image cell sheets and use the above vortex analysis to quantify cellular metabolic activity. Alternatively, it is feasible that one could coherently image the microcirculation and use vortex analysis to study microcirculatory flow.

References

1.   M. S. Soskin, V. N. Gorshkov, M. V. Vasnetsov, J. T. Malos, and N. R. Heckenberg, "Topological charge and angular momentum of light beams carrying optical vortices," *Physical   Rev. A* 56(5), 4064-4075 (1997).

2.   M. Chen, C. Dainty, and F. S. Roux, "Speckle evolution with multiple steps of least-squares   phase removal," *Physical Rev. A* 84, 023846 (2011).

3.   G. H. Kim, H. J. Lee, J. U. Kim, and H. Suk, "Propagation dynamics of optical vortices with   anisotropic phase profiles," *J. Opt. Soc. Am. B* 20(2), 351-359 (2003).

4.   G. Gbur and R. K. Tyson, "Vortex beam propagation through atmospheric turbulence and   topological charge conservation," *J. Opt. Soc. Am. A* 25(1), 225-230 (2008).

5.   G. H. Sendra, H. J. Rabal, R. Arizaga, and M. Trivi, "Vortex analysis in dynamic speckle   images," *J. Opt. Soc. Am. A* 26(12), 2634-2639 (2009).

6.   D. D. Duncan and S. J. Kirkpatrick, "The copula: a tool for simulating speckle dynamics," *J. Opt.   Soc. Am. A* 25(1), 231-238 (2008).

7.   W. Wang, T. Yokozeki, R. Ishijima, A. Wada, Y. Miyamoto, M. Takeda, and S. G. Hanson,   "Optical vortex metrology for nanometric speckle displacements," *Opt. Express* 14(1),120-127   (2006).

8.   M. A. Bray, S. F. Lin, R. R. Aliev, B. J. Roth, and J. P. Wikswo, Jr., "Experimental and   theoretical analysis of phase singularity dynamics in cardiac tissue," *J. Cardiovasc. Electrophysiol.* 12(6), 716-722 (2001).

9.   E. G. Abramochkin and V.G. Volostnikov, "Relationship between two-dimensional intensity and   phase in a Fresnel diffraction zone," *Optics Communications* 74(3–4), 144-148 (1989).

Figures:

Figure. 36 Example of a band-limited numerically generated speckle pattern (a), its pseudo-phase representation (b) and the pseudo-phase representation with the positively charged (green stars) and negatively charged (red circles) optical vortices identified (c).

Figure. 37 Autocorrelation functions of the rapidly decorrelating speckle sequence versus the more slowly decorrelating speckle sequence used in this study.

Figure. 38 Three-dimensional representation of the vortex trails for the rapidly decorrelating speckle sequence (a) and the more slowly decorrelating speckle

sequence(b). The green stars represent the positively charged vortices and the red circles

represent the negatively charged vortices.

Chapter 7
(Paper 4)

Nematic Liquid Crystal Spatial Light Modulator for Mimicking Laser Speckle Contrast Imaging[1]

Mitchell A. Kirby, Kosar Khaksari, Sean J. Kirkpatrick, "Nematic Liquid Crystal Spatial Light Modulator for Mimicking Laser Speckle Contrast Imaging", Dynamics and Fluctuations in Biomedical Photonics XII, Valery V. Tuchin; Kirill V. Larin; Martin J. Leahy; Ruikang K. Wang, Editors, Proceedings of SPIE Vol. 9322 (SPIE, Bellingham, WA), 932203, (2015). (See **Appendix A** for copyright transfer agreement that give permission to use this material.)

Contribution of Authors:

Mitchell A. Kirby: Ran experiments, Developed optical layout
Sean J. Kirkpatrick: Principal Investigator, data evaluation, writing and edition
Kosar Khaksari: Ran the experiments; Developed theory, Wrote computer code, Analyzed data, Wrote manuscript

Mitchell A. Kirby, Kosar Khaksari, Sean J. Kirkpatrick[*]

*Corresponding Author: E-mail: sjkirkpa@mtu.edu

---

[1] The material contained in this chapter was previously published in the *Journal of Biomedical Optics*.

Michigan Technological University, Department of Biomedical Engineering, 1400 Townsend Dr., Houghton, MI, 49931 USA

Abstract. Before laser speckle contrast imaging (LSCI) can be used reliably in a clinical setting, there are several theoretical and practical issues that must be addressed. In order to address some of these issues, an electro-optical system that utilizes a nematic liquid crystal spatial light modulator (SLM) to mimic LSCI experiments was assembled. Using this system, experimental parameters that influence LSCI were varied in a systematic fashion. Herein, the performance and application of the system for investigating LSCI is demonstrated. Specifically, the ability of the SLM-based system to generate speckle patterns with a controlled minimum speckle size, probability intensity distribution, and decorrelation behavior is shown. The ability to produce LSCI images that mimic flow assuming both Lorentzian and Gaussian flow models is presented. By eliminating many experimental parameters, this system is capable of serving as a useful intermediary between computer simulation and physical experimentation.

145

1.   INTRODUCTION

Laser speckle contrast imaging (LSCI) is a simple, non-invasive, low cost method that offers the potential of assessing blood flow and perfusion in near-real time. It has become commonplace for LSCI and its variations to be used in full-field qualitative visualization of blood flow.[1,2]   However, there are numerous challenges, as well as theoretical and practical limitations, that remain unresolved in using LSCI to make quantitative measurements of flow and perfusion.[3]   Furthermore, even for qualitative assessment of blood flows, there are compounding issues such as changes in hematocrit that manifest as changes in bulk blood optical properties that appear identical to relative changes in blood flow.   Without *a priori* knowledge of the scattering and absorption coefficients of the blood, it is impossible to discriminate between changes in flow and changes in blood optical properties.[4]   In addressing these issues, it is often difficult to isolate the variables under investigation due to the interdependence of many of the experimental parameters. For example, flow (or velocity), camera integration time, and assumed flow model all interact with each other to yield a particular contrast value.[3] While phantom flow studies are useful, there are often issues that arise from the experimental design, such as the effects of tubing on the scattering characteristics, unanticipated fluctuations in the flow pattern, clumping of scatterers, and challenges with reproducibility. Additionally, there remains an uncertainty as to the proper flow model used to describe the stochastic behavior of the scattering particles.[3]

The goal of this paper is to present an optical system incorporating a spatial light modulator that can faithfully reproduce laser speckle contrast images in a highly controlled and reproducible fashion and permits for the isolation of a single experimental parameter

while not varying any others. This optical system permits control of the speckle size, the decorrelation behavior of the 'scatterers' (and the resulting speckle patterns), the first-order speckle statistics of the speckle patterns (*i.e.* the intensity probability distribution), the ratio of static to dynamic scatterers, the mathematical relationship between contrast values and the assumed flow model, the camera integration time and frame rate, and all other data acquisition variables. The objective of this system is to generate dynamic speckle patterns that are statistically similar to experimental speckle patterns observed from biological tissue in order to address single LSCI experimental parameters and their effects on contrast image quality. The overarching goal is to employ this electro-optical system to optimize the approach to this imaging modality.

2   METHODS & MATERIALS

The optical layout can be seen in Figure 39. A stabilized HeNe laser (633nm) illuminated a 512 x 512 spatial modulator (Boulder Non-linear Systems) via a beam splitter that returned the scattered light to a CMOS camera through a $4f$ imaging system with an adjustable aperture stop located in the Fourier plane of the front lens. Varying the diameter of the aperture opening changes the minimum speckle size observed on the camera. Reducing the opening of the aperture resulted in larger speckles, while increasing the diamter resulted in smaller speckles.[5] The light passed through a neutral density filter, allowing adjustable incident intensity. The beam was passed through a spatial filter and collimated before passing through a λ/2 plate. The half-wave plate served to orient the polarization of the incoming light in the vertical plane so that the SLM functioned in the

'phase-only' mode. By operating in the phase-only mode, the light backscattered from the SLM was de-phased in the same way as if it were scattered from a rough surface or a scattering volume. The polarizer in the imaging arm was oriented in the same plane as the incident light. This resulted in observing only a single component of the electromagnetic wave on the CMOS array and thus generating a polarized speckle pattern.

To generate the speckle patterns from the SLM, a sequence of phase screens, typically 50 frames in length, was loaded to the SLM. The phase screens were generated by filling a 512 x 512 array with complex numbers of unit amplitude, and phases uniformly distributed over $(0, 2\pi)$. Thus, the light scattered from each individual SLM element was dephased and the resulting scattered wavefront had an identical phase distribution. The scattered light was, however, still temporally and spatially coherent allowing for random interference to occur when the scattered light impinged on the CMOS chip of the camera, resulting in a speckle pattern.

By controlling the temporal decorrelation behavior of the phase screens, the temporal decorrelation behavior of the resulting speckle patterns was varied.[6] In addition to controlling the rate of temporal decorrelation, the shape (*e.g.,* Gaussian, exponential, etc.) of the decorrelation curve was also variable.[6] Different regions on the SLM were capable of displaying different decorrelation behaviors. Thus regions of 'fast' decorrelation and 'slow' decorrelation were able to be created to mimic an LSCI image of a vessel with flow (fast) surrounded by slower moving tissue regions.

To generate the LSCI image seen in Figure 40 multiple sequential frames of the speckle patterns from the CMOS array were summed to simulate the finite exposure time that results in the contrast seen due to temporal averaging. Contrast was defined as

$$K(r) = \frac{\langle \sigma_i \rangle}{\langle \mu_i \rangle}$$

(1)

where μ_i is the mean intensity and σ_i is the standard deviation of the intensity of a 7 x7 window of pixels slid across the image at location r.[1] For a single, static, polarized speckle pattern, the global contrast attains a theoretical maximum of unity. For time averaged, dynamic speckle patterns the global contrast is less than unity. It should be noted, however, that these global contrast values have their own statistical distributions.[7]

3   RESULTS

Figure 40 demonstrates a simulated laser speckle contrast image using the SLM-based system. A 'vessel' region with flow in the center section of rows de-correlated at a faster rate than the surrounding pixels, which represents more slowly varying speckles from the surrounding 'tissue'.

A goal of this study was to demonstrate the ability to control both the first- and second-order statistics of the speckle patterns generated by the SLM. The first-order statistics of the speckle pattern are described by the intensity probability distribution function (PDF). For a polarized speckle pattern, the theoretical PDF is a negative exponential.[5] Figure 41a demonstrates the ability to reproduce a single speckle pattern with a negative exponential PDF. In cases where multiple speckle patterns are incoherently summed, the PDF of the resultant speckle pattern is described by a Rayleigh PDF. In practice, such a speckle pattern is seen when observing speckle from a volume scatterer, such as tissue, without using a polarizer to isolate a single component of the

electromagnetic field. Figure 41b demonstrates the system's ability to reproduce speckle with a Rayleigh PDF by summing on an intensity basis multiple individual, polarized speckle patterns. The number of speckle patterns that need to be summed to generate a speckle pattern with an intensity PDF as in Fig. 41a depends upon the decorrelation behavior of the speckle sequence. The lower the correlation between subsequent speckle patterns, the fewer individual patterns need to be summed. In the limiting case, only 2 speckle patterns are necessary if they are statistically independent from one another.[5]

To control the size of the speckle, the aperture stop in the Fourier plane of the front lens was varied. Figure 42a displays a single speckle pattern from the SLM and its power spectrum (Figure 42b), which was used to estimate the minimum speckle size in the pattern.[5] The minimum speckle size relative to the CMOS chip pixel size (5.2 μm) as the diameter of the aperture was varied is shown in Figure 42c.

Another goal of this study was to demonstrate the ability to control both the rate and the pattern of the temporal decorrelation of the speckle pattern sequences. To achieve this, we generated speckle patterns that exhibit Gaussian decorrelation behavior with varying time constants, as seen in Figure 43a, b, and c. Figure 43d also demonstrates our ability to change the shape of the autocorrelation function, showing a Lorentzian autocorrelation function plotted along with a Gaussian autocorrelation fucntion. When generating the phase screens, we invoke the Wiener-Khinchin theorem[8] to recall that an exponential and a Lorentzian form a Fourier pair, as does a Guassian and a Gaussian. That is, when the phase screens exhibited a Gaussian decorrelation behavior, the resulting speckle pattern sequence also exhibited Gaussian behavior. When the phase screens

exhibited an exponential decorrelation behavior, the speckle sequence exhibited Lorentzian behavior.

In LSCI, unlike laser Doppler measurements, the link between speckle contrast and flow (or velocity) can only be made if the velocity distribution is known. However, the actual velocity distribution of biological fluid is often unknown in LSCI experiments. Early work has assumed the flow of blood to exhibit either purely unordered (Lorentzian) or ordered (Gaussian) flow.[2, 9, 10] Theoretically, a Lorentzian velocity distribution is only appropriate for Brownian motion (purely random flow). Conversely, a Gaussian velocity distribution is technically only appropriate for purely ordered flow. In paractical situaations, it is likely that the true flow model lies somewhere between the Lorentzian and Gaussian models. Some workers have suggested what is essentially a rigid-body model that is simply the convolution of the Lorentzian and Gaussian flow model.[3] Because assumptions are made to describe the fluid velocity distribution, the unambiguous quantification of flow velocity from contrast values is not yet possible.

In addition to controlling the temporal decorrelation of the speckle images, we have also demonstrated our ability to reproduce contrast values that follow the theoretical curves using both accepted flow models.[1] The experimental contrast values were compared to the theoretical values as a function of the ratio of the speckle decorrelation time, τ_c, and the integration time, T. The results are shown in Figure 44, which displays a comparison of theoretical and experimental results.

4   CONCLUSIONS

We have shown the ability of our system to faithfully reproduce the speckle images

used in LSC imaging. Because our electro-optical system allows for fast experimentation and reproduction, this system provides a convenient and quantifiable platform to address many of the real-world complications that hinder the future development LSCI. It is hoped that through this approach, the fine details of LSCI can be explored in more detail and further development of the imaging modality as a reliable and inexpensive research and diagnostic tool can proceed.

5. Acknowledgements

References

1. D. A. Boas and A. K. Dunn*.,* "Laser speckle contrast imaging in biomedicine," *J. Biomed. Opt.* **15**(1), 011109 (2010).

2. D. Briers, D. D. Duncan, E. Hirst, S. J. Kirkpatrick, M. Larsson, W. Steenbergen, T. Stromberg, and O. B. Thompson*,* "Laser speckle contrast imaging: Theoretical and practical limitations," *J. Biomed. Opt*. **18**(6), 066018 (2013).

3. D. D. Duncan and S. J. Kirkpatrick, "Can laser speckle flowmetry be made a quantitative tool?," *J. Opt. Soc. Am. A* **25**(8), 2088–2094 (2008).

4. K. Khaksari, S.J. Kirkpatrick, "Effects of combined scattering and absorption coefficients on laser speckle contrast imaging values" *Proc. SPIE 9322, Dynamics and Fluctuations in Biomedical Photonics XII*, 93220U-1-4 (March 5, 2015).

5. J. W. Goodman, *Speckle Phenomena in Optics*, Roberts & Co., Englewood, CO, USA (2007).

6. D. D. D AND S. J. KIRKPATRICK, "THE COPULA: A TOOL FOR SIMULATING SPECKLE DYNAMICS," *J. OPT. SOC. AM. A* 25(1), 2231-237 (2008).

7. D. D. DUNCAN AND S. J. KIRKPATRICK, R. K. WANG, "STATISTICS OF LOCAL SPECKLE CONTRAST," *J. OPT. SOC. AM. A* 25(1), 9-15 (2008).

8. J. W. Goodman, *Statistical Optics*, Wiley, New York, NY, USA (2000).

9. A. F. Fercher and J. D. Briers, "Flow visualization by means of single- exposure speckle photography," *Opt. Commun*. **37**(5), 326–330 (1981).

10. J. D. Briers and S. Webster*,* "Laser speckle contrast analysis (LASCA): a non-scanning, full-field technique for monitoring capillary blood flow," *J. Biomed. Opt*. **1**(2), 174–179 (1996).

Figures
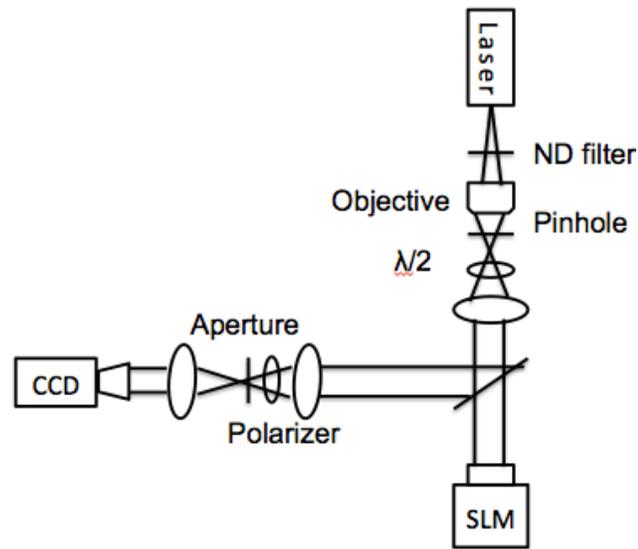
Figure. 39. Optical layout of the LSCI simulating system. The laser was a 2.5mW stabilized HeNe (633nm) and the image magnification equaled ~ 0.61.
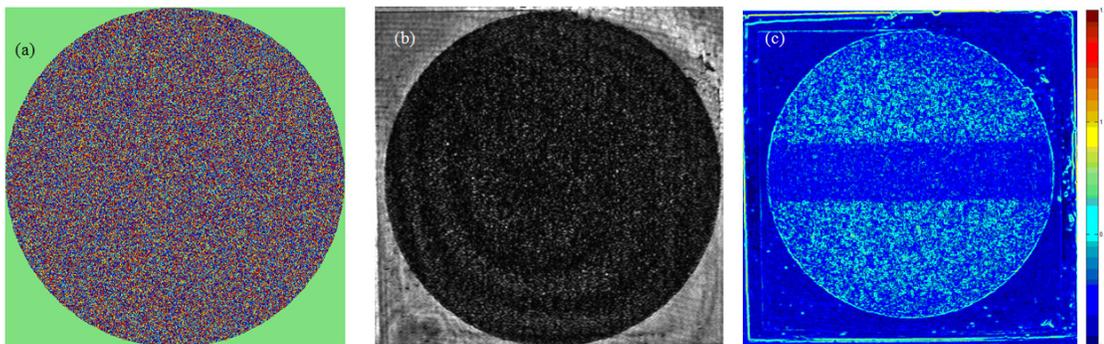
Fig. 40. (a) Phase screen loaded to the SLM. (b) The resulting imaged speckle pattern. (c) Simulated LSC image. The center rows in (2c) represent the 'flow' region. The contrast ratio between the static and dynamic regions was 4.108

Fig. 41. Intensity PDF's of SLM generated speckle patterns plotted along with numerically simulated (theoretically ideal) speckle patterns. (a) Fully developed, polarized intensity PDF showing both experimental (SLM) and theoretical speckle patterns in agreement. (b) Non-polarized intensity PDF showing both experimental and theoretical results in agreement.

155

Figure 42. (a) SLM generated speckle pattern (b) SLM generated speckle PSD. The minimum speckle size in this case was 4 pixels. (c) Variation in speckle size is plotted as a function of the aperture diameter, with a fitting function overlaid for future calibration.

(a)
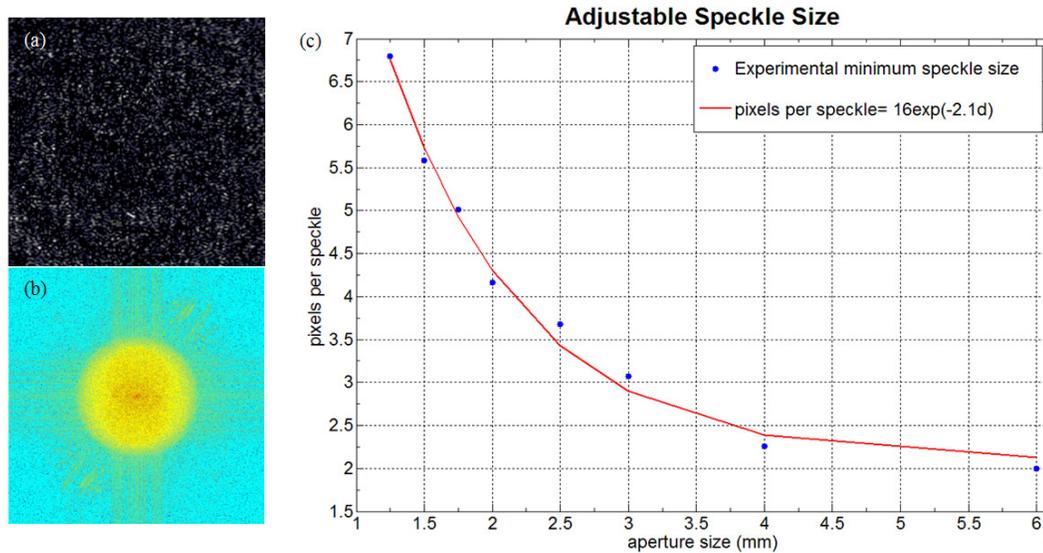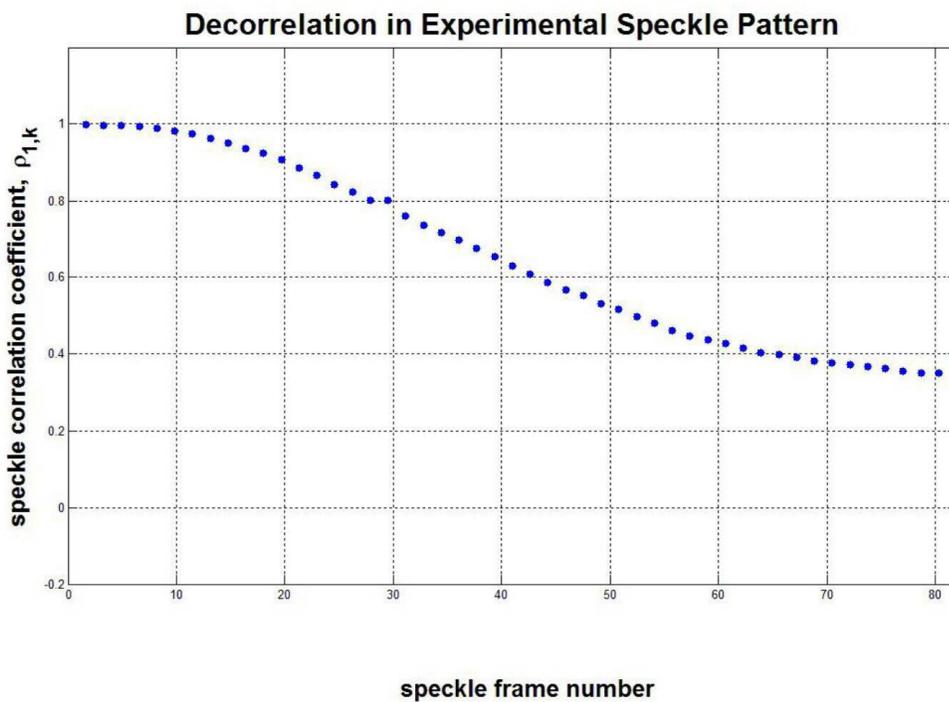
Decorrelation in Experimental Speckle Pattern

(b)

Decorrelation in Experimental Speckle Pattern

157
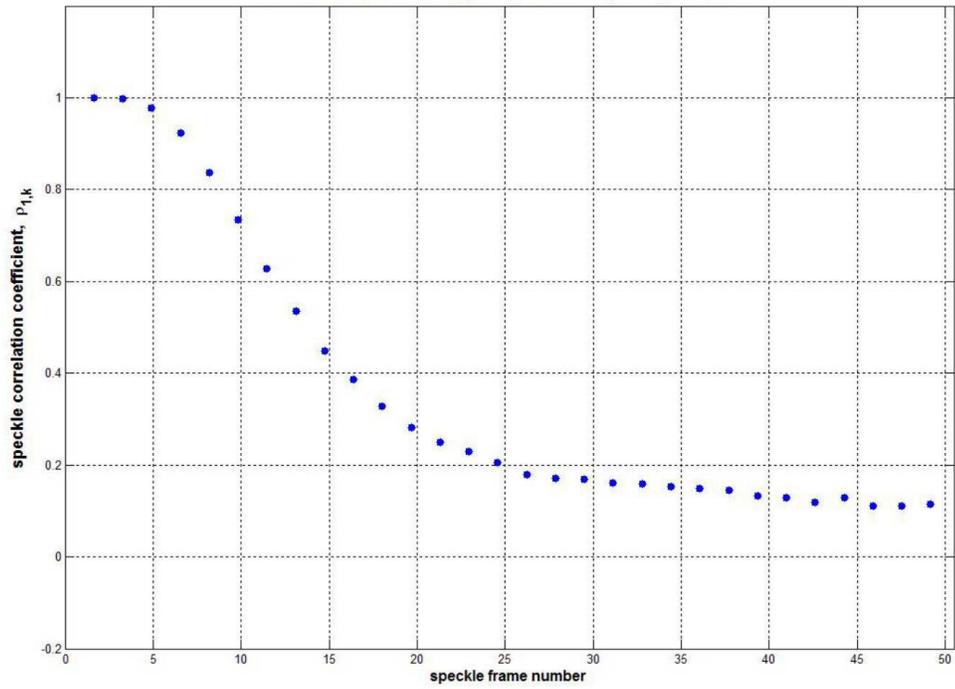
(c)
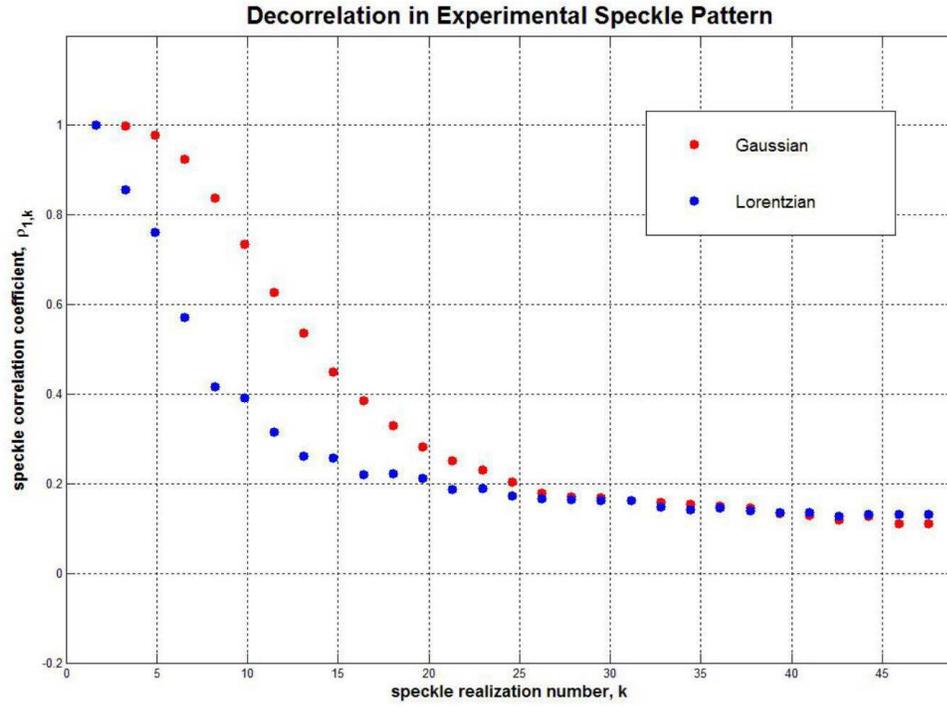
(d)

Figure 43(a-c). Decorrelation curves for SLM speckle patterns with different correlation
behaviors (top 3 figures). From the left, the decorrelation times were 70, 37 and 17 frames,
respectively. (**d**). Demonstration of both Lorentzian and Gaussian decorrelation behaviors
(bottom).
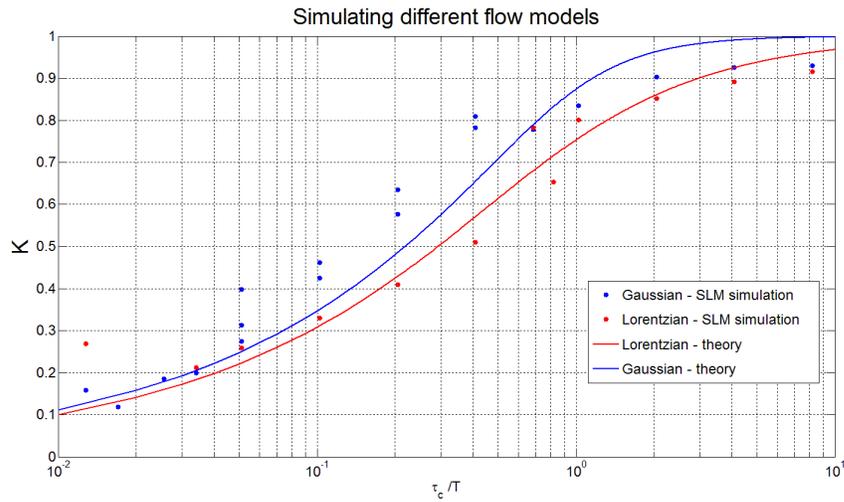
Figure 44. SLM simulated contrast vs $\frac{\tau_c}{T}$ for both a Gaussian and Lorentzian velocity distribution. The SLM set-up was able to faithfully reproduce the expected results for both flow models.

Chapter 8

(paper 5)

Effects of combined scattering and absorption coefficients on laser speckle contrast imaging[1]

Kosar Khaksari, Sean J. Kirkpatrick, "Effects of Scattering and Absorption Coefficients on Laser Speckle Contrast Imaging", Dynamics and Fluctuations in Biomedical Photonics XII, Valery V. Tuchin; Kirill V. Larin; Martin J. Leahy; Ruikang K. Wang, Editors, Proceedings of SPIE Vol. 9322 (SPIE, Bellingham, WA), 932203, (2015). (See **Appendix A** for copyright transfer agreement that give permission to use this material.)

Contribution of Authors:

Sean J. Kirkpatrick: Principal Investigator, data evaluation, writing and edition

Kosar Khaksari: Ran the experiments; Developed theory, Wrote computer code, Analyzed data, Wrote manuscript

Kosar Khaksari and Sean J. Kirkpatrick[*]

Department of Biomedical Engineering, Michigan Technological University, 1400 Townsend Dr., Houghton, MI 49931 USA

---

[1] The material contained in this chapter was previously presented in *Photonics West, SPIE*.

ABSTRACT

Laser Speckle contrast imaging (LSCI) is a non-invasive or minimally invasive method for visualizing blood flow and perfusion in biological tissues. In LSCI the motion of scattering particles results in a reduction in global and regional speckle contrast. A variety of parameters can affect the calculated contrast values in LSCI techniques, including the optical properties of the fluid and surrounding tissue. In typical LSCI where the motion of blood is of interests, hematocrit levels influence optical properties. In this work we considered the combined effects of both the scattering and absorption coefficients on LSCI measurements on a flow phantom. Fluid phantoms consisting of various concentrations of neutrally buoyant ~10 micron microspheres and india ink mixed with DI water were formulated to mimic the optical properties of whole blood with various levels of hematocrit. In these flow studies, it was found that an increase in μ_a and/or μ_s led to a decrease in contrast values when all other experimental parameters were held constant. The observed reduction in contrast due to optical property changes could easily be confused with a contrast reduction due to increased flow velocity. These results suggest that optical properties need to be considered when using LSCI to make flow estimates.

INTRODUCTION

Laser speckle contrast imaging (LSCI) and its many variants are full field imaging modalities that are commonly employed for the qualitative visualization of blood flow.[1-2] Yet, there still remain numerous issues that prevent LSCI from becoming a truly quantitative tool[3] that can be used reliably in time course studies, population comparisons, or even as an imaging modality that can be used to directly compare studies across laboratories or clinics. One unresolved issue is the influence of the optical properties on the speckle contrast levels observed in LSCI.

The purpose of the present study is to systematically investigate how changes in the reduced scattering coefficient μ_s' and the absorption coefficient μ_a influence the observed contrast values in an LSCI flow model. Conceptually, it is readily obvious that speckle contrast must be influenced by the number of moving scatterers in the imaging volume. If, for example, all of the scatterers were static, and only one polarization component of the scattered light is observed, then the contrast, K, defined as

$$K(\overline{r}) = \frac{\sigma_I(\overline{r})}{\mu_I(\overline{r})} \tag{1}$$

where μ_I is the mean intensity of a small window (7 x 7 in the present case) of pixels at location r and σ_I is the standard deviation of the intensity over the same window, will equal unity. If only a small number of moving scatterers are added, then the fluctuations in intensity due to these dynamic scatterers will lead to a small reduction in K. As the proportion of moving scatterers is increased, the relative influence of the moving scatterers

relative to the static scatterers will increase leading to a further reduction in contrast. Our experiments mimicked this thought experiment. Additionally, however, we also systematically added an absorber (india ink) to our flow phantom to observe the confounding influence of μ_a.

MATERIALS AND METHODS

A simple flow system was developed to provide controlled flow of a fluid phantom material through 2mm (i.d.) glass tubing where it was imaged with an LSCI system. The flow (at this point we do not need to differentiate between perfusion and velocity and the term 'flow' can be interpreted as velocity, either simply the magnitude or, since we have *a priori* knowledge of the direction, the full velocity vector with units of distance/time, or perfusion which involves a concentration and contrasts with *rate of flow* with units of volume per unit of time) system consisted of a mini-peristaltic pump controlled by a microcontroller (Arduino). Small diameter rubber tubing carried the flow to the imaging region where the rubber tubing connected to the aforementioned glass tubing. The glass tubing rested in a small groove (3mm diameter) on the surface of a white plastic block. The flow velocity was constant at 5mm/s for all experiments.

The LSCI imaging was accomplished by illuminating the flow phantom with a polarized 660nm diode laser (80mW) at a slight off-axis angle to help reduce specular reflection in the images. The backscattered dynamic speckle patterns were recorded with a CCD camera at 125 fps. The camera integration time was 6ms. A polarizer oriented to transmit the same polarization state as the illuminating light was placed in front of the camera. In order

to ensure that the speckle pattern was spatially sampled correctly (*i.e.,* minimum speckle size > 2 pixels), the lens was set to f/32. Care was taken to avoid specular reflection from the glass tubing. Sequences of 100 frames were taken for each experiment. All imaging and flow parameters we kept absolutely constant for all experiments. The only variables changed in a systematic manner were μ_s' and μ_a.

A MATLAB GUI controlled the flow system and the camera and also provided near-real time contrast images to the computer screen.

Flow phantoms were made by adding careful concentrations of a poly-disperse powder of 9-13 micron diameter glass microspheres (brand name of Luxil) to DI water. The spheres had a reported specific gravity of 1.1 g/cc. Solutions of microspheres were mixed so as to produce an array of 10 (11 including pure DI water) solutions with varying scattering coefficients. The scattering coefficients were measured using a ballistic transmission method. Subsequent inverse Mie scattering calculations revealed that although the solutions were poly-disperse, the scattering behavior mimicked that of an ~11 micron monodisperse system. Mie calculations yielded a scattering anisotropy of ~0.99. The resulting scattering coefficients of the flow phantoms ranged $0 mm^{-1} < \mu_s' < 6.8 mm^{-1}$ including the pure water sample.

Additionally, another array of 11 solutions containing india ink as an absorber were constructed. Absorption coefficients ranged $0 mm^{-1} < \mu_a < 0.065 mm^{-1}$.

The two sets of solutions were combined to create an 11 x 11 matrix of phantom solutions with varying scattering and absorption coefficients. Scattering coefficient was varied

across rows and absorption coefficient was varied across columns. Three samples of phantom solutions were made for each element of the matrix.

Two hundred raw speckle images were recorded per phantom sample as they flowed through the system, thus each experiment lasted only 1.6 sec. The field of view for each image included not only the glass capillary, but also portions of the white plastic block. This allowed for the generation of a ratio between the contrast calculated via Eq (1) from the static block and from the moving flow phantom material. Thus for the purposes of this study, $K_{Ratio} = \dfrac{K_{fluid}}{K_{block}}$.

RESULTS

A negative linear relationship was seen between K_{Ratio} and μ_s and between K_{Ratio} and μ_a. The absolute magnitudes of the K_{Ratio} values as a function of μ_s were clearly dependent on the associated magnitude of μ_a. Likewise, when assessing the contrast as a function of absorption coefficient, the absolute magnitude of K_{Ratio} was dependent upon the associated values of the scattering coefficient (Figures 45 & 46).
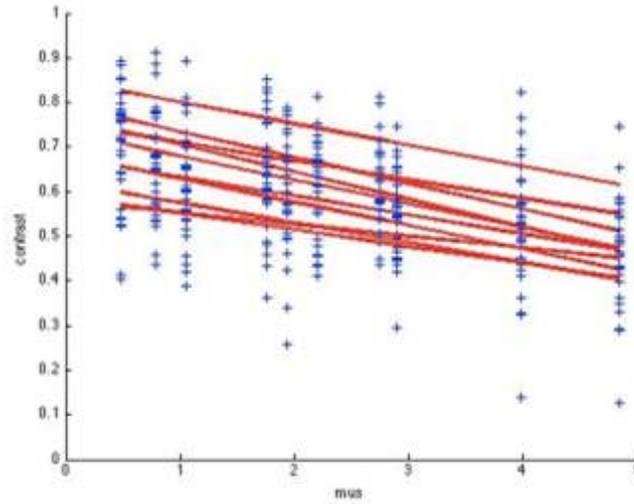
Figure 45. Relationship between contrast (K_{Ratio}) and μ_s . Each best fit line represents a single μ_a , with the largest μ_a values at the bottom. There are no significant differences between slopes. $K_{Ratio} \propto -0.0374\mu_s$.

Figure 46. Relationship between contrast (K_{Ratio}) and μ_a . Each best fit line represents a single μ_s , with the largest μ_s values at the bottom. There are no significant differences between slopes. $K_{Ratio} \propto 1.28e-3\mu_a$.

167
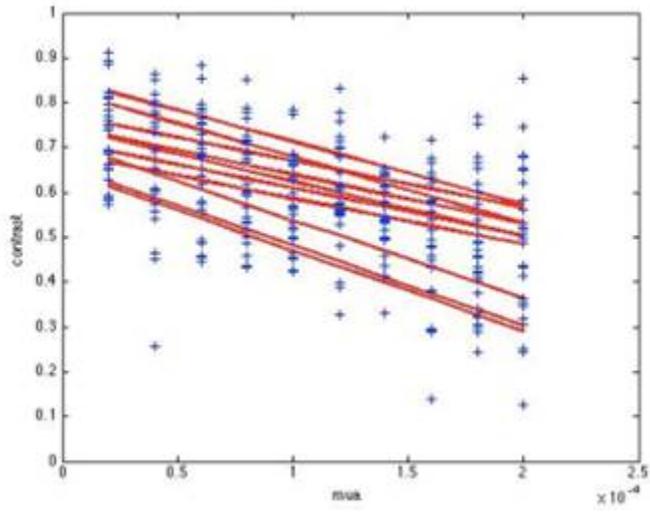
Likewise, when the effects of the total attenuation coefficient $\mu_t = \mu_s + \mu_a$ on K_{Ratio} were

evaluated, there was a significant negative relationship found (Figure 47).
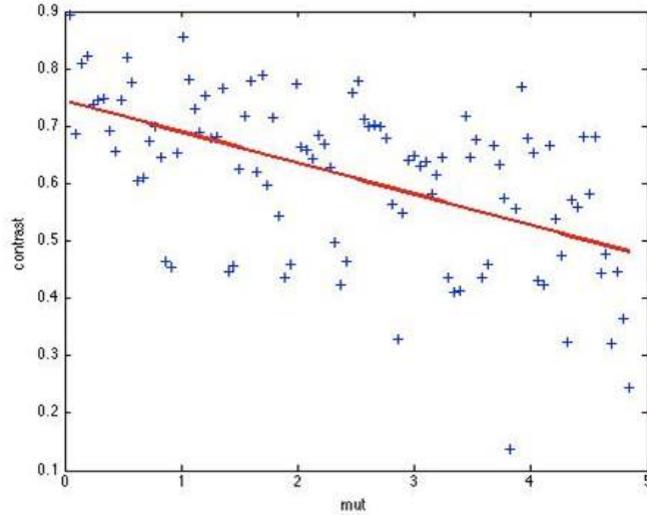
Figure 47. Effects of μ_t on K_{Ratio}. A significant negative relationship between the

variables was found. $K_{Ratio} \propto -0.0543\mu_t$.

The effect of flow velocity was also evaluated at a constant μ_s and μ_a. It was found that

$K_{Ratio} \propto -0.002v$, where v is velocity (mms^{-1}).

SUMMARY & CONCLUSIONS

The results reported here represent the first systematic evaluation of the effects of the

optical properties of the dynamic scattering medium on the contrast observed in LSCI. It

was observed that when all other experimental parameters were kept constant, contrast

decreased in a predictable fashion. On conceptual grounds, the results are not unexpected.

What was unexpected, was that the effects of μ_s on the contrast values was more

pronounced than that of velocity v. Specifically, $K_{Ratio} \propto -0.0374\mu_s$ and $K_{Ratio} \propto -0.002v$.

168

The difference in these proportionalities is on the scale of a single order of magnitude. These results imply that LSCI is more sensitive to small changes in scattering properties than it is to small changes in flow velocity. This can have significant implications when using LSCI for time course studies, for comparing different populations, and for inter-laboratory comparisons for example.

Changes in blood hematocrit result in changes in μ_s. Thus, if there is a hematocrit change during the course of a study, or between populations, this must be considered when interpreting LSCI data. When using LSCI for imaging blood flow, it is recommended that the μ_s of the blood be measured and considered as a significant variable in the data analysis.

REFERENCES

[1] Boas, D.A. and Dunn, A.K., "Laser speckle contrast imaging in biomedicine," J. Biomed. Opt. 15(1):011109 (2010).

[2] Briers, D., Duncan, D.D., Hirst, E., Kirkpatrick, S.J., Larsson, M., Steenbergen, W., Stromberg, T., Thompson, O.B., "Laser speckle contrast imaging: Theoretical and practical limitations," J. Biomed. Opt. 18(6): 066018 (2013).

[3] Duncan, D.D., and Kirkpatrick, S.J., "Can laser speckle flowmetry be made a quantitative tool?," J. Opt. Soc. Am. A 25(8), 2088-2094 (2008).

Chapter 9

(Paper 6)

Assessment of Incident Intensity on Laser Speckle Contrast Imaging Using a Nematic Liquid Crystal Spatial Light Modulator[1]

Sean J. Kirkpatrick, Kosar Khaksari, Dennis Thomas, Donald D. Duncan , "Assessment of Incident Intensity in Laser Speckle Contrast Imaging Using a Nematic Liquid Spatial Light Modulator", Journal of Biomedical Optics, 21(3), 036001(1), (2016). (See **Appendix A** for copyright transfer agreement that give permission to use this material.)

Contribution of Authors:

Mitchell A. Kirby: Ran some experiments, Developed optical layout

Sean J. Kirkpatrick: Principal Investigator, data evaluation, writing and edition

Kosar Khaksari: Ran the experiments; Developed theory, Wrote computer code, Analyzed data, Wrote manuscript

Mitchell A. Kirby, Kosar Khaksari, Sean J. Kirkpatrick[*]

*Corresponding Author: E-mail: sjkirkpa@mtu.edu

---

[1] The material contained in this chapter was previously presented in *Photonics West, SPIE*.

Michigan Technological University, Department of Biomedical Engineering, 1400 Townsend Dr., Houghton, MI, 49931 USA

Abstract. Before laser speckle contrast imaging (LSCI) can be used reliably & quantitatively in a clinical setting, there are several theoretical and practical issues that still must be addressed. In order to address some of these issues, an electro-optical system that utilizes a nematic liquid crystal spatial light modulator (SLM) to mimic LSCI experiments was assembled. The focus of this manuscript is to address the issue of how incident intensity affects LSCI results. Using the SLM-based system, we systematically adjusted incident intensity on the SLM and assessed the resulting first- and second-order statistics of the imaged speckle to explain the corresponding spatial contrast values in both frozen and time-integrated speckle patterns. The SLM-based system was used to generate speckle patterns with a controlled minimum speckle size, probability intensity distribution, and temporal decorrelation behavior. By eliminating many experimental parameters, this system is capable of serving as a useful intermediary tool between computer simulation and physical experimentation for further developing LSCI as a quantitative imaging modality.

1. INTRODUCTION

Laser speckle contrast imaging (LSCI) is a simple, non-invasive, low cost method that allows for the assessment of blood flow and perfusion in near-real time. It has become common place for LSCI and its variations to be used in full-field qualitative visualization of blood flow.[1, 2] However, there are numerous experimental challenges, as well as theoretical and practical limitations, that remain unresolved in using LSCI to make quantitative measurements of flow and perfusion.[3] Furthermore, for both quantitative and qualitative assessment of blood flows, there are compounding issues such as changes in hematocrit that manifest as changes in bulk blood optical properties that appear identical to relative changes in blood flow. Without *a priori* knowledge of the scattering and absorption coefficients of the blood, it is impossible to discriminate between changes in flow and changes in blood optical properties.[4] It is worth noting that the term perfusion is used to describe a relative motion of scatterers in blood vessels. When referring to flow, we describe a volume of scatterers. Because scatterer density has been shown to affect the measured contrast in LSCI[4], when we refer to flow and perfusion, we are implying a volume movement of scatterers in time.

In addressing experimental, theoretical and practical issues in LSCI, it is often difficult to isolate the variables under investigation due to the interdependence of the many experimental parameters. For example, flow, camera integration time, optical arrangement, laser power, and assumed flow model all interact with each other to yield a particular contrast value[3,5]. While phantom flow studies are useful, there are often issues that arise from the experimental design, such as the effects of tubing on the scattering characteristics, unanticipated fluctuations in the flow pattern, clumping of scatterers, and challenges with

reproducibility that affect the LSCI results. The challenges associated with phantom flow studies often manifest as noise in the measured contrast value, making it difficult to control single experimental variables. Additionally, computer modeling is useful in understanding the theory behind LSCI, but does not sufficiently address the challenges associated with experimental LSCI.

To address the effects of experimental settings used in LSCI, we utilize an electro-optical system employing a spatial light modulator (SLM) that can faithfully produce LSC images in a highly controlled and reproducible environment.[6] The system allows for the isolation of single experimental parameters while not varying any others. This optical system permits control of many experimental settings, namely, speckle size, decorrelation behavior of the 'scatterers' (and the resulting speckle patterns), the first-order speckle statistics of the speckle patterns (*i.e.* the intensity probability distribution), the ratio of static to dynamic scatterers, the mathematical relationship between contrast values and the assumed flow model, the camera integration time, and the frame rate. As the objective of this system is to generate dynamic speckle patterns that are statistically (and visually) similar to experimental speckle patterns observed from biological tissue, having the ability to isolate each variable independently means that we can adjust our settings to account for known interdependencies and assess unknown interdependencies between experimental parameters and measured contrast, whilst having the freedom to address other real experimental variables. For example, the speckle/pixel size ratio has been shown to have an effect on measured contrast value.[7] Our system allows us to easily adjust the speckle size to ensure that the speckle patterns are sampled spatially in any manner desired by the operator. Once the speckle size is fixed, we can then adjust experimental parameters, such

as incident intensity, and assess the effect on measured contrast values as well as the resulting effect on the frequency content of the speckle image.

LSCI is limited by the uncertainty as to the proper flow model used to describe the stochastic behavior of the scattering particles.[3] Because of this limitation, the dynamic speckle generated via reflection from the SLM is created using an assumed model. It is worth mentioning that the flow model used in mimicking speckle can be easily adjusted by the user to any model desired, which may serve as a valuable method of comparison between various models of behavior of the scattering particles in the future.

In this work, we focus on adjusting the total intensity of the speckle patterns at the imaging plane and assess the statistics of the resulting speckle patterns. In many practical applications, intensity is addressed as a laser power density incident on a phantom or tissue. When a coherent light source illuminates biological tissue, the photons transmit through, absorb, and scatter within the tissue. Because the amount of energy lost within the tissue can vary greatly between experiments, as well as tissue types in human application, the resulting backscattered light intensity arriving at the imaging plane can have varying levels of intensity. Because of this, describing the incident intensity at a medium does not sufficiently address whether or not the camera is receiving sufficient illumination. We seek to eliminate the variation seen in experimental procedures by addressing the statistical properties of the speckle patterns with varied intensities, as detected by the camera. We address the quantization of camera gray values across a wide range of incident laser power densities, presenting a guideline that can be used when adjusting both camera and laser settings in future applications of LSCI.

175

2   METHODS & MATERIALS

The optical layout can be seen in Fig. 48. A stabilized 2.5 mW HeNe laser (633nm) illuminated a 512 x 512 nematic spatial light modulator (Boulder Non-linear Systems (BNS) XY series, Model- P512) via a beam splitter that returned the scattered light to an 8-bit CMOS camera (Thorlabs, DCC1545M High Resolution USB 2.0 CMOS Camera) with an effective area of 1280 x 1024 pixels. It is assumed that only the zero-order output pattern from the BNS XY Series nematic SLM is responsible for image reconstruction due to the high zero-order diffraction efficiency of the device.[8] Additionally, BNS's high speed addressing scheme is assumed to limit phase drooping and latency, resulting in temporally stable phase modulation.[8] Before the reflected light was imaged on the CMOS array, the light passed through a $4f$ imaging system with an adjustable aperture stop located in the Fourier plane of the front lens. The lenses comprising the $4f$ imaging system consisted of a 125mm focal length (FL) achromatic triplet and a 75.0mm FL achromatic doublet. The effective focal length and principal plane of the system were estimated using thin-lens approximations.[9] The CMOS array was located in the imaging plane, approximately 132mm from the second lens. The resulting image magnification was roughly 0.5. The aperture stop was placed in the Fourier plane at a distance equal to the focal length from each lens. Varying the diameter of the aperture opening changes the minimum speckle size observed on the camera. Reducing the opening of the aperture resulted in larger speckles, while increasing the diameter resulted in smaller speckles.[10] The speckle size, d_{sp}, was estimated by Eq. 1, where λ is the illumination wavelength, v is the distance from the principal plane of the lens system to the imaging plane, and a is the diameter of the viewing lens aperture.[11]

$$d_{sp} = \frac{2.4\lambda v}{a}$$ (1)

 The light passed through a neutral density filter wheel set to attenuate incoming light, allowing adjustable incident intensity. The beam was then passed through a spatial filter consisting of a 10X microscope objective and a 25-micron pinhole. The beam was then collimated before passing through a λ/2 plate. The half-wave plate served to orient the polarization of the incoming light in the vertical plane so that the nematic SLM functioned in the phase-only mode. By operating in the phase-only mode, the light backscattered from the SLM was de-phased in the same way as if it were scattered from a rough surface or a scattering volume. A polarizer placed in the imaging arm was oriented in the same plane as the incident light. This resulted in observing only a single component of the electromagnetic wave on the CMOS array, thus generating a polarized speckle pattern. Care was taken to ensure negligible ambient light reached the CMOS array.

To generate the speckle patterns from the SLM, a sequence of phase screens, arbitrarily chosen to be 50 frames in length was loaded to the SLM. The phase screens were generated by filling a 512 x 512 array with randomly generated complex numbers of unit amplitude, with phases uniformly distributed over [0, 2π]. For each individual phase screen loaded to the SLM, a pre-determined look-up table (LUT) was used to ensure the phase modulation resulted in a linear relationship between phase distribution [0, 2π] and resulting gray values [0, 255]. Thus, light scattered from each individual SLM element was de-phased accordingly and the resulting scattered wavefront had an identical phase distribution. The scattered light remained temporally and spatially coherent, allowing for random interference to occur when the scattered light impinged on the CMOS chip of the camera, resulting in a speckle pattern.

The phase screen sequence allowed for controlled temporal decorrelation behavior. By controlling the temporal decorrelation behavior of the phase screens, the temporal decorrelation behavior of the resulting speckle patterns was varied using the copula method.[12] The correlation, r, between the speckle patterns was varied over the interval [1,-1]. For a specified correlation of $r = 1.0$ between multiple phase screens, the resulting phase screens were perfectly correlated, resulting in perfectly correlated sequential speckle patterns. When $r = 0$, the phase screens and resulting sequential speckle patterns were completely uncorrelated. Due to the complex symmetric nature of the Fourier transform relating the phase screens to speckle patterns, phase screen realizations of $r \leq 0$ result in an uncorrelated speckle pattern. The shape of the decorrelation curve was governed by the rate at which the realization was altered following either a Gaussian or exponential curve, resulting in either Gaussian or Lorentzian decorrelation behavior in the imaged speckle. When generating the phase screens, we invoke the Wiener-Khinchin theorem[13] to recall that an exponential and a Lorentzian form a Fourier pair, as does a Gaussian and a Gaussian. That is, when the phase screens exhibited a Gaussian decorrelation behavior, the resulting speckle pattern sequence also exhibited Gaussian behavior. When the phase screens exhibited an exponential decorrelation behavior, the speckle sequence exhibited Lorentzian behavior. In the present work, the decorrelation time of the generated speckle frames was arbitrarily chosen to be 17 ('fast') and 37 ('slow') frames. An example of Gaussian phase screen decorrelation behavior, showing varying decorrelation times, can be seen in Fig. 49. Fig. 49 also demonstrates the ability to change the shape of the autocorrelation function between Gaussian and Lorentzian.

Once the phase screens were generated and loaded to the SLM, each resulting

178

speckle pattern was imaged individually by the CMOS camera. The camera was set to expose each static speckle pattern for 35ms. An example showing a single phase screen and the resulting imaged speckle pattern can be seen in Fig. 50. Using the imaged speckle patterns generated by the SLM, the first-order statistics of the coherent summation were assessed and described by the intensity probability distribution function (PDF). A comparison of the theoretical and experimental PDF for fully polarized speckle is displayed in Fig. 51. For a polarized speckle pattern, the theoretical PDF is a negative exponential.[10] Fig. 51 (a) demonstrates the ability to reproduce a single speckle pattern with a negative exponential PDF. In cases where multiple speckle patterns are incoherently summed, the PDF of the resultant speckle pattern is described by a Rayleigh distribution. In practice, such a speckle pattern can also be seen when observing speckle from a volume scatterer, such as tissue, without using a polarizer to isolate a single component of the electromagnetic field. Fig. 51 (b) demonstrates the system's ability to reproduce speckle with a Rayleigh PDF, by summing on an intensity basis, multiple individual polarized speckle patterns. The number of speckle patterns that need to be summed to generate a speckle pattern with a Rayleigh PDF, as in Fig. 51 (b), depends upon the decorrelation behavior of the speckle sequence. The lower the correlation between subsequent speckle patterns, the fewer individual patterns need to be summed. In the limiting case, only 2 speckle patterns are necessary if they are statistically independent from one another.[10]

The second-order statistics of the interference patterns were analyzed through the power spectral density (PSD) of the imaged speckle pattern. As the calculated PSD can be used to experimentally determine speckle size, we use the calculated speckle size to describe the second-order behavior of the generated speckle patterns. To control the

minimum size of the speckle, and thus the second-order characteristics, the camera aperture can be easily adjusted to verify the minimum speckle size in the imaged speckle, the power spectral density (PSD) of the imaged speckle was calculated and the diameter of the frequency energy band was measured (in pixels). The size of the minimum imaged speckle was calculated as[7]

$$\text{Speckle size} = 2\left(\frac{\text{Width of Array}}{\text{Diameter of PSD Energy Band}}\right) \tag{2}$$

Fig. 52 demonstrates the variation in speckle size achieved with the SLM-based system. The speckle size for both the experimental and calculated values are displayed relative to the pixel size of the CMOS array. Fig. 52 (a) displays a single speckle pattern from the SLM and its power spectrum (Fig. 52 (b)), which was used to estimate the minimum speckle size in the pattern. Fig. 52 (c) displays the theoretical speckle size, as calculated with Eq. 1, plotted with the imaged speckle size. For the experiments across varied intensities, the minimum imaged speckle size relative to the CMOS chip pixel size (5.2 μm) was kept constant at roughly 3.25 pixels/speckle.

To generate an LSC image, multiple sequential frames of speckle patterns imaged by the CMOS array were summed to simulate speckle blurring, as seen when dynamic speckle is imaged with a finite exposure time. The blurred speckle results in reduced contrast seen in temporal averaging. Contrast, K, was defined as

$$K(r) = \frac{\langle \sigma_i \rangle}{\langle \mu_i \rangle} \tag{3}$$

where μ_i is the mean intensity and σ_i is the standard deviation of the intensity of a 7 x7

window of pixels slid across the image at location r r.[1] For a single, static, polarized speckle pattern, the global contrast attains a theoretical maximum of unity. For time averaged, dynamic speckle patterns the global contrast is less than unity. It should be noted, however, that these global contrast values have their own log-normal statistical distributions.[14] Because the speckle decorrelation behavior can be altered in different pixel regions of the phase screens, the speckle patterns generated by the SLM are capable of displaying spatially-dependent decorrelation behavior. Thus regions of 'fast' decorrelation and 'slow' decorrelation can be created to mimic an LSCI image of a vessel with rapidly moving scatterers ('fast' decorrelation) surrounded by slower moving spatial regions. To demonstrate the ability to simulate a LSCI image with a 'vessel' region with motion in the center, a 200-pixel section of rows was set to decorrelate 16 times faster (τ_{c2}) than the more slowly varying speckles from the surrounding 'tissue' region, (τ_{c1}), i.e. $\tau_{c2} = 16\tau_{c1}$, as displayed in Fig. 53.

In LSCI, the link between speckle contrast and flow can only be made if the flow distribution is known. However, the actual flow distribution of biological fluid is often unknown. Early work has assumed the flow of blood to exhibit either purely unordered (Lorentzian) or ordered (Gaussian) flow.[2,15,16] Theoretically, a Lorentzian velocity distribution is only appropriate for Brownian motion (purely random flow). Conversely, a Gaussian velocity distribution is technically only appropriate for purely ordered flow. In practical situations, it is likely that the true flow model is a mixture between the Lorentzian and Gaussian line shapes. In laser engineering terms, the convolution between these two line shapes is a Voigt profile, frequently referred to as a rigid-body model.[3] Because assumptions are made to describe the fluid velocity distribution, the unambiguous

quantification of flow velocity from contrast values is not yet possible. To model the fluid velocity distribution with this system, in addition to controlling the temporal decorrelation rate of the speckle images, we produce speckle sequences that decorrelate following a user defined function. We demonstrate this by producing speckle sequences that result in calculated contrast values that follow both Gaussian and Lorentzian distributions.[1] However, it should be noted that any desired function can be used to mimic whatever flow model is desired. The experimental contrast values were compared to the theoretical values as a function of the ratio of the speckle decorrelation time, τ_c, and the integration time, T. Here, the speckle decorrelation time, τ_c was predetermined by the realization number of the generated phase screens, and the integration time, T, was determined by the number of summed frames. The results are shown in Fig. 54, which displays a comparison of theoretical and experimental results. For the experiments with varied intensity, 30 phase screens assuming a Gaussian decorrelation pattern were summed to ensure the LSC images were sampled and summed to appropriately mimic contrast values seen when imaging experimental dynamic speckle with a finite exposure time.

To adjust the intensity of the interference pattern, a neutral density (ND) filter wheel covering 2-orders of magnitude was placed in front of the 2.5mW stabilized HeNe laser used in these experiments. A photo-detector was placed in the imaging plane to calibrate the intensity of the light at the CMOS array for each filter value prior to image acquisition. The intensity calibration curve can be seen in Fig. 55. This calibration curve was used to relate the speckle contrast to a relative reduction of laser power density at the imaging plane. This approach serves as an attempt to generalize the results so that they

may be applied to an array of LSCI applications where the scattering and absorption of light by tissue may result in backscattered light with varied intensities.

To address the effects of over- and under-exposing speckle during image acquisition, the exact same phase screens were loaded to the SLM and the resulting speckle patterns were imaged in the same sequence at each intensity value. The statistical behavior of a single 'frozen' speckle pattern was assessed and then the contrast from the incoherent sum of 30 images was calculated. This summation of 30 images mimics a finite exposure time as would be used in an actual LSCI application.

Herein, we describe the effects of light intensity on sensitivity to changes in spatial decorrelation between 'flow' and 'static' regions. The ratio between the contrasts in the two regions is calculated in dB as:

$$K_{ratio} = 20\log_{10}\left(\frac{K_{static}}{K_{flow}}\right) \tag{4}$$

K_{static} was calculated in a 200 x 100 pixel area in the τ_{c1} region, while K_{flow} was calculated from a 200 x 100 pixel area in the faster decorrelating, τ_{c2} region.

3   Results

An example of the same imaged 'frozen' speckle pattern sampled at varying intensities can be seen in Fig. 56. The global spatial contrast of this speckle pattern, as calculated by Eq. 3, is shown across the full range of intensities investigated in Fig. 57 (a), with the global intensity mean and spatial standard deviations used to calculate contrast plotted in Fig. 57 (b). In the frozen speckle images where the mean intensity is approximately equal to the standard deviation (in the intensity range from $6.05\mu W/cm^2$- $.605\mu W/cm^2$, 10%-1% of full

intensity), the resulting contrast is close to the theoretical value of unity. The global contrast was closest to unity when the mean intensity value fell between grayscale values of 10 to 73 (recall that an 8-bit CMOS chip was used in these experiments). In practice, the contrast is rarely equal to the exact theoretical value of 1.0 due to mechanical vibrations, dark current noise in the system, and the fact that calculated global contrast values display an intrinsic log-normal distribution.[17]

The effects of incident intensity on the sampled first-order statistics of the individual speckle patterns were also investigated. Note that the random phase screens used to generate the speckle patterns had a phase modulation of [0, 2π]. Thus, since a single polarization state was observed, the speckle patterns produced from these phase screens should exhibit a negative exponential intensity PDF. The first order statistics (PDFs) seen in the camera quantization of the speckle at the intensity extremes displayed deviation from the negative exponential in both the calculated PDF and in the camera intensity histogram, as seen in Fig. 58. The histograms show that high incident intensity results in pixel saturation while low intensities cover a smaller range of gray values. The highest contrast values were seen in the cases where both the calculated PDF and quantized intensities (histogram data) follow the theoretical negative exponential.

The resulting spatial contrast analysis, following the summation of the 30-image sequences at varied intensities, is displayed in Fig. 59. The 200-pixel band in the center of the image displayed rapid blurring of the speckles, thus reducing contrast, as expected due to the smaller τ_{c2}. In this set of images, it is clear that there is an intensity range that results in optimal discrimination between the rapidly and slowly decorrelating regions. To quantitatively assess this, the contrast values of both the simulated 'static' and 'flow'

regions were plotted in Fig. 60. The intensity values that resulted in a near theoretically ideal PDF in the 'frozen' speckle patterns (1%-10%) showed the highest contrast ratio between 'static' and 'flow' regions when the respective speckle patterns were summed. Within this range of intensities, the 'frozen' speckle pattern exhibits a global contrast near unity. Outside of this range, the contrast values in the 'dynamic' speckle vary and sensitivity to speckle motion becomes reduced.

By assessing the width of the power spectral density (PSD) of the individual speckle patterns, the frequency content of the images can be assessed. For an appropriately (spatially) sampled speckle image, with no saturation or significant under-exposure, the frequency content is a means of estimating the minimum speckle size in the speckle image (*i.e.,* second order statistics). Since the minimum speckle size was set during the course of the experiments by the diameter of the aperture in the imaging arm, we were able to use this *a priori* information to investigate the effects of image saturation on the frequency content of the speckle images. An intensity trace was plotted across the PSD and the full width half max (FWHM) was estimated to get the width of the PSD, and thereby address the effects of saturation on the frequency content of the speckle images. The 'apparent' imaged speckle size, artificially created by the loss of high frequency content, was calculated by taking the FWHM of the PSD and dividing the result by 2 (because DC is located in the center of the display) so the values used align with the theoretical calculation of speckle size seen in Eq 1. The experimentally determined 'apparent' speckle size was then normalized relative to the camera pixel size and displayed in Fig. 61. A loss of high frequency data was seen in speckle patterns imaged with greater than 10% of full intensity. This result indicates that there may be pixel saturation at higher intensities[18].

In many applications of LSCI, raw speckle images are subject to histogram equalization so as to fill the full dynamic range prior to processing.[19, 20, 21] This scaling effect often adjusts the mean contrast in the single speckle pattern, and is thought to improve an under-exposed image. To assess whether the simple histogram equalization results in improved contrast, the gray values of each imaged speckle pattern summed in the spatial contrast analysis of 'dynamic' speckle were scaled to fill the full dynamic range of the camera. Another approach would be to employ a higher bit-camera and bin multiple intensity values so as to reduce the number of gray levels. However, the goal of this simple analysis is to briefly display that although single "frozen" speckle look better post equalization, the actual image quality is not improved. For this investigation, the exact same speckle patterns were adjusted to ensure the only altered variable was the scaling function. The spatial contrast analysis on the scaled images resulted in an almost identical range of optimal values as a function of intensity. A comparison of scaled and unscaled contrast values can be seen in Fig. 62. Fig. 62 also displays an example of the scaled histogram data from a speckle pattern at a very low intensity (.03% of full intensity). The resulting measured contrast values following the histogram equalization were nearly identical to the contrast values of the unscaled speckle patterns in the resulting spatial contrast analysis. The results indicate that simple histogram equalization does not significantly improve speckle statistics and sensitivity to flow at low intensities.

4   Conclusions

The results of our experiments indicate that there is a range of incident intensities that approach the theoretically ideal PDF for fully developed speckle. This in turn

corresponds to a global contrast approaching unity. When the single speckle patterns displayed characteristics near the theoretically ideal values, the resulting spatial contrast analysis from a summation of speckle patterns displayed a high sensitivity to motion. The results indicate the importance of assessing the quantized signal and resulting intensity PDF of the speckle patterns during image acquisition in LSCI. The optimum sensitivity of the LSC image is seen when the speckle frames have appropriate intensity distribution to display the first-order statistics of fully developed speckle.

It is clear that at high intensities, high frequency information is lost due to camera saturation, resulting in a decrease in contrast. In cases of high incident intensity, it has been proposed that intensity peaks are clipped in the quantization process of the camera.[18] When the average intensity of the raw speckle image is less than half the maximum intensity value of the sensor, clipping of the intensity peaks is assumed to have a reduced effect. For an 8-bit camera with $2^8 = 256$ different gray values, Alexander $et\ al.$[18] proposed that the maximum average intensity value should be 128 to avoid clipping of high frequency data. That is, the maximum average gray level should be no more than 128 in order to avoid saturation and the loss of the ability to resolve individual speckles. Our results support this claim. At higher intensities, the imaged speckle displayed decrease in high frequency content due to pixel saturation. When the average intensity gray value was above 125 (>16% of the full intensity), we also saw a reduction in statistical variance that resulted in contrast values diverging from the theoretical maximum. It is also worth noting that detecting the number of saturated pixels in the image, prior to spatial contrast analysis, could serve as a method to determine if the camera is over-saturated. Others have indicated that increased intensity improves detectability of changes to flow,[22] however, our results

indicate that there is a window of laser power densities that result in optimum sensitivity. In practice, the upper range of incident light intensity is limited by the laser power density at which a coherent light source will backscatter without inducing functional changes in the tissue due to global absorption. In other words, the laser power density where functional changes occur in the tissue is the limiting factor in determining a maximum incident intensity. At this maximum incident intensity, a combination of reducing the imaging aperture diameter and shortening the camera integration time can be used to prevent saturation.

Simply scaling to fill the full dynamic range using an 8-bit camera improved the mean intensity when the images were under-exposed, but did not correct for the loss of data due to the digital quantization process. Even though this process improved the mean intensity value, the standard deviation changed at relatively the same rate, resulting in little to no improvement in calculated contrast. If the gray values of under-exposed images are quantized by a lower bit system, small variances in the shades of gray may be binned to the same gray value, resulting in a loss of information. Simple histogram equalization does not improve contrast data in a situation where sampling results in information loss. However, there may be reason to further explore methods of pre-processing speckle data so as to improve the statistics of poorly-sampled data. There have been proposed methods to solve the issue of uneven illumination that may be applied to improve the contrast of under-exposed images used in LSCI. [23, 24, 25] It can also be reasoned that increased camera bit-depth may result in fully developed speckle characteristics and optimum sensitivity across a wider range of incident intensity values.[23] In practice, however, adjusting the

incident intensity and camera settings may be sufficient to ensure optimal speckle statistics are satisfied when sampling speckle data for LSCI.

We have shown the ability of our system to faithfully reproduce the speckle images used in LSC imaging and its promise as a research tool. Because our electro-optical system allows for fast experimentation and reproduction, this system provides a convenient and quantifiable platform to address many of the real-world complications that hinder the on-going development of LSCI, such as incident intensity in experimental settings. It is hoped that through approaches similar to that employed herein, the fine details of LSCI can be explored in more detail and further development of the imaging modality as a reliable and inexpensive research and diagnostic tool can proceed.

5. Acknowledgements

References

[1] Boas, D.A. and Dunn, A.K., "Laser speckle contrast imaging in biomedicine," J. Biomed. Opt. 15(1):011109 (2010).

[2] Briers, D., Duncan, D.D., Hirst, E., Kirkpatrick, S.J., Larsson, M., Steenbergen, W., Stromberg, T., Thompson, O.B., "Laser speckle contrast imaging: Theoretical and practical limitations," J. Biomed. Opt. 18(6): 066018 (2013).

[3] Duncan, D.D., and Kirkpatrick, S.J., "Can laser speckle flowmetry be made a quantitative tool?," J. Opt. Soc. Am. A 25(8), 2088-2094 (2008).

[4] K. Khaksari, S.J. Kirkpatrick, "Effects of combined scattering and absorption coefficients on laser speckle contrast imaging values", Proc. SPIE 9322, Dynamics and Fluctuations in Biomedical Photonics XII, 93220U-1-4 (March 5, 2015).

[5] Song, Lipei, and Daniel S. Elson. "Effect of signal intensity and camera quantization on laser speckle contrast analysis." *Biomedical optics express* 4.1 (2013): 89-104.

[6] Kirby, M. A., Khaksari, K., & Kirkpatrick, S. J. (2015). *Nematic liquid crystal spatial light modulator for mimicking laser speckle contrast imaging.* Paper presented at the SPIE BiOS.

[7] Kirkpatrick, Sean J., Donald D. Duncan, and Elaine M. Wells-Gray. "Detrimental effects of speckle-pixel size matching in laser speckle contrast imaging." *Optics letters* 33.24 (2008): 2886-2888.

[8] http://bnonlinear.com/pdf/XYSeriesDS0909.pdf

[9] Hecht, Eugene. "Geometrical optics." *Chapter* 5 (1988): 149-242.

[10] J. W. Goodman, *Speckle Phenomena in Optics* (Roberts & Co., Englewood, CO, USA 2007).

[11] Jones, Robert, and Catherine Wykes. *Holographic and speckle interferometry*. Vol. 6. Cambridge university press, 1989.

[12] Duncan & Kirkpatrick, "The copula, a tool for simulating speckle dynamics," J. Opt. Soc. Am. A 25 , 231-237, 2008

[13] J. W. Goodman, *Statistical Optics* (Wiley, New York, NY, USA, 2000).

[14] Duncan, Donald D., Sean J. Kirkpatrick, and Ruikang K. Wang. "Statistics of local speckle contrast." *JOSA A* 25.1 (2008): 9-15.

[15] A. F. Fercher and J. D. Briers, *Opt. Commun*. **37**, 5:326–330 (1981).

[16] J. D. Briers and S. Webster*, J. Biomed. Opt*. **1**, 2:174–179 (1996).

[17] Bandyopadhyay, Ranjini, et al. "Speckle-visibility spectroscopy: A tool to study time-varying dynamics." *Review of Scientific Instruments* 76.9 (2005): 093110.

[18] Alexander, Terri L., James E. Harvey, and Arthur R. Weeks. "Average speckle size as a function of intensity threshold level: comparison of experimental measurements with theory." *Applied optics* 33.35 (1994): 8240-8250.

[19] Richards, Lisa M., et al. "Low-cost laser speckle contrast imaging of blood flow using a webcam." *Biomedical optics express* 4.10 (2013): 2269-2283.

[20] Yang, Owen, and Bernard Choi. "Laser speckle imaging using a consumer-grade color camera." *Optics letters* 37.19 (2012): 3957-3959.

[21] Richards, Lisa M., et al. "Low-cost laser speckle contrast imaging of blood flow using a webcam." *Biomedical optics express* 4.10 (2013): 2269-2283.

[22] D.D. Postnov et. al. "Improved detectability of microcirculatory dynamics by laser speckle flowmetry" JBiophotonics

[23] Song, Lipei, and Daniel S. Elson. "Effect of signal intensity and camera quantization on laser speckle contrast analysis." *Biomedical optics express* 4.1 (2013): 89-104.

[24] Zhang, Hongyan, et al. "Correcting the detrimental effects of nonuniform intensity distribution on fiber-transmitting laser speckle imaging of blood flow."*Optics express* 20.1 (2012): 508-517.

[25] Shanmugavadivu, P., K. Balasubramanian, and K. Somasundaram. "Modified Histogram Equalization for Image Contrast Enhancement using Particle Swarm Optimization." *Int. J. of Comp. Sci., Engg. and IT* 1.5 (2011): 13-27.

Figures
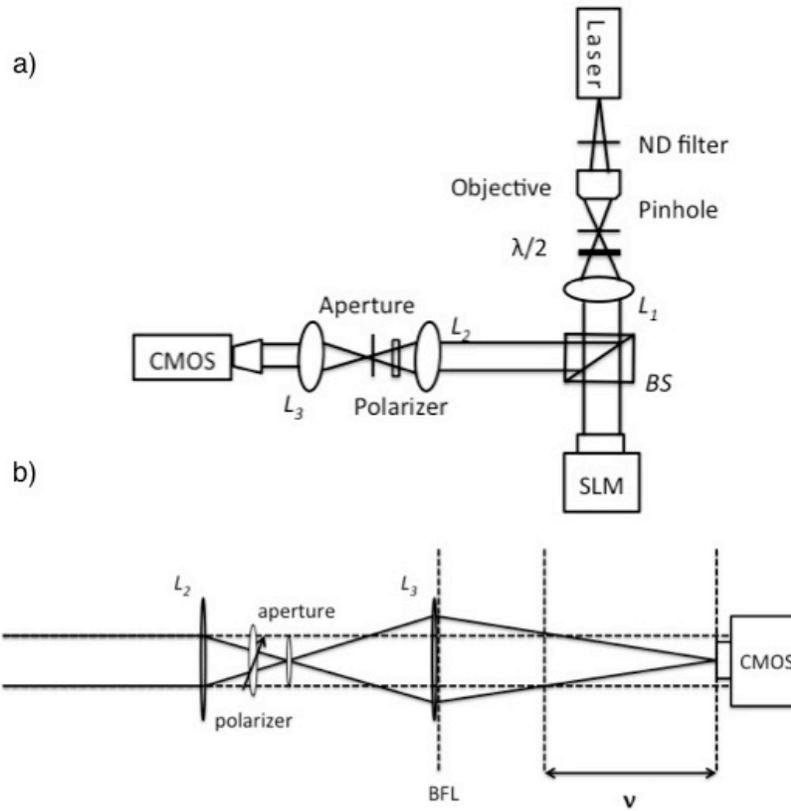
Fig. 48. a) Optical layout of the LSCI simulating system. The laser was a 2.5mW stabilized HeNe (633nm). The focal length of L_1, L_2, and L_3 are 75mm, 125mm, and 75mm, respectively. The image magnification equaled ~ 0.5. b) Horizontal view of the imaging arm of the set-up. The distance from L_2 to L_3 was ~300mm. The CMOS array was located ~132mm from the back focal plane (BFL) of L_3. The principal plane, v, was estimated to be ~37.5mm from the CMOS array.
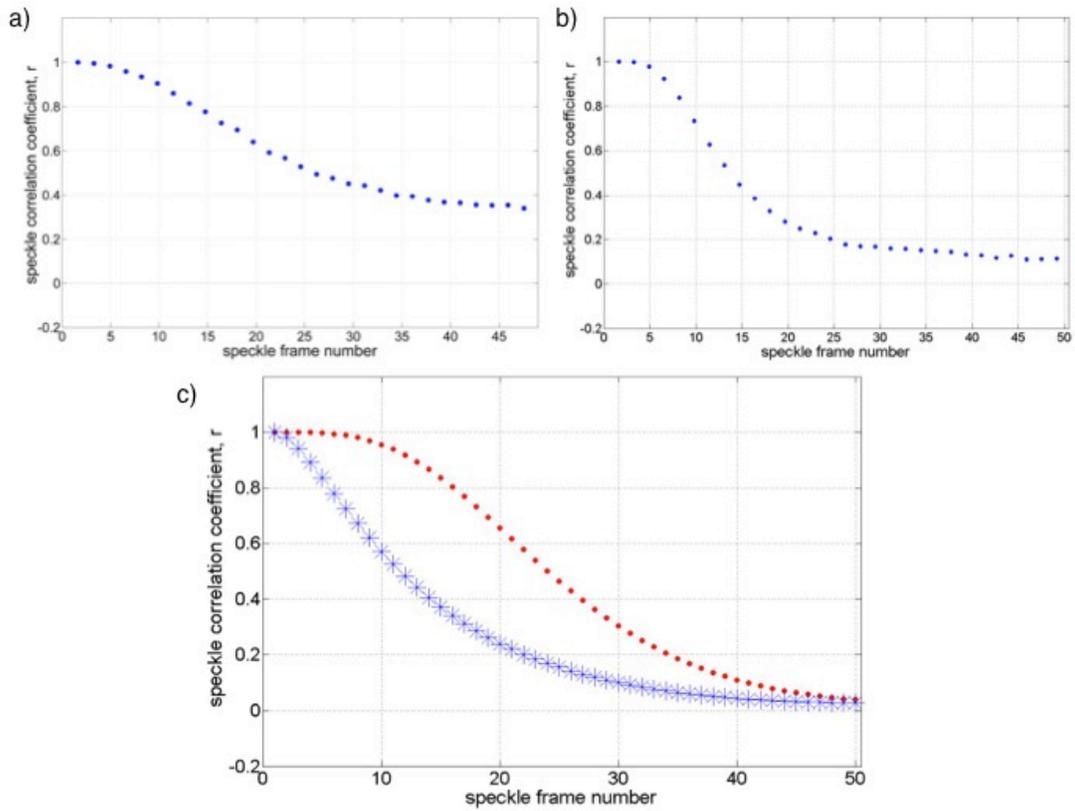
Fig 49. Decorrelation curve for SLM speckle patterns with different correlation behavior exhibiting a Gaussian decorrelation profile. For this example, 50 screens were created to image 50 consecutive speckle patterns. (a) Decorrelation of 37 frames, (b) Decorrelation of 17 frames, (c) Demonstration of both Lorentzian and Gaussian decorrelation behaviors showing a Lorentzian autocorrelation function plotted along with a Gaussian autocorrelation function.
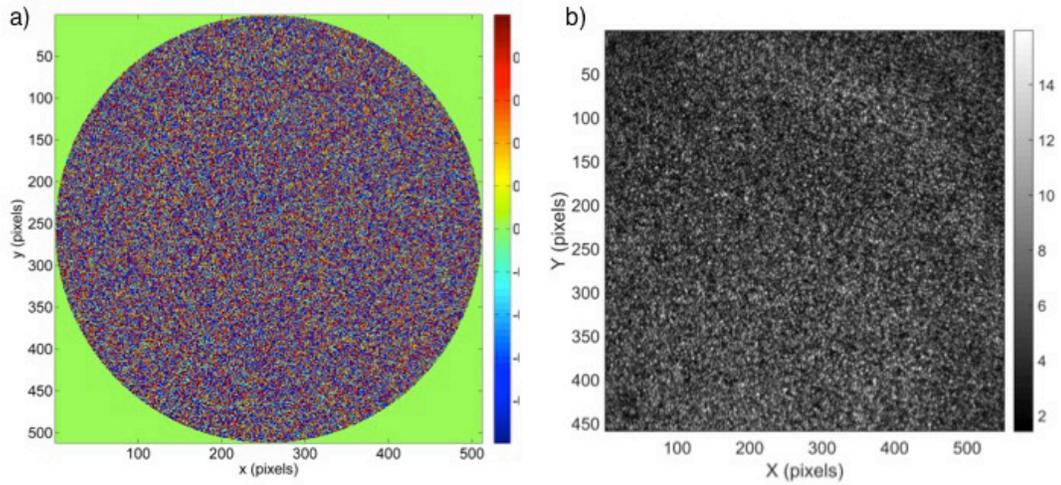
Fig. 50. (a) Phase screen loaded to the SLM. The pixel-phases were evenly distributed and randomly generated between [0,2π]. The pixel values are displayed using a RGB color map with 64 discrete values. (b) The resulting speckle pattern imaged with an 8-bit CMOS camera. The random interference can be seen mapped to gray values between [0,255], with a value of 255 indicating purely constructive interference, and 0 resulting from destructive interference.
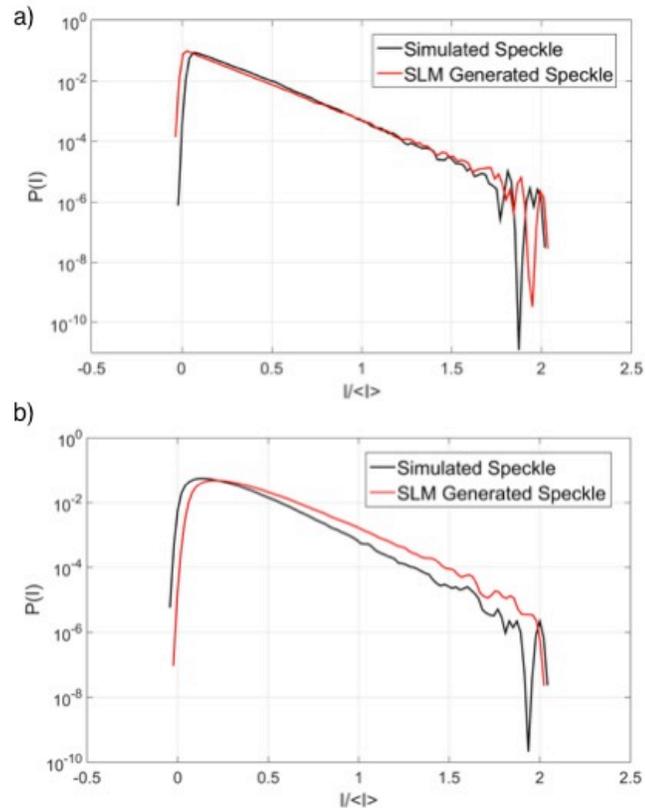
Fig. 51. Intensity PDF's of SLM generated speckle patterns plotted with numerically simulated (theoretically ideal) speckle patterns. (a) Fully developed, polarized intensity PDF showing both experimental (SLM) and theoretical speckle patterns in agreement. (b) Non-polarized intensity PDF showing both experimental and theoretical results in agreement. It is worth noting that the Rayleigh PDF is often dependent on the scale factor used. For this experiment, the logarithmic scale shows similar linearity to assume an accurate intensity distribution.
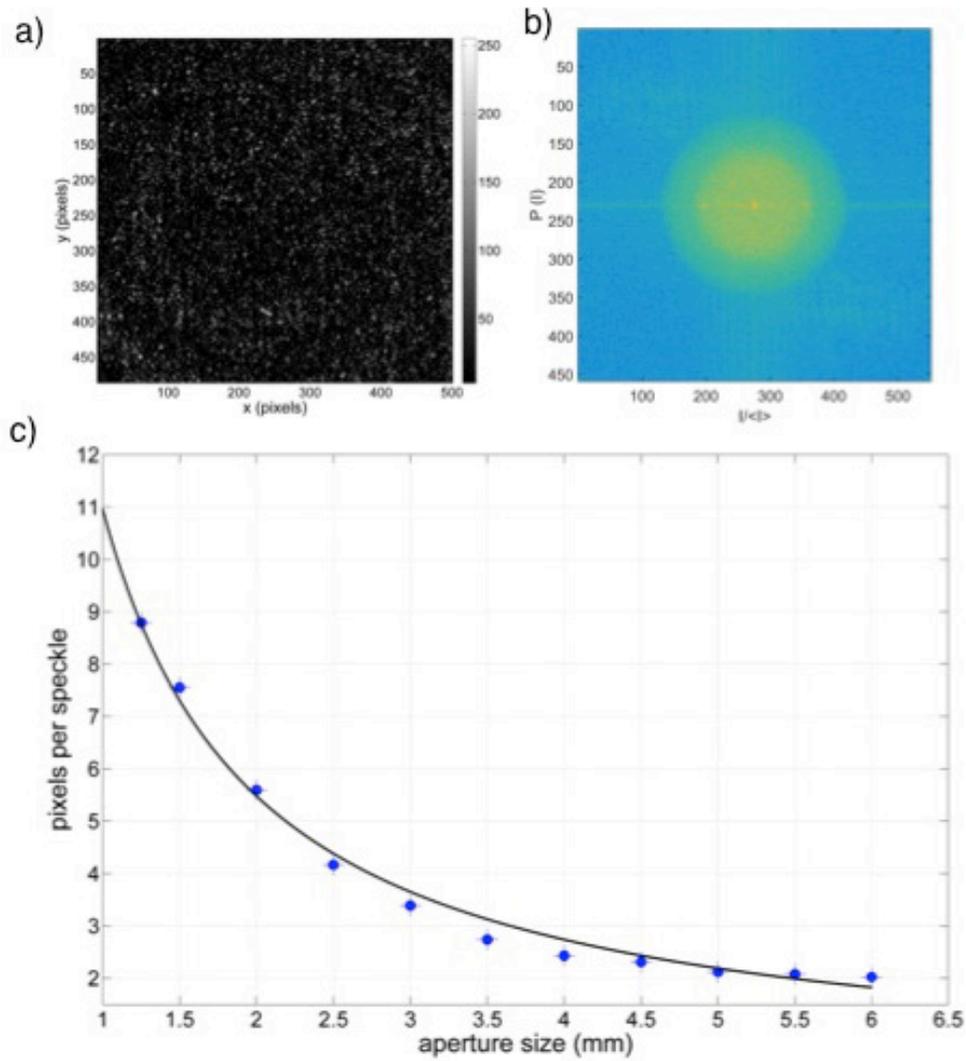
Fig 52. (a) SLM generated speckle pattern (b) SLM generated speckle PSD. The minimum speckle size in this case was 4 pixels. (c) Variation in speckle size plotted as a function of the aperture diameter, with the theoretical curve of Eq. 1 plotted as the solid line. The experimentally sampled speckle size is plotted as a blue dot.
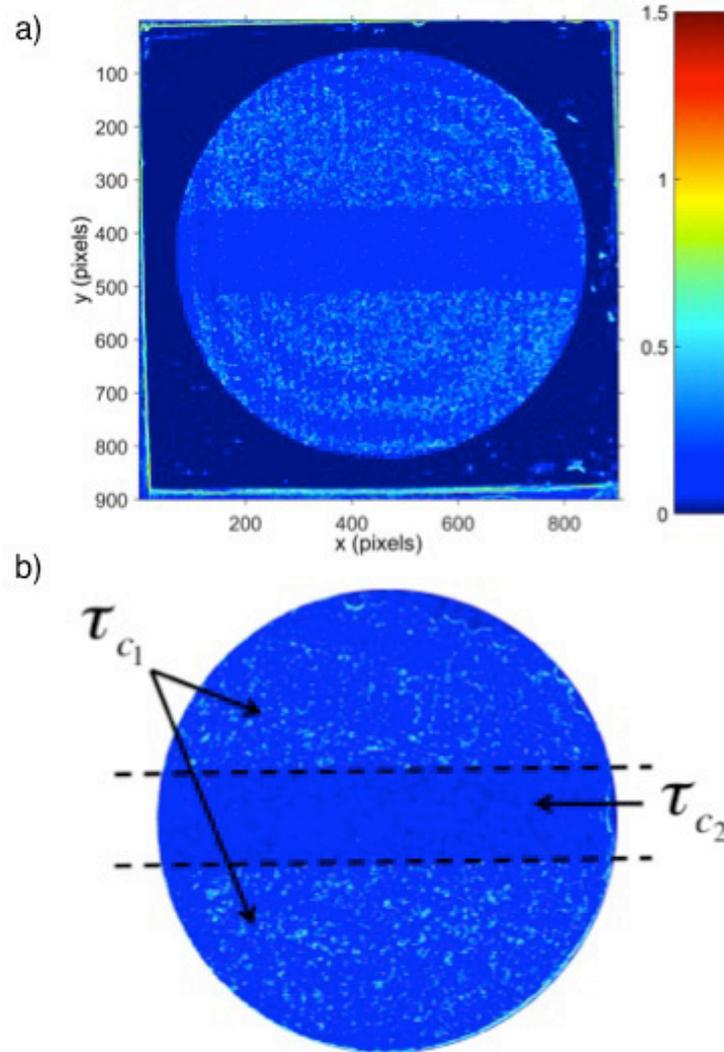
Fig 53. Simulated LSC image. The center region represents the 'flow' region (τ_{c_2}). The contrast ratio between the static (τ_{c_1}) and dynamic region was 4.108dB. In this figure, the contrast range was set between [0,1.5]. The nearly concentric rings come from noise in the optical layout of the system.
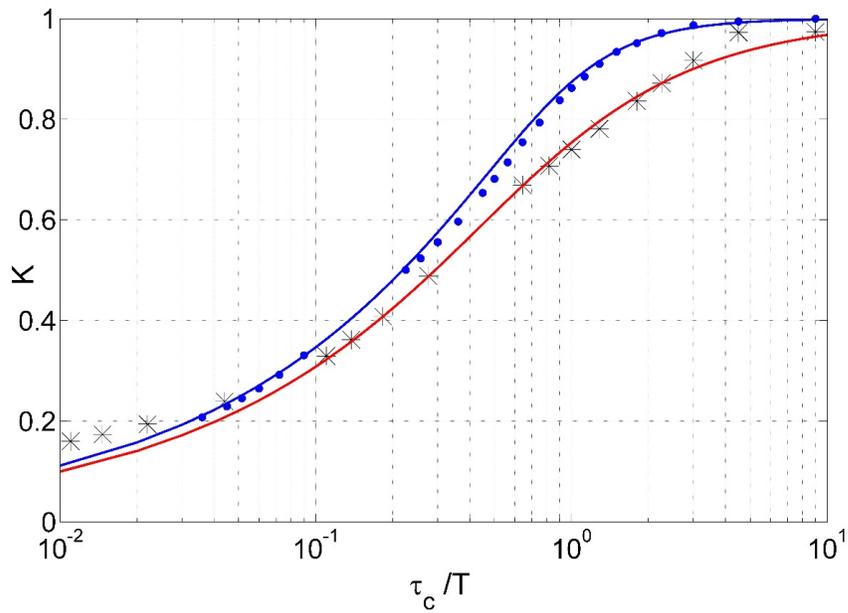
Fig 54. SLM simulated contrast vs $\frac{\tau_c}{T}$ for both a Gaussian and Lorentzian velocity

distribution. The SLM set-up was able to faithfully reproduce the expected results for

both flow models.
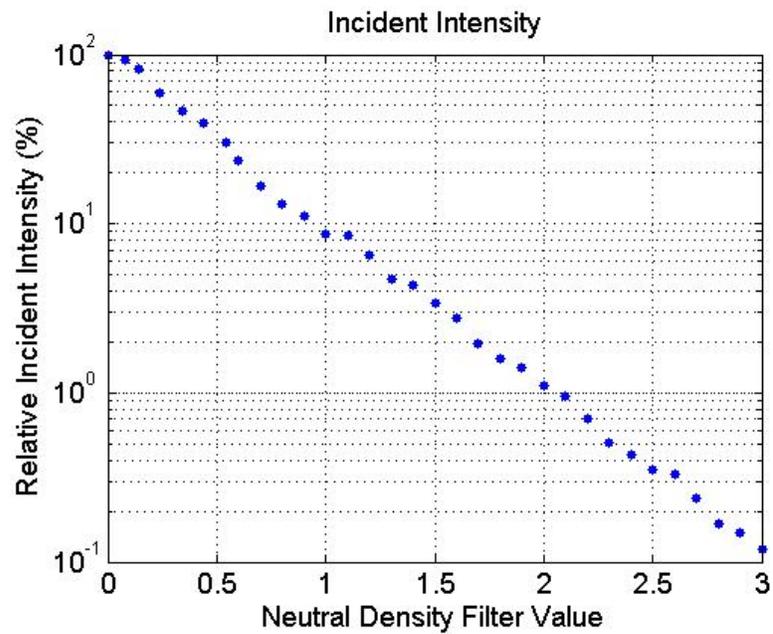
Fig 55. Relation between ND filter and average intensity at CMOS array. The intensity

was reduced logarithmically from the full intensity of .0605mW/cm^2.
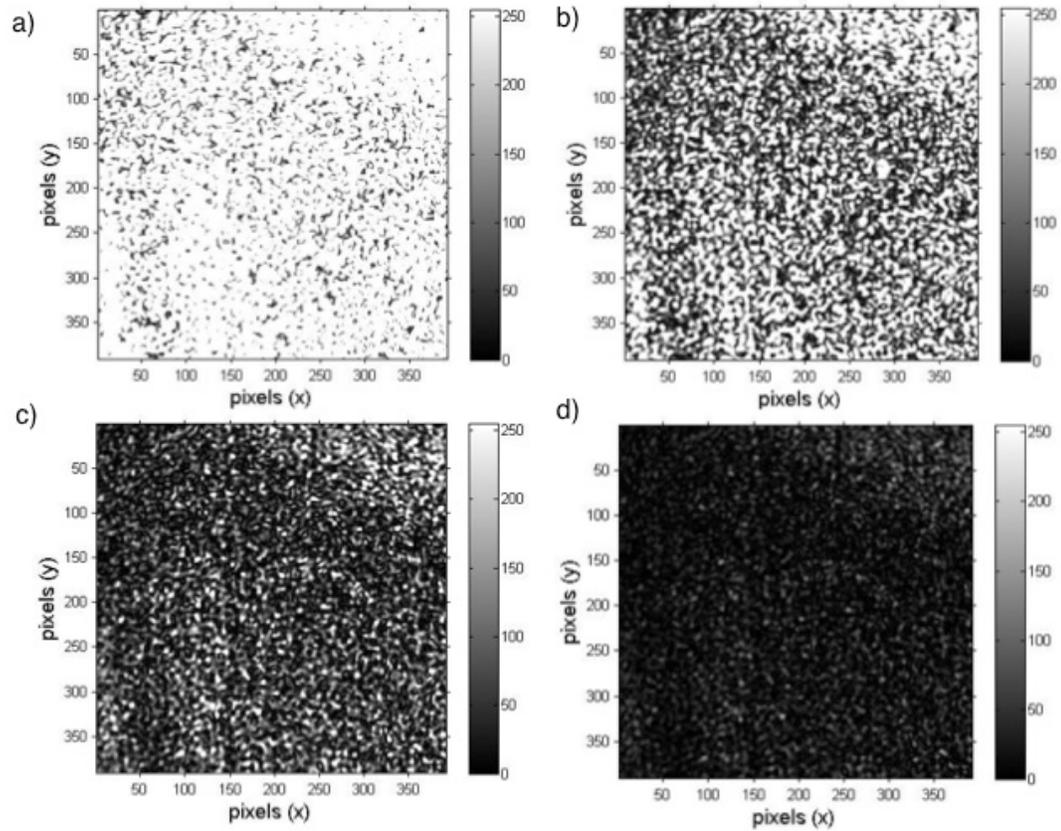
Fig 56. "Frozen" speckle patterns at (a) 100%, (b) 30%, (c) 8.75%, and (d) 3.4%, of full

intensity (.0605mW/cm^2).
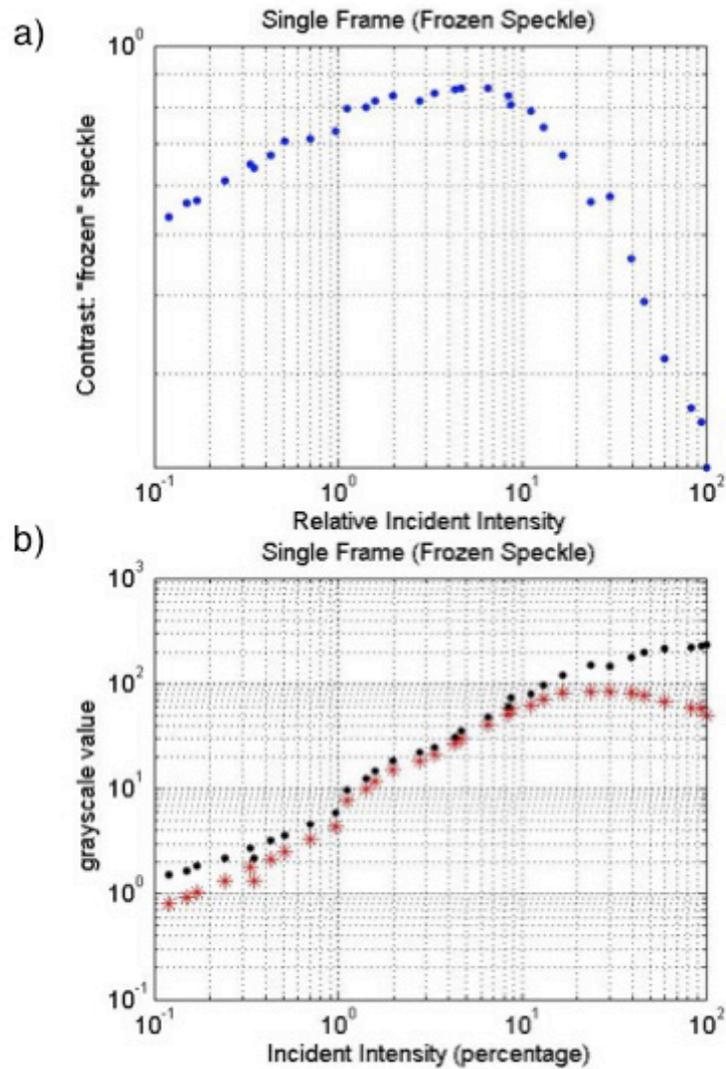
Fig 57. (a) Contrast in a single speckle frame. In the case where a large field is used, such as a global contrast, the theoretical limit of K=1 can be assumed as the "ideal."[11] Note the range where global contrast approaches unity. (b) The global mean intensity (black dot) and spatial standard deviation (red star) used to calculate contrast of a single speckle pattern.

(a)

(b)

201

(c)

(d)

(e)

(f)

203
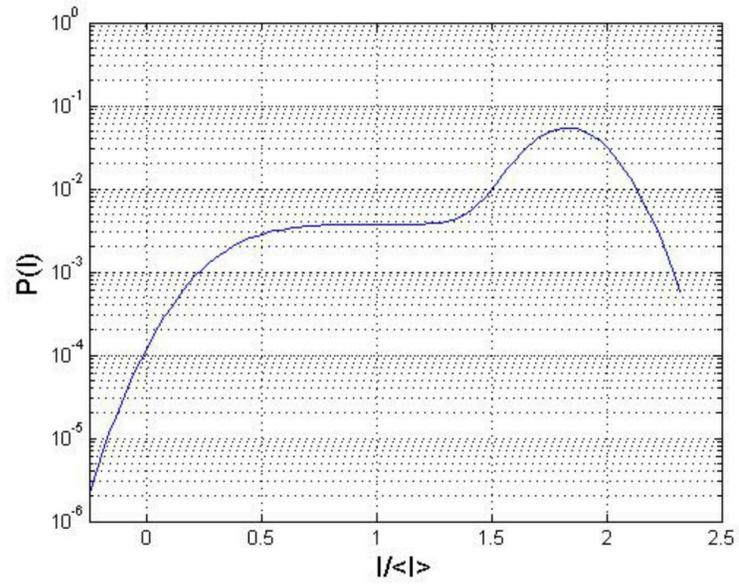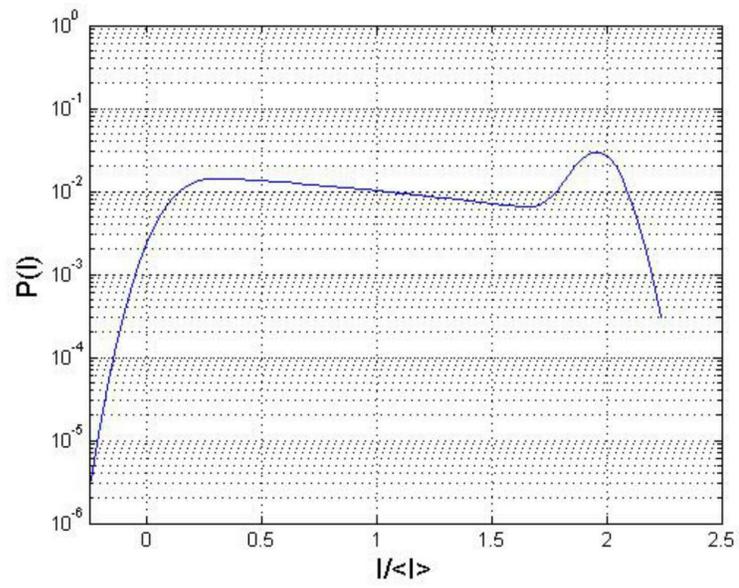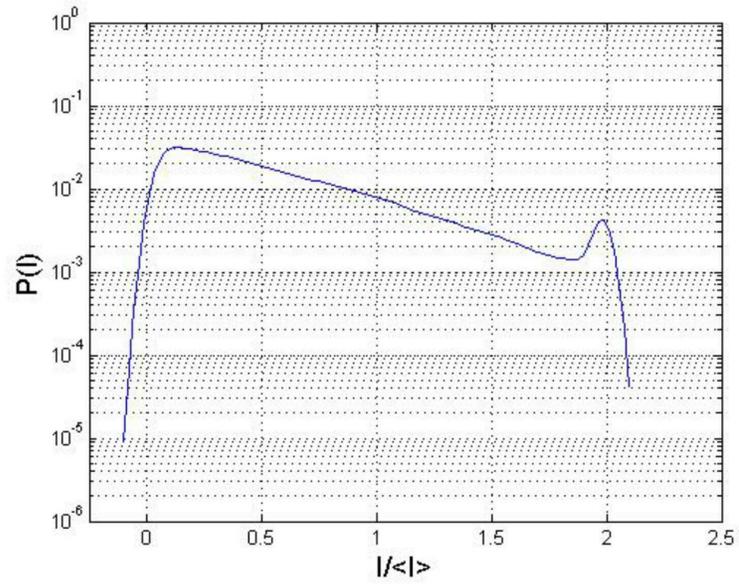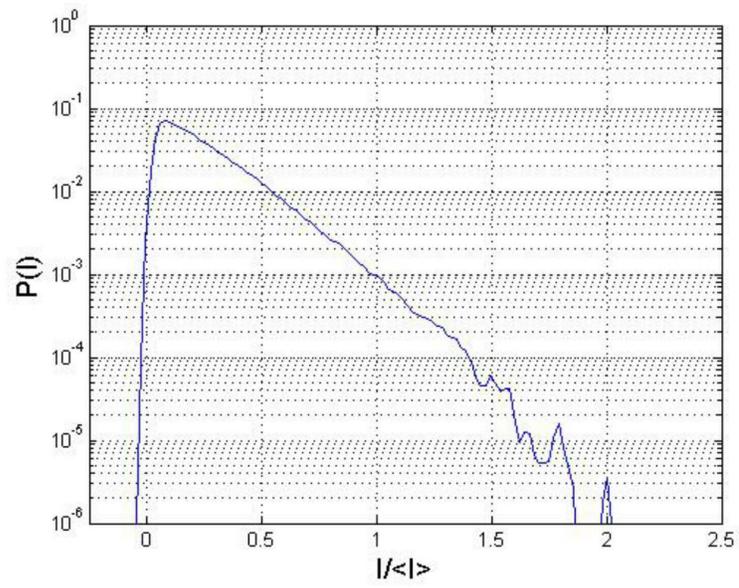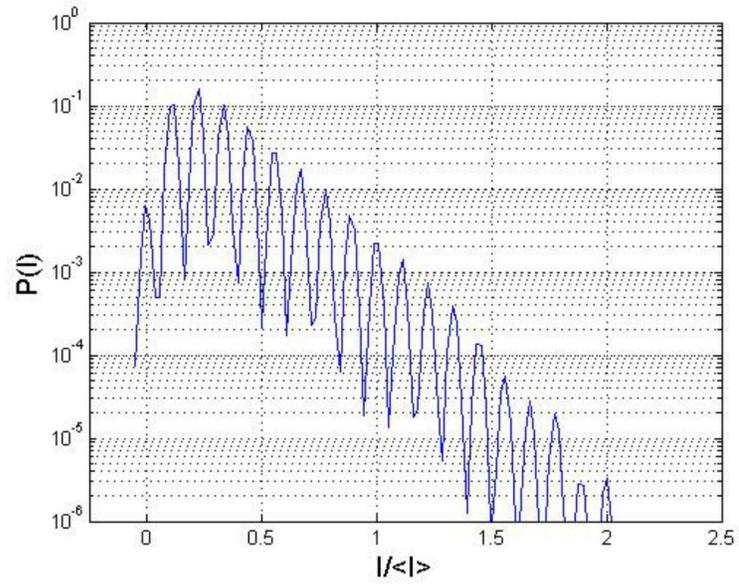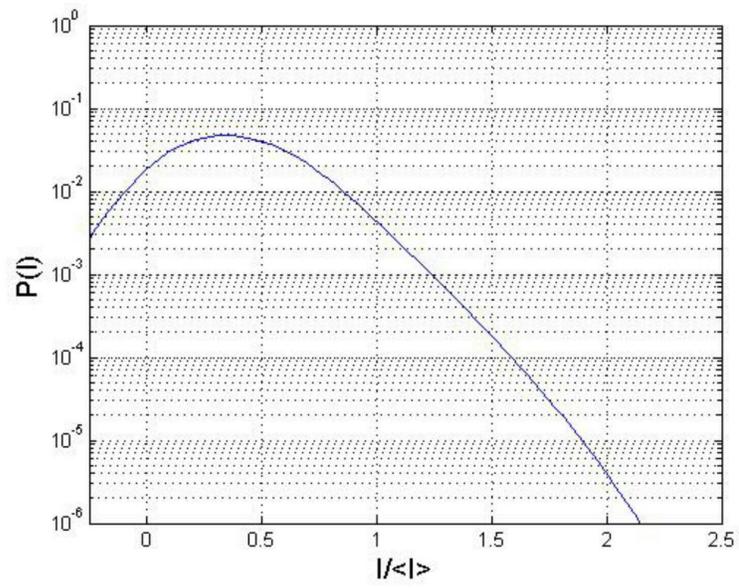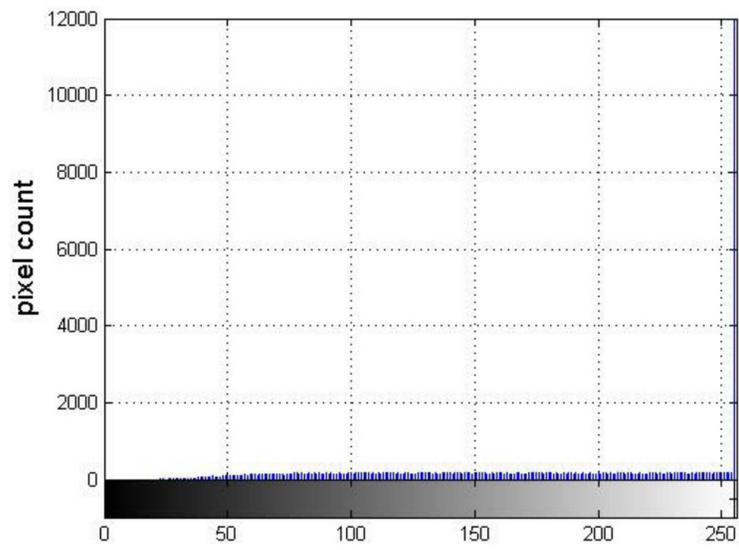
(g)
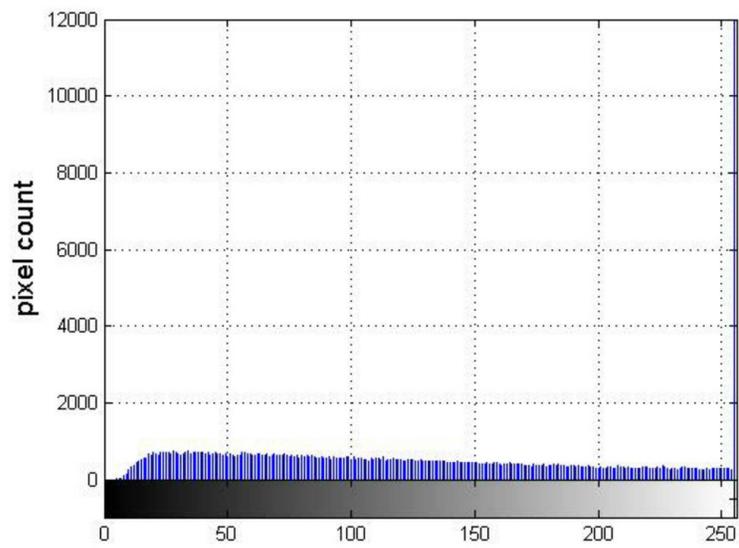
(h)
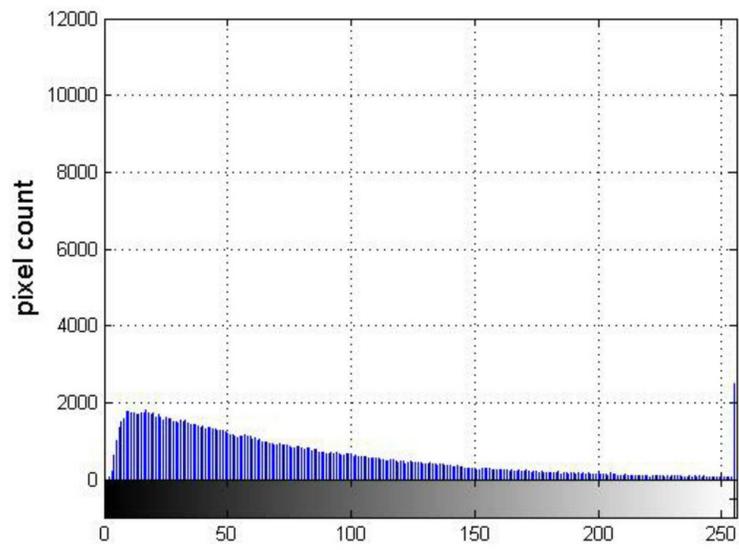
(i)
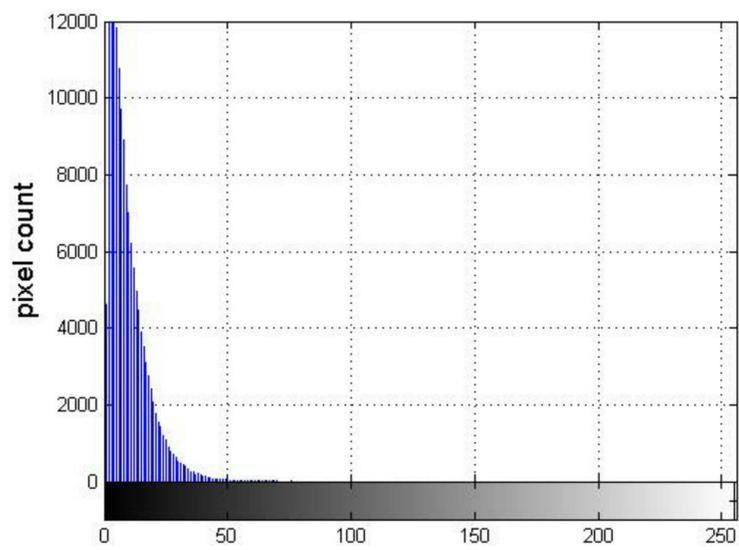
(j)
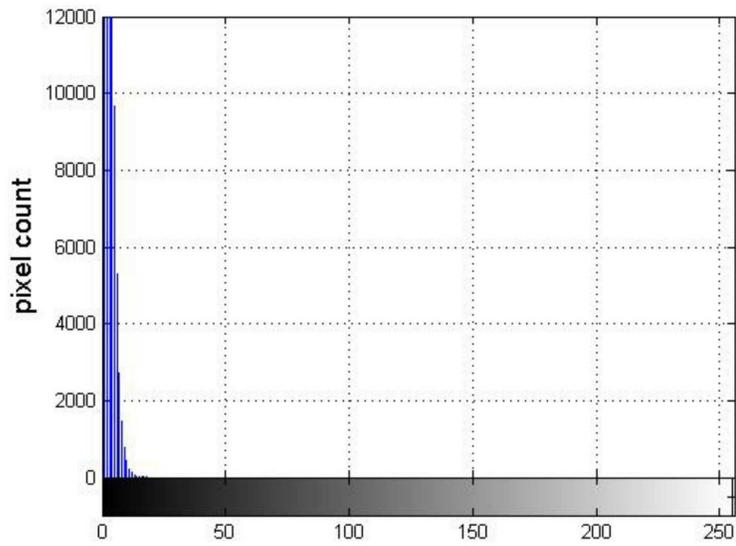
(k)
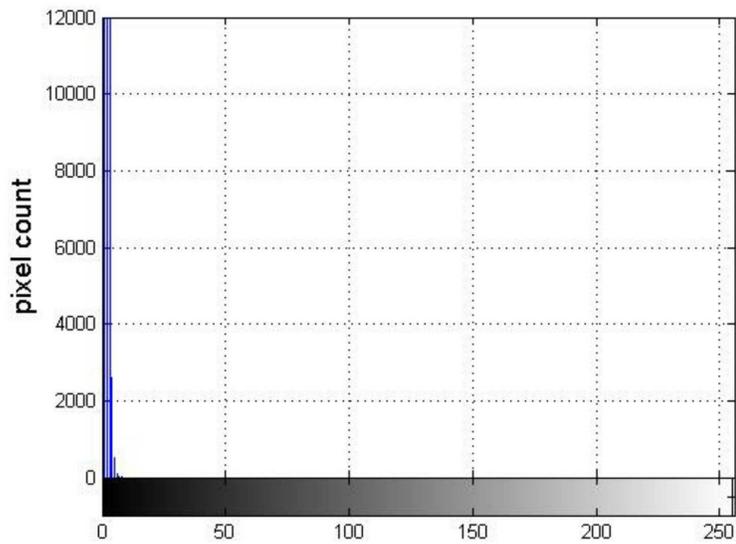
(l)

Fig 58. PDF of speckle patterns at (a) 100%, (b) 30%, (c) 8.75%, (d) 1.1%, (e) .35%, and

(f) .12% of full intensity, plotted on a log scale. Camera histogram of speckle patterns at

(g) 100%, (h) 30%, (i) 8.75%, (j) 1.1%, (k) .35%, and (l) .12% of full intensity.
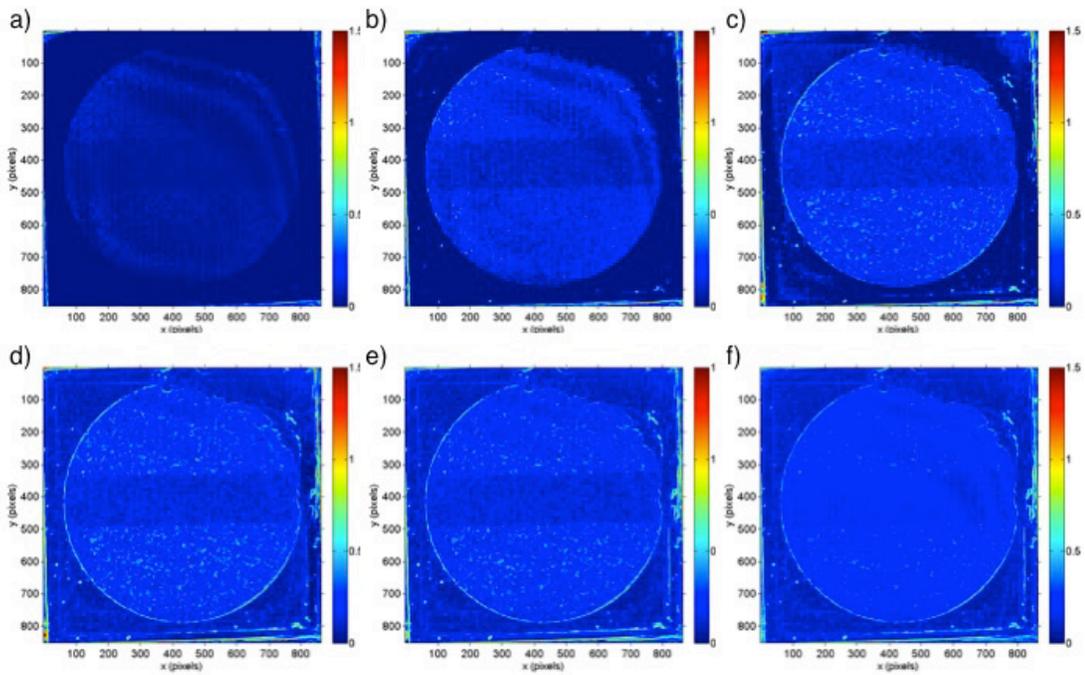
Fig 59. Spatial analysis of speckle patterns at intensities of (a) 100%, (b) 30%, (c) 8.75%, (d) 3.4%, (e) 1.1%, and (f) .35%. The ring in the upper right corner of the images come from statistically negligible noise in the optical system.
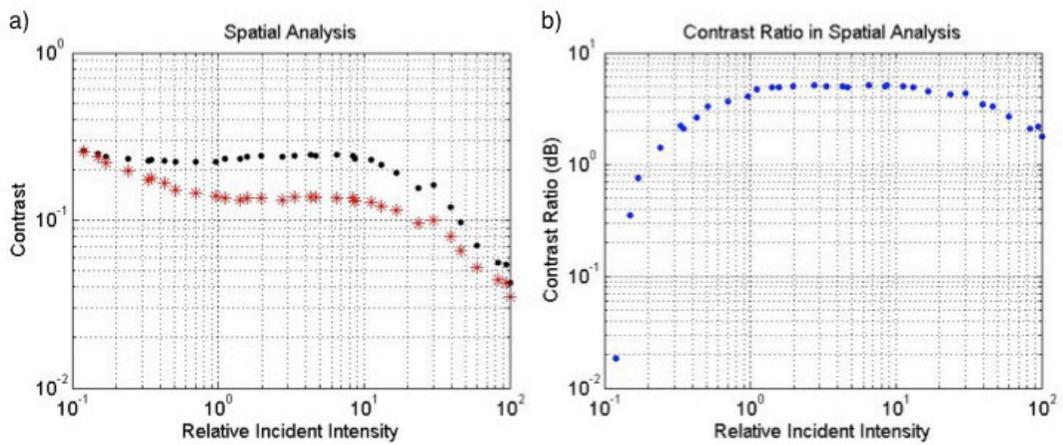
Fig 60. (a) Contrast of speckle regions in spatial averaged LSCI. Red stars indicate the 'flow' region of faster decorrelating speckle, with the black dots indicative of the 'tissue' region with slower decorrelating speckle. (b) Contrast ratio of the 'flow' region and the 'static' region. Optimum sensitivity to temporal changes follow the trends in Figure 52.
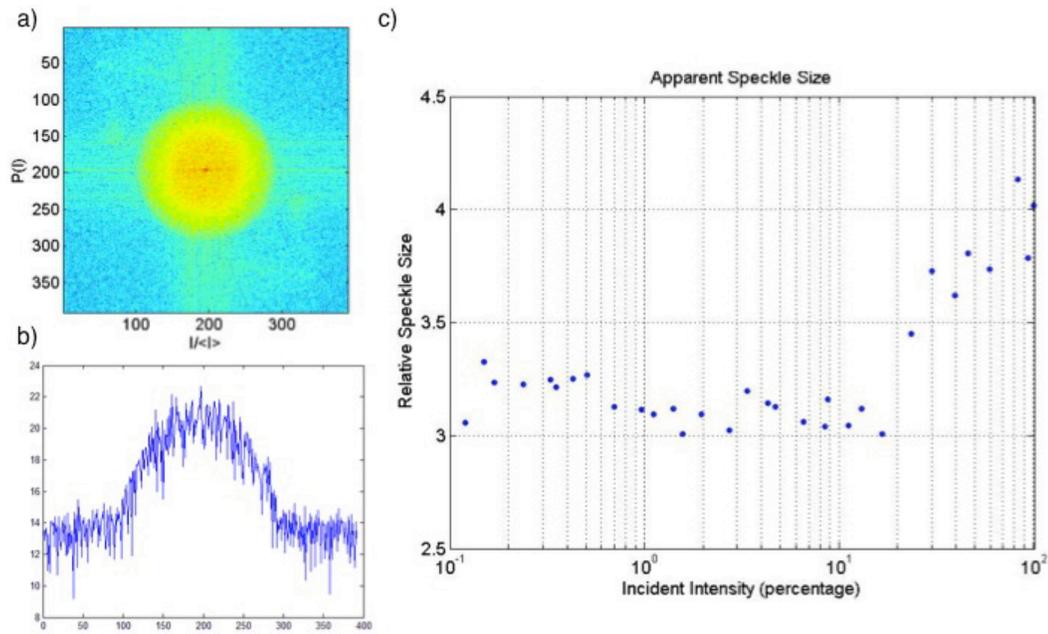
Fig 61. (a) PSD of frozen speckle pattern imaged at 8.75 % of full intensity (b) Frequency energy crossing the full image width, passing through the center. (c) Frequency information was used to calculate apparent speckle size (Eq. 4) at each incident intensity.
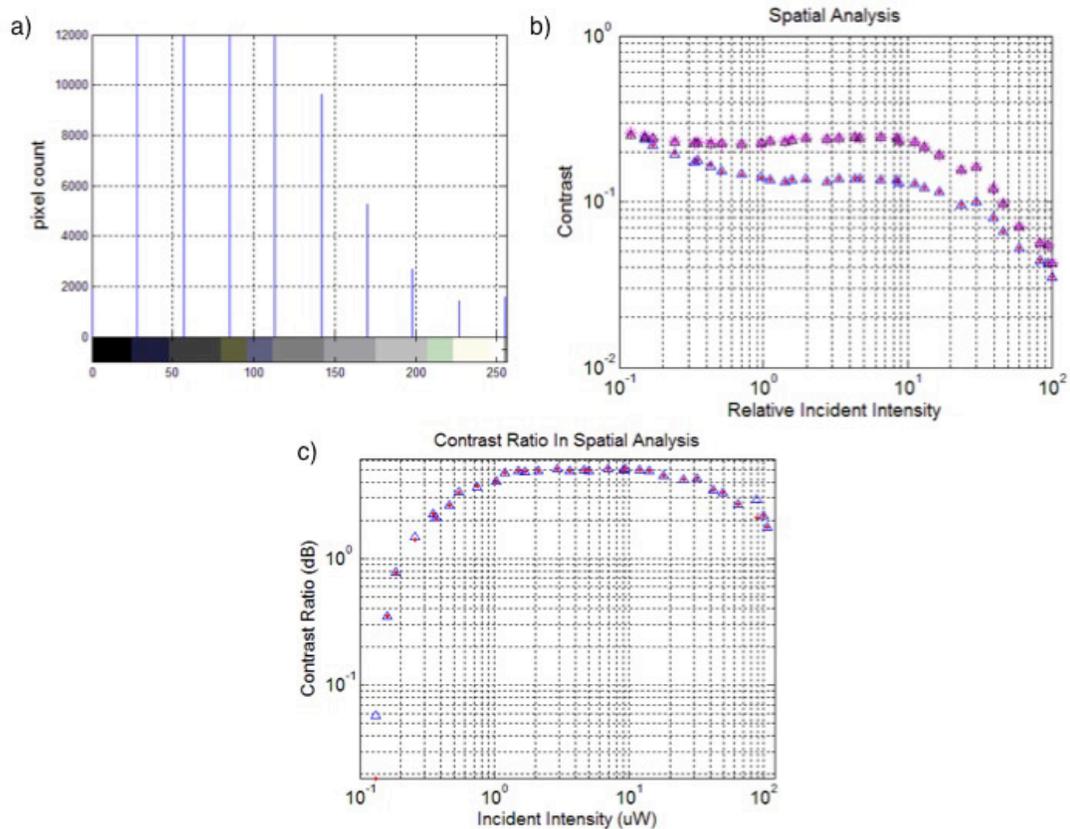
Fig 62. Raw speckle data imaged at 0.35% intensity: (a) histogram scaled (b) Contrast values shown with all images scaled to fill the full dynamic range of the 8-bit camera. The optimum imaging window of incident intensity showed little to no difference in the spatial analysis between the original (red stars) and scaled (blue triangles) images (c) Contrast ratio of the 'flow' region and the 'static' region for both scaled (blue triangle) and unscaled (red star) speckle.

Chapter 10

(Paper 7)

Temporal Ultrasound Speckle Contrast Imaging for the Visualization of Flow and Tissue Perfusion[1]

Contribution of Authors:

Sean J. Kirkpatrick: Principal Investigator, data evaluation, writing and edition

Kosar Khaksari: Developed theory, Wrote computer code, Analyzed data, Wrote manuscript

David Rosen: Ran ultrasound experiments

Jingfang Jiang: Oversaw ultrasound experiments

Kosar Khaksari, David Rosen, Jing fang Jiang and *Sean J. Kirkpatrick**
*Corresponding Author: E-mail: sjkirkpa@mtu.edu

Michigan Technological University, Department of Biomedical Engineering, 1400 Townsend Dr., Houghton, MI, 49931 USA

---

[1] The material contained in this chapter has been accepted for publication in the *Physics in Medicine and Biology*.

Abstract

The temporal contrast of ultrasound speckle images is used to visualize flow and diffusion in tissue mimicking phantoms in this Note. Contrast, defined as the inverse of the signal-to-noise ratio is used frequently in coherent optical imaging to assess motion and flow of blood in biological tissue and in blood vessels. Laser speckle contrast imaging has been shown to be sensitive to flux in the tissues of interest. However, this modality has not been exploited in ultrasonic imaging. The results presented herein indicate that temporal ultrasound speckle contrast imaging (tUSCI) may be valuable in visualizing diffusive flow in tissues. The clinical visualization of tissue perfusion using ultrasound is a persistent clinical challenge. The purpose of this Note is to demonstrate the viability of USCI to addressing this challenge.

I. Introduction

The effective measurement of tissue perfusion by ultrasound remains a clinical challenge, particularly in small vessels $\left(\text{those with a diameter of} < 2.0 \, \text{mm}\right)$ where the sensitivity of Doppler ultrasound is poor due to the small mean Doppler shifts $\langle \omega \rangle$ associate with the low velocities in these vessels [1]. Contrast enhanced ultrasonic imaging (CEUI) with microbubbles is a relatively new approach to the imaging of tissue perfusion and has been used to assess tissue perfusion in a variety of tissues including kidney [2], muscle [3], adipose tissue [4], renal tissue [1], and vascular tissue [5]. While CEUI has become the preferred method for using ultrasound to visualize and quantify tissue perfusion, there are numerous alternative medical imaging modalities that are routinely employed for tissue perfusion imaging. These modalities, however, tend to be expensive,

211

expose the patients to ionizing radiation and/or require the injection of nuclear tracers. Such modalities include position emission tomography (PET), single photon computed tomography (SPECT), multi-detector computed tomography (CT), nuclear magnetic resonance imaging (MRI) [1]. Laser Doppler flowmetry [6] presents another, less expensive alternative, however this technique has limited depth penetration and probes only a small volume (typically ~1 mm^3) defined by the intersection of 2 laser beams. Laser Doppler flowmetry can be used in a scanning mode, however, the scanned volume is still relatively restricted in size.

Laser speckle contrast imaging (LSCI) is an alternative laser-based approach for the assessment of relative blood flow and tissue perfusion [7-9]. The technique is full field and is sensitive to both changes in the concentration and velocity of scattering particles (e.g. red blood cells). In LSCI, a broad area is coherently illuminated with a laser source and the backscattered laser speckle is recorded with a camera over a finite camera integration time. The crux of the technique is that there is a quantifiable relationship between the motion of the scattering particles and the contrast of the time integrated speckle pattern. The key, then, is to develop a correlation function between the contrast observed in the image plane and the motion of the scatterers in the object plane. Like laser Doppler flometry, LSCI has limited penetration depth which is dictated by the optical properties of the tissue under observation.

The speckle phenomenon is ubiquitous in any sort of coherent imagery, including ultrasound. Regardless of the coherent source, the underlying physics behind the formation of speckle is identical. It results from the coherent summation of scattered waves from a rough surface or scattering volume [10]. Because of the ubiquitous nature of speckle, the

speckle-based techniques used to optically assess motion and flow in biological tissue should translate to ultrasound. The purpose of this paper is to demonstrate that the moderately well-developed techniques of temporal LSCI can be applied to assessing tissue perfusion using ultrasound. By analogy, we refer to this imaging modality as temporal ultrasound speckle contrast imaging (tUSCI).

The purpose of this manuscript is to demonstrate the feasibility of using temporal speckle contrast in ultrasound images to assess flow and perfusion in tissue phantoms.

II. Theory

A brief overview of the theory behind speckle is called for in order to understand tUSCI. For a more detailed discussion of ultrasound speckle statistics, readers are referred to Burkhardt [11] and Wagner et al [12]. The discussion here will focus on simple scans, and not compound scans. The above references [11,12] discuss the statistics of compound scans. A fundamental difference between laser speckle and ultrasound speckle is that the former is an intensity measurement, while the latter is an amplitude measurement. Since ultrasound is pulsed, we can assume that during the temporal detection envelope several sinusoidal pulses with randomly distributed phases between the interval $[0, 2\pi]$ are summed. By further assuming that the resolution cell in the tissue contains a large number of scatterers, it can be readily shown that the complex amplitude A probability distribution of the speckle is circularly Gaussian and follows the Rayleigh distribution [10] of Eq. (1)

$$p(A) = \frac{A}{\psi} \exp\left(-\frac{A^2}{2\psi}\right) \quad , \tag{1}$$

where ψ is the variance of scattering amplitude A. This distribution assumes that there is a very weak, or non-existent specular component of the backscatter. That is, it assumes $\frac{A}{\sqrt{\psi}} = 0$. As $\frac{A}{\sqrt{\psi}}$ increases away from zero, the distribution becomes asymptotically Gaussian, assuming a sufficiently large number of phasors are summed. While a full discussion of the implications of this distribution on tUSCI is beyond the scope of this manuscript, and indeed still requires some theoretical development, it should be noted that it sets an upper limit on the maximum contrast values that can be obtained.

The parameter $\frac{A}{\sqrt{\psi}}$ is commonly referred to as the signal to noise ratio (SNR). To be consistent with common nomenclature, we note that

$$SNR_{\max} = \frac{A}{\sigma} = 1.91 \tag{2}$$

where $\psi = \sigma^2$. The inverse of the SNR is what is known as the contrast, K:

$$SNR^{-1} = K. \tag{3}$$

This definition is completely apart from any generalizing assumption about the underlying statistics of the field. Thus, in USCI, assuming no specular component in the echo, $K_{\max} = \frac{1}{1.91} = 0.523$. In LSCI, as we are doing herein, the typical assumption is that the speckle pattern is associated with a sufficiently large sum of complex field components that the central limit theorem can be invoked [13]. If the field components are polarized, and the phases are uniformly distributed and statistically independent, then the resulting speckle pattern displays a negative exponential PDF and the contrast as defined by Eq. (3) is exactly unity. Because ultrasound senses the envelope or magnitude of the echo, the

theoretical maximum is something less than unity [12]. These theoretical maximum values, however, have their own accompanying distributions and it is very likely that K values greater (and less) than the theoretical maximums will be observed [14].

In its most common incarnation, spatial LSCI is performed by calculating the spatial contrast by sliding a convolution window, typically on the order of 7×7 pixels in dimension, across a time integrated exposure and replacing the central pixel with the calculated contrast value for that small subset of pixels. In this approach, then, any motion of the speckle pattern during the finite exposure time leads to a reduction in contrast [7-9]. This phenomenon has been exploited by many authors to examine blood flows, for example. Recently, Khaksari and Kirkpatrick [15] demonstrated that LSCI is sensitive to total flux. Specifically, in ordered flow, LSCI is sensitive to advective flux and shows similar sensitivity to red blood cell concentration and velocity (or speed if direction is not explicitly known).

Alternatively, the temporal contrast of a sequence of speckle images can be quantified on a pixel by pixel basis [16]. The key to temporal speckle contrast imaging is to image sufficiently fast that any speckle motion is essentially stopped during a single image acquisition and then the statistics of the 'frozen' speckle can be assessed. Assuming that this condition of frozen speckle is met, then any motion over time will result in an increase in contrast, whereas zero motion will result in $K \to 0$ for a sequence of images devoid of uncorrelated noise. The high image acquisition rate of ultrasound indicates this approach for speckle contrast imaging using a sequence of B-scans.

Besides motion, consideration of the approach reveals that the final contrast values will be sensitive to other experimental parameters as well such as size (relative to detector

pixel size) and the shape of the individual speckles and the number of B-scans analyzed. As noted by Burckhardt [11], the speckle size is on the order of the resolution of the scanner and depends therefore on the aperture of the transducer. Wagner et al. [12] note that the dimensions of the speckle are different in the axial and longitudinal directions. They note that in the axial direction, the speckle width is inversely related to the pulse bandwidth and that in the longitudinal direction, the speckle dimension is proportional to the transducer beam width and thus increases with increasing range.

III. Experiments

Experiments were performed on flow phantoms to demonstrate the basic concept of tUSCI. A programmable ultrasound system (Verasonics Inc. Redmond, WA) equipped with a linear array ultrasound probe (L7-4 Phillips Inc., center frequency 5MHz, 60% fractional bandwidth) was used to acquire ultrasound data. Raw IQ ultrasound data under the plane wave mode were exported from the ultrasound system for off-line post-processing. B-scans were acquired at a rate of 200 Hz.

The ultrasound flow phantom was composed of a soft, latex rubber tube (8mm inner diameter, 1mm wall thickness) imbedded in a block of tissue-mimicking (TM) gelatin (7.4% dry weight gelatin, sigma-Aldrich Inc., St Louis, MO, USA). The TM gelatin block was constructed and housed in a 50mL plastic container. Glass microspheres (50-100 micrometer diameter, sigma-Aldrich Inc., St Louis, MO, USA) were added to the TM gelatin as scattering source for ultrasound imaging. Degassed water containing Nylon microbeads (7-11 micrometer diameters, 4% by weight, Arkema, Inc., Colombes, France) was flowed through the ultrasound flow phantom.

216

Three different flow conditions were investigated. In the first condition, the fluid flow through the 8 mm tube without any blockage. In conditions 2 and 3, a 10 mm long piece of sponge was placed into the tube in order to create diffusive flow. Under conditions 2 and 3, diffusive flow was induced by two different pressure gradients, respectively, and their flow rates (0.44 ml/s and 0.79 ml/s) were measured by a graduate cylinder.

IV. Results

Speckle Size and Probability Distribution

Ensuring that the speckle pattern is adequately sampled in a spatial sense is a requirement for USCI, as it is for LSCI [7-9]. If the speckles are not spatially sampled to at least meet the (spatial) Nyquist criteria (greater than 2 pixels per speckle) [17], the temporal statistics (e.g., the temporal derivatives) cannot represent the true value of the speckles and the speckles will be temporally uncorrelated. Spatially undersampling leads to a reduction in the accuracy of the tUSCI estimates. The minimum speckle size (in pixels) φ_{min} was determined by calculating the power spectral density (PSD) of the raw speckle images in the B-scan sequences and applying Eq. (4) which the yields minimum speckle size in terms of pixels:

$$\varphi_{min} = 2\left(\frac{\text{Width of Array}}{\text{Diameter of PSD Energy Band}}\right). \tag{4}$$

Figure (63a) displays a typical B-scan from the flow sequence. The B-scan was not compounded in any form so as to not reduce the speckle visibility. Figure (63b) displays the experimental histogram of the B-mode data from Fig. (63a). The data clearly display a Rician distribution. Figure (63c) is the PSD of Fig. (63a). By employing Eq. (4), then,

from Fig. (63c), the minimum speckle size for this B-scan was ~8.1 pixels in the axial direction and ~6.2 pixels in the range direction.

Contrast Images

In this section, we display 3 sets of contrast images, one set for each flow condition. In each set contrast images generated over 10, 100 and 200 images are displayed displaying the effects of number of frames analyzed on the final contrast image. Raw speckle images are also displayed. Note that for display purposes, the scales of the contrast images, even within a single set, vary.

In these contrast images, higher values are indicative of speckle motion due to moving scatterers in the flow phantoms. Motion is from left to right. Figure (64) displays the images generated from the unrestricted flow model. The flow in the 8 mm tube is clearly visible due to the change in temporal contrast. The contrast ratio K_{ratio} between the region with the flowing fluid and the static gel increased with an increase in the number of images analyzed. This is consistent with what has been reported prior for temporal laser speckle contrast imaging [16]. K_{ratio} was determined by taking the ratio between the mean contrast in the flow region and the mean contrast in the static gel region. Figure (67) displays the influence of the number of frames analyzed on K_{ratio} .

Figures (65) and (66) show the results for the diffusion experiments. Again, the diffusional motion is clearly visible by the increase in contrast. Of particular note, is that as the number of frames analyzed was increased, the fraction of the image in the flow region displaying an increased contrast increased form left to right in the image. This

increase in high contrast area shows the moving diffusion front through the sponge phantom.

Similar to above, as the number of frames analyzed increased, K_{ratio} decreased. Figure (67) displays these results. A more detailed study is necessary for proper interpretation of this plot, however, it does reveal that there is a clear distinction between the 3 different flow conditions.

V. Conclusions

The results of this study demonstrate the feasibility of tUSCI for visualizing flow and perfusion in tissue flow phantoms. By increasing the number of frames analyzed (which corresponds to increasing the time of observation), the moving diffusion front was visualized. For example, by analyzing over 150 frames, the total time in which the data were analyzed was 0.75s, while when analyzing 200 frames, the total time over which the data were analyzed was 1.0 s. Thus, the diffusive flow images (Figs. 3 and 4) show the motion of the diffusion front from 0.05 s (10 frames) to 1 s (200 frames). This indicates that USCI may be a useful modality in visualizing diffusive flow in tissues using ultrasound. Further work is indicated, both theoretical and experimental. The visualization of diffusional flux in deep tissue remains a clinical challenge. However, the results of this investigation indicate that tUSCI holds promise as a simple means of assessing diffusional flux [15] in tissues using the temporal statistics of ultrasound speckle without the addition of contrast agents, nuclear tracers or exposing the patient to ionizing radiation.

VI. References

219

1. Quaia, E 2011, 'Assessment of tissue perfusion by contrast enhanced ultrasound', *Eur. Radiol.*, vol. 21, pp. 604-615.

2. Wei K, Le E, Bin JP, Coggins M, Thorpe J, Kaul S 2001, 'Quantification of renal blood flow with contrast-enhanced ultrasound', *J. Am. Coll. Cardiol.* vol. 37, pp. 1135–1140.

3. Weber MA, Krix M, Jappe U et al 2005, 'Pathologic skeletal muscle perfusion in patients with myositis: detection with quantitative contrast-enhanced US—Initial results', *Radiology*

vol. 238, pp. 640–649.

4. Flynn A, Li Q, Panagia M, et al. 2015, 'Contrast enhanced ultrasound: A novel noninvasive, nonionizing method for the detection of brown adipose tissue in humans', *J. Am. Soc. Echocardiogr.* vol. 28, no., 10, pp 1247-1254.

5. Masugata H, Peters B, Lafitte S, et al, 2001, 'Quantitative assessment of myocardial perfusion

during graded coronary stenosis by real-time myocardial contrast refilling curves', *J. Am. Coll. Cardiol.* vol. 37, pp. 262–269.

6. Bonner R, Nossal, R, 1981, 'Model for laser Doppler measurements of blood flow in tissue', *Appl. Opt.* vol. 20, no. 12, pp 2097-2107.

7. Fercher AF and Briers JD, 1981 'Flow visualization by means of single-exposure speckle photography," *Opt. Commun*. vol. 37 no. 5, pp 326-330.

8. Boas DA and Dunn AK 2010 'Laser speckle contrast imaging in biomedicine,' *J. Biomed. Opt.* vol. 15, no. 1, 011109.

9. Briers JD et al. 2013 'Laser speckle contrast imaging: Theoretical and practical limitations,' *J. Biomed. Opt.* vol. 18, no. 6, 066018.

10. Goodman J., 2007, *Speckle phenomena in optics*, Roberts & Co., Englewood, CO, USA.

11. Burckhardt CB, 1978, 'Speckle in ultrasound B-mode scans,' *IEEE Trans. Sonics & Ultrasonics*, vol. su-25, no. 1, pp 1-6.

12. Wagner RF, Smith SW, Sandrik JM, and Lopez, H, 1983, 'Statistics of speckle in ultrasound B-scans,' *IEEE Trans. Sonics & Ultrasonics*, vol. 30, no. 3, pp 156-163.

13. Duncan DD and Kirkpatrick SJ 2008, 'Can laser speckle flowmetry be made a quantitative tool?,' *J. Opt. Soc. Am* vol. 25, no.8, pp. 2088-2094.

14. Duncan DD, Kirkpatrick SJ, and Wang RK 2008, 'Statistics of local speckle contrast,' *J. Opt. Soc. Am A* vol. 25, pp. 9-15.

15. Khaksari K and Kirkpatrick SJ, 2016 'Laser speckle contrast imaging is sensitive to advective flux,' *J. Biomed. Opt.* (in press).

16. Kirkpatrick SJ, Wang, R, and Hinds MT, 'Quantitative temporal speckle contrast imaging for tissue mechanics,' *J Opt. Soc. A* vol. 24, no. 12, pp. 3728-2734.

17. Kirkpatrick SJ, Duncan DD, and Wells-Gray, EM 2008, 'Detrimental effects of speckle-pixel size matching in laser speckle contrast imaging,' *Optics letters* vol. 33, no. 24, pp. 2886-2888.

Figure 63a. B-scan of the unrestricted flow phantom. The tube containing the flow is

the slightly darker region approximately 2/3 of the way down from the top. No

information about motion is revealed.

Figure 63b. Probability distribution function of the B-scan shown in Fig. (63a). The distribution is Rician, starting to converge on a Gaussian distribution indicating a significant specular component to the echo.


Figure 63c. Power spectral density of the B-scan shown in Fig. (63a) used to compute the minimum speckle size in both the axial and the range direction. The non-circular

shape of the bright central energy band indicates that the speckles have different

dimensions in the two directions.


(a)

(b)

(c)

(d)

Figure 64. (a) B-scan of the unrestricted flow phantom. (b) Temporal contrast image using 10 frames to calculate the contrast statistic. (c) Temporal contrast image using 100 frames to calculate the contrast statistic. (d) Temporal contrast image using 200 frames to calculate the contrast statistic.

(a)

(b)

227

(c)

(d)

228

Figure 65. (a) B-scan of the diffusive flow phantom with a slower flow rate. (b) Temporal contrast image using 10 frames to calculate the contrast statistic. (c) Temporal contrast image using 100 frames to calculate the contrast statistic. (d) Temporal contrast image using 200 frames to calculate the contrast statistic. Of particular note is the progression of the area of the image that displays increasing from left to right contrast as time (number of frames) increases. This indicates a diffusion front moving through the sponge.

(a)

(b)

(c)

230

(d)

Figure 66. (a) B-scan of the diffusive flow phantom with a faster flow rate. (b) Temporal contrast image using 10 frames to calculate the contrast statistic. (c) Temporal contrast image using 100 frames to calculate the contrast statistic. (d) Temporal contrast image using 200 frames to calculate the contrast statistic. Of particular note is the progression of the area of the image that displays increasing from left to right contrast as time (number of frames) increases. This indicates a diffusion front moving through the sponge.

Figure 67. Plot of the ratio of the temporal contrast in the flow region to that in the static

gel region, K_{ratio}. From top to bottom, K_{ratio} for the slow diffusive phantom (green stars

on-line), K_{ratio} for the unrestricted flow phantom (red dashes on-line), and K_{ratio} for the

fast diffusive phantom (blue dots on-line).

Appendix A:

Copyright agreement of SPIE journals (chapters 6,7, 8 and 9):

SPIE   **TRANSFER OF COPYRIGHT TO SOCIETY OF PHOTO-OPTICAL INSTRUMENTATION ENGINEERS (SPIE)**

Title of Paper: _____

SPIE Paper Number: (xxxx-xx) _____   **Contact Author Email:** _____

Author(s): _____

This signed statement must be returned to SPIE prior to the scheduled publication of the Proceedings or Journal in which the Paper will be published. The intent of this Agreement is to protect the interests of both SPIE and authors/employers and to specify reasonable rights for both parties related to publication and reuse of the material.

The undersigned hereby assign(s) to Society of Photo-Optical Instrumentation Engineers (SPIE) copyright ownership in the above Paper, effective if and when the Paper is accepted for publication by SPIE and to the extent transferable under applicable national law. This assignment gives SPIE the right to register copyright to the Paper in its name as claimant and to publish the Paper in any print or electronic medium.

Authors, or their employers in the case of works made for hire, retain the following rights:

1. All proprietary rights other than copyright, including patent rights.
2. The right to make and distribute copies of the Paper for internal purposes.
3. The right to use the material for lecture or classroom purposes.
4. The right to prepare derivative publications based on the Paper, including books or book chapters, journal papers, and magazine articles, provided that publication of a derivative work occurs subsequent to the official date of publication by SPIE.
5. The right to post an author-prepared version or an official version (preferred version) of the published paper on an internal or external server controlled exclusively by the author/employer, provided that (a) such posting is noncommercial in nature and the paper is made available to users without charge; (b) a copyright notice and full citation appear with the paper, and (c) a link to SPIE's official online version of the abstract is provided using the DOI (Document Object Identifier) link.

   Citation format:
   Author(s), "Paper Title," Publication Title, Editors, Volume (Issue) Number, Article (or Page) Number, (Year).

   Copyright notice format:
   Copyright XXXX (year) Society of Photo-Optical Instrumentation Engineers. One print or electronic copy may be made for personal use only. Systematic reproduction and distribution, duplication of any material in this paper for a fee or for commercial purposes, or modification of the content of the paper are prohibited.

   DOI abstract link format:
   http://dx.doi.org/DOI# (*Note: The DOI can be found on the title page or online abstract page of any SPIE article.*)

If the work that forms the basis of this Paper was done under a contract with a governmental agency or other entity that retains certain rights, this Transfer of Copyright is subject to any rights that such governmental agency or other entity may have acquired.

By signing this Agreement, the authors warrant that (1) the Paper is original and has not previously been published elsewhere; (2) this work does not infringe on any copyright or other rights in any other work; (3) all necessary reproduction permissions, licenses, and clearances have been obtained; and (4) the authors own the copyright in the Paper, are authorized to transfer it, and have full power to enter into this Agreement with SPIE.

WHO SHOULD SIGN. This form must be signed by (1) at least one author who is not a U.S. Government employee and (2) the author's employer if the Paper was prepared within the scope of the author's employment or was commissioned by the employer. If not signed by all authors, the author(s) signing this Agreement represents that he/she is signing this Agreement as authorized agent for and on behalf of all the authors.

_____   _____   _____
Author's signature   Print name   Date (mm/dd/yyyy)

_____   _____   _____
Author's signature   Print name   Date (mm/dd/yyyy)

_____   _____   _____   _____
Authorized Employer signature   Print name   Title   Date (mm/dd/yyyy)

U.S. GOVERNMENT EMPLOYMENT CERTIFICATION
A work prepared by a U.S. Government employee as part of his or her official duties is not eligible for U.S. Copyright. If all authors were U.S. Government employees when this Paper was prepared, and the authors prepared this Paper as part of their official duties, at least one author should sign below. If at least one author was not a U.S. Government employee, the work is eligible for copyright and that author should sign the Transfer of Copyright form above.

_____   _____   _____
Author's signature   Print name   Date (mm/dd/yyyy)

Submit this form online at http://spie.org/myaccount
Director of Publications, SPIE, P.O. Box 10, Bellingham, WA 98227-0010 USA • Phone: 360/676-3290 (Pacific Time) • Fax: 360/647-1445 • Revised 14 May 2013